The Geomagnetic Latitude Effect on Atmospheric Muons at Ground Level Altitude

谷崎, 圭祐

(Degree)
博士（理学）
(Date of Degree)
2004-03-31
(Date of Publication)
2012-02-06
(Resource Type)
doctoral thesis
(Report Number)
甲3155
(URL)
https://hdl.handle.net/20.500.14094/D1003155

博士論文

The Geomagnetic Latitude Effect on Atmospheric Muons at Ground Level Altitude

（地上における大気μ粒子の地磁気緯度効果の研究）

平成16年2月

神戸大学大学院自然科学研究科

谷崎　圭祐

The Geomagnetic Latitude Effect on Atmospheric Muons at Ground Level Altitude

Keisuke Tanizaki

KOBE University

Graduate School of Science and Technology

27/Feb/2004

Abstract

The BESS-2001 (Balloon-borne Experiment with Superconductiong Spectrometer) ground experiment was performed at Ft. Sumner in 2001. We obtained precise atmospheric muon spectra at atmospheric depth of 892 g/cm^2 with the geomagnetic cut-off rigidity of 4.2 GV. In order to estimate the dependence of the intensity of muons on the geomagnetic latitude, the result of BESS-2001 was compared those obtained on our previous BESS experiments performed at two different observation sites with different years. Since the measurements were made at different altitudes and different period, we can discuss the effect of the solar modulation and altitude dependence of the muons using those observed data. We determined the momentum dependence of the charge ratio of muons very precisely, and its dependence on the altitude and magnetic cut-off rigidity of the observation site.

Contents

List of Figures

List of Tables

Chapter 1

Introduction

Dominant components of primary cosmic rays from space are protons and helium nuclei with their fractions of about 90 % and 10 %, respectively. The primary cosmic rays enter the atmosphere surrounding the earth and interact with the atmospheric nuclei. Thus, hadronic interactions create atmospheric secondary particles such as pions, kaons, antiprotons, gamma rays and other particles. Since the secondary particles also interact with the atmospheric nuclei, the number of secondary particles increases along the propagation of cosmic ray, until the energy of each particle becomes too small to produce any particles. Finaly, the atmospheric cosmic rays on ground are almost muons and electrons.

Atmospheric muons as the decay product of the secondary pions and kaons arrive on the ground with information of the spectrum of primary particles and the effect of propagation through the atmosphere. Solar modulation of primary particles is infered by the measurement of atmospheric muon on the ground. Geomagnetic cut-off is also reflected in the muon spectrum. The trajectry of the charged particles entering the earth is defelected by the geomagnetic field of the earth. The lowest momentum to enter the earth is called a cut-off rigidity. Since the absolute flux of primary particles varies at different geomagnetic latitudes by the geomagnetic cut-off effect, the absolute flux of atmospheric muons on the ground also varies.

The intensity of muons changes not only by the effect of magnetic cut-off rigidity, but is also affected by the atmospheric temperature and pressure of the observing places. In order to estimate precisely the geomagnetic cut-off effect, it is needed to estimate and extract other effects.

Observations of the geomagnetic cut-off effect were mainly performed from 1930's to 1970's by transporting instruments from one place to the other by making a voyage via ships, air planes and other ways. However, most of the previous experiments did not present an absolute flux. They normalized their observed spectrum to a standard value such as Rossi point [4] probably because it was difficult to estimate the exposure factor and the total efficiency precisely. The geomagnetic factor of the BESS(Balloon-borne Experiment with Superconductiong Spectrometer) detector can be calculated precisely, and we can estimated the exposure factor and the total efficiency of the measurement accurately.

For further precise investigation of the atmospheric neutrino oscillation, it is crucial to make an accurate prediction of the energy spectrum of neutrinos. One of the uncertainties in this prediction is the effect of geomagnetic cut-off. Since the muon production and their decay process are directly linked with the neutrino production, precise measurements of the atmospheric muon flux on ground at different magnetic latitudes are important.

The atmospheric muon flux changes with atmospheric depth; It increases with depth at high altitude, and then decreases towards deeper atmosphere. The decay probability and the energy loss in the atmosphere depend on the muon energy. Thus precise and systematic measurements and analysis of individual cosmic-ray flux and their spectral shapes are fundamental and crucial to improve the accuracy of the atmospheric neutrino flux calculations.

As shown in Figure 1.1 and Figure 1.2, measurements of atomospheric muons at different geomagnetic cut-off locations have been carried out on the ground [1] [2] [3]. In addition to the observations at balloon altitudes, BESS has performed observations on the ground level and mountain altitude since 1995. The BESS-1995 experiment was performed on the ground at Tsukuba, Japan in 1995 [1]. The BESS-1997-1999 experiments was performed on the ground at LynnLake, Northen Canada from 1997 to 1999, during the period of preparation for balloon flight experiments [1]. The BESS-1999 experiment was carried out at Mt. Norikura, Japan, near SuperKamiokande, in 1999 [2].

Recently the results of experiments by the other group have been presented, and these are shown together with our data in Figure 1.1, 1.2. The CAPRICE94 and the CAPRICE97 were performed on the ground at LynnLake in 1994 and at Ft. Sumner in 1997, respectively.

These spectra include effects of the geomagnetic cut-off, altitude, solar modulation, and atmosphere. The absolute muon flux is affected by the altitude of observation sites even if they locate at the same geomagnetic cut-off rigidity. The muon flux changes with altitude by the processes of muon decay and production, and is affected by the atmospheric conditions of the observation sites. The flux is also affected by the primary cosmic-ray intensity which is modulated by solar activity. In order to derive a geomagnetic cut-off effect, absolute muon spectra should be corrected for the effects of altitude variation and solar modulation.

The BESS-2001 ground experiment was carried out at Ft. Sumner, New Mexcio, U.S.A. on 9th, September 2001 during a preparation period for the flight. The geomagnetic cut-off rigidity at Ft. Sumner is 4.2 GV. In advance to this observation on the ground were performed at Tsukuba and LynnLake with geomagnetic cut-off rigidity of 11.4 GV and 0.4 GV, respectively. Using the atmospheric muon flux at three different geomagnetic cut-off locations, the effect of the geomagnetic cut-off on the absolute muon spectra can be evaluated.

In this thesis, we report a series of precise measurements of atmospheric muons on the ground, and compare them with those observed by other group and with a theoretical calculation using the geomagnetic cut-off models currently used in the neutrino flux estimation. Chapter 2 gives a description of the BESS spectrometer. Chapter 3 describes details of the ground experiments. In Chapter 4, we analyze the data obtained in this ground experiment to select muon cadidates, and the estimation of various corrections and backgrounds. Then, Chapter 5 determines the muon flux, and estimates various uncertainties in the derivation of the absolute flux from the observed data. In Chapter 6, solar activity dependence and altitude dependence of the muon flux and charge ratio are estimated, and geomagnetic latitude effect to those quantities is discussed quantitatively. In the last Chapter 7, summarize the result.

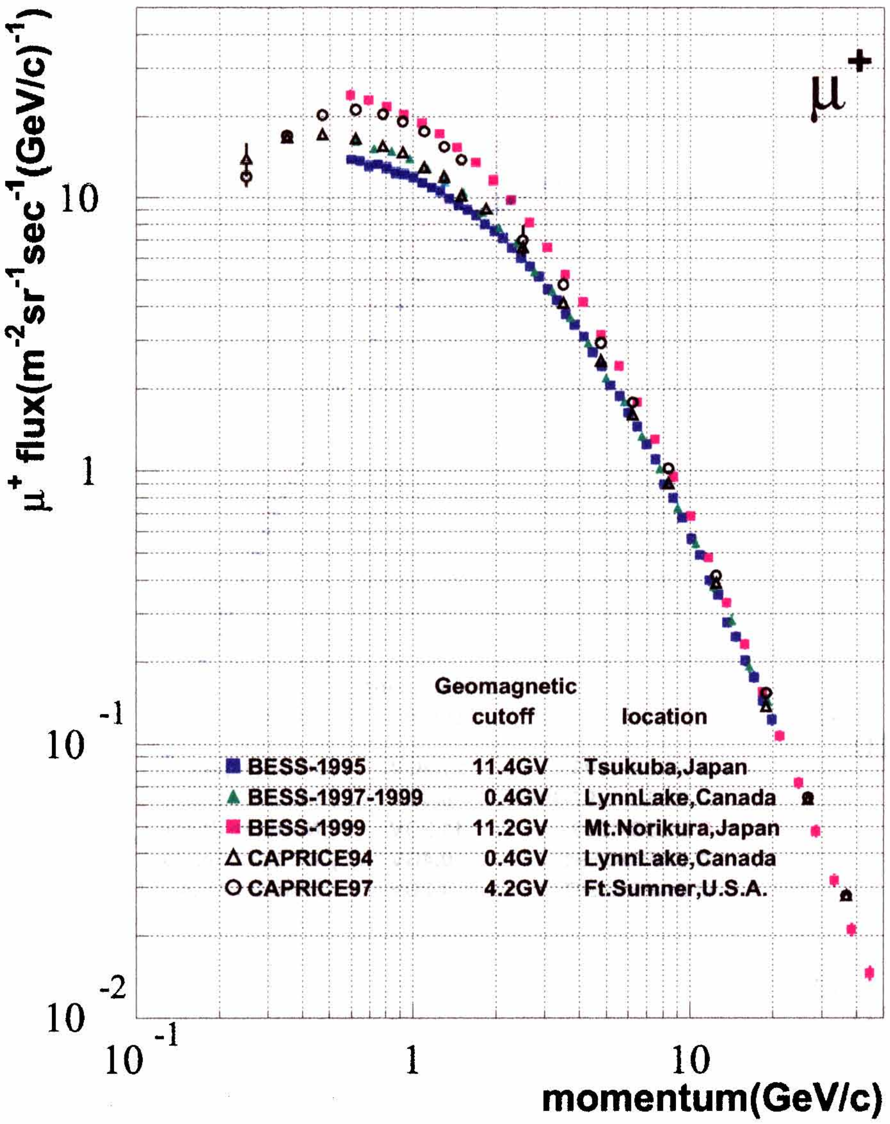

Figure 1.1: Observed μ^+ spectra on ground at different geomagnetic cut-off locatitons.

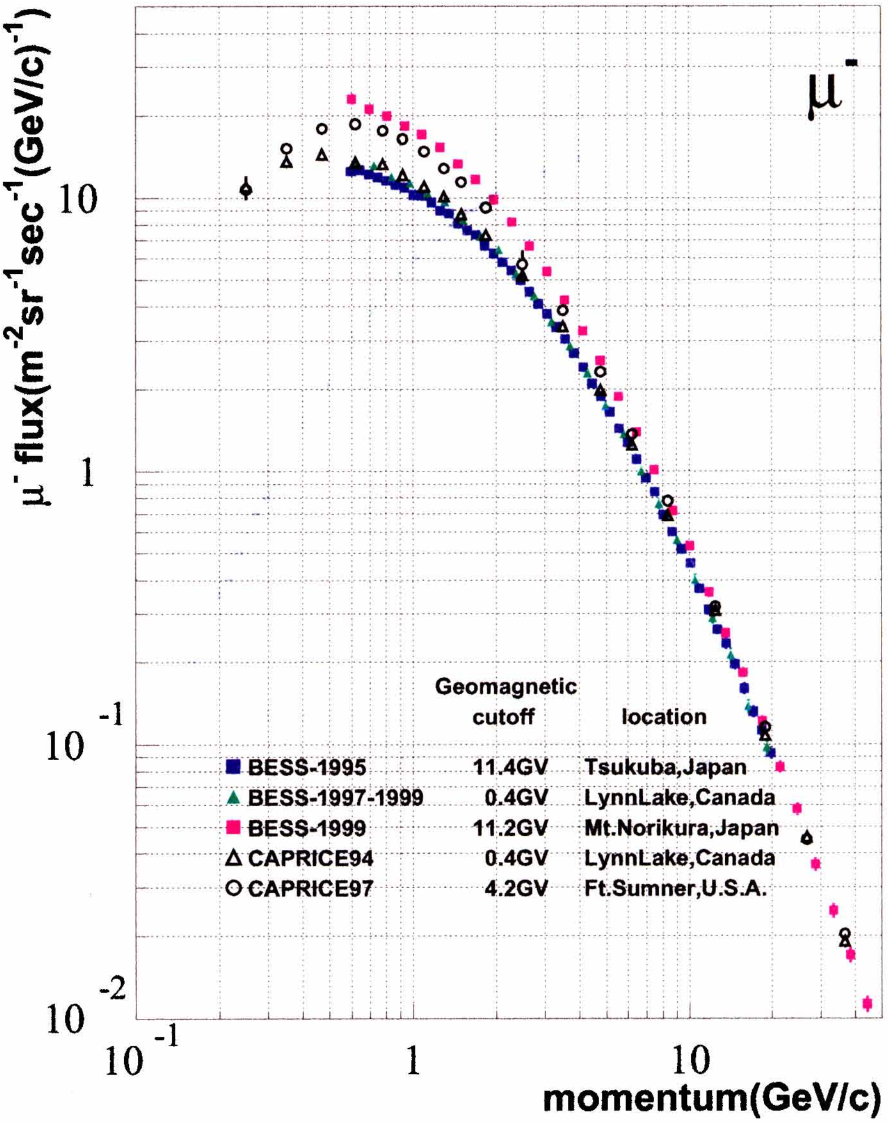

Figure 1.2: Observed μ^- spectra on ground at different geomagnetic cut-off locatitons.

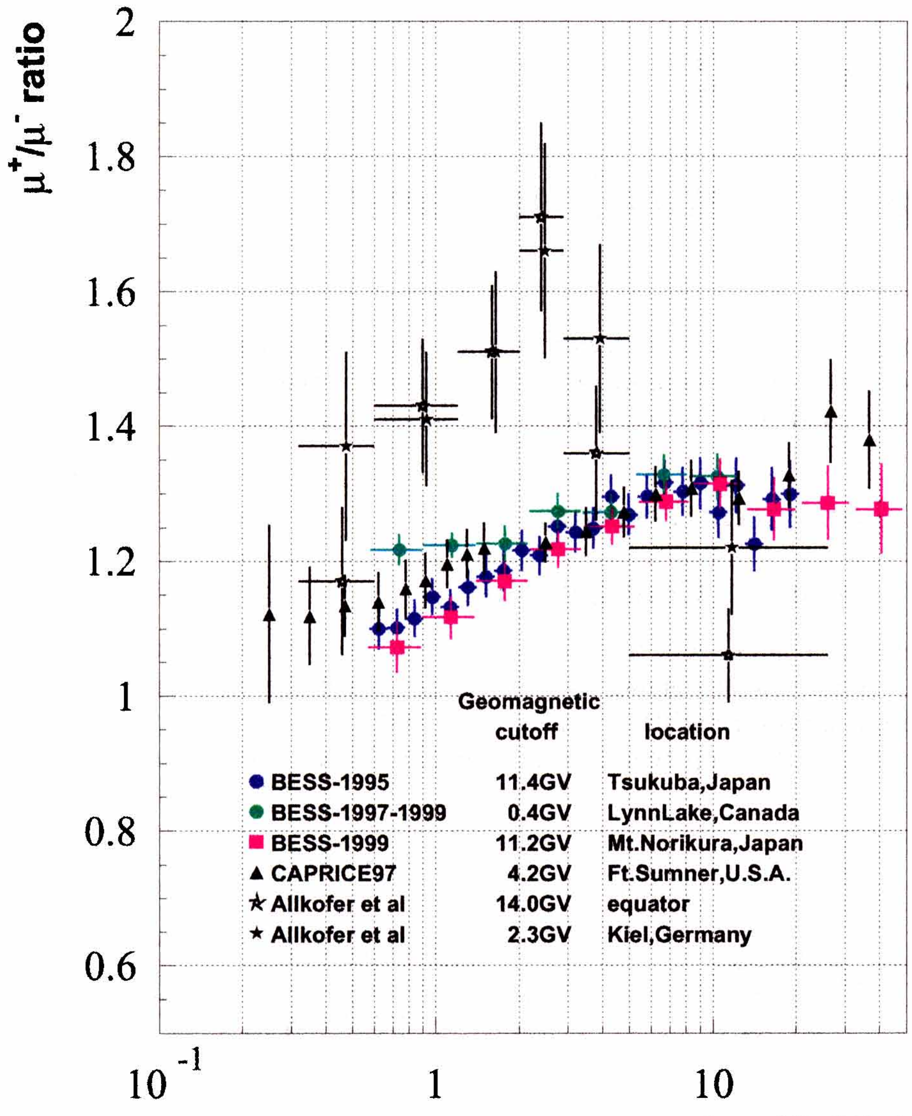

Figure 1.3: Observed μ^+/μ^- charge ratios on ground at different geomagnetic cut-off locatitons.

Chapter 2

Experimental apparatus

This chapter provides an overview of the employed apparatus [5, 6, 7, 8]. Basic features, design concept and performance of the individual detector components and the data acquisition system are described.

2.1 Detector Layout

2.1.1 Detector Configuration

The detector components were arranged concentrically as shown in Figure 2.1. A particle traversing the apparatus passed through, from outside to inside, a plastic scintillator hodoscope (TOF), two layers of outer drift chambers (ODC) a superconducting solenoid (MAG), two layers of inner

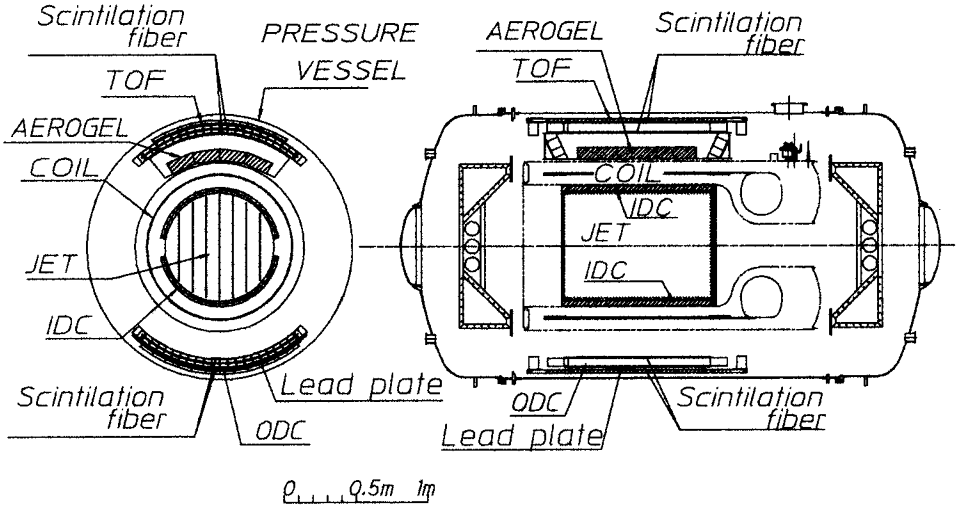

Figure 2.1: Cross section of the BESS detector.

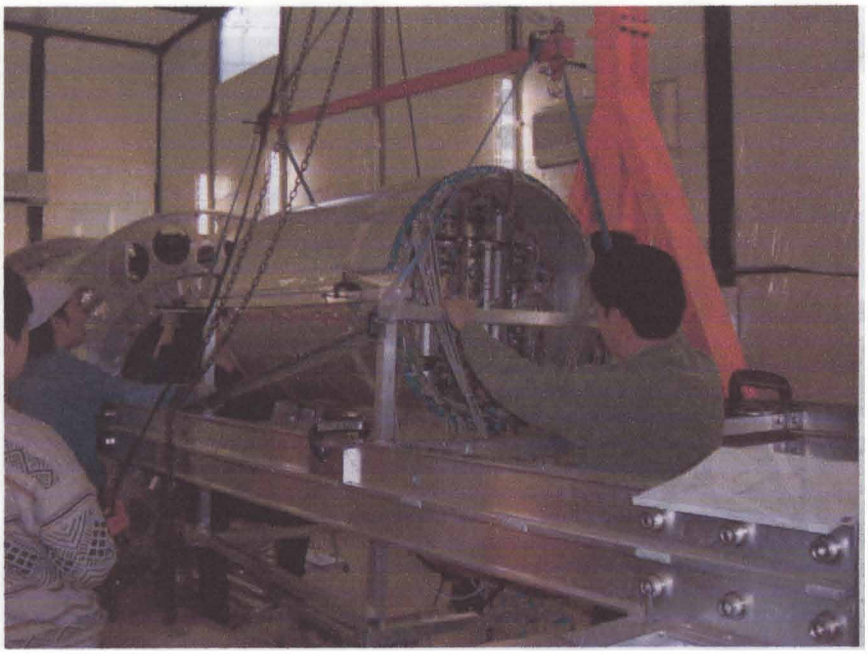

Figure 2.2: Installation of JET/IDC chamber

drift chambers (IDC) before entering a central jet type drift chamber (JET). An aerogel Cherenkov counter (ACC) was placed between the upper TOF hodoscope and the cryostat. Between the lower TOF and the lower ODC, a lead plate was installed. Scintillation fiber hodoscopes (Scifi) were attached to insides and outsides of the ODCs. All these detector components were contained in a pressure vessel.

Figure 2.2 shows a photograph of installation of JET/IDC chamber. Figure 2.3 shows the cross-sectional view of the BESS-2001 instrument.

Solenoidal magnets covering detector system have often been disfavored in previous cosmic ray experiments [10, 11, ?, 13, 14] because of the unavoidable material in the particle passage. However, a thin superconducting solenoid developed at KEK[15, 16, 17] enabled us to adopt this horizontally cylindrical configuration.

The cylindrical configuration, usually used in the high energy collider experiments, has many advantages in the cosmic ray application too. The strong and uniform magnetic field is generated in a large volume inside the solenoid where a large acceptance tracking system is installed. Therefore good momentum resolution is easily obtained while keeping the whole detector size compact. The detector has a wide-open geometry, and the JET can fully "visualize" the incoming tracks or any interactions inside the apparatus. Inelastic interactions accompanied by several secondary tracks can easily be

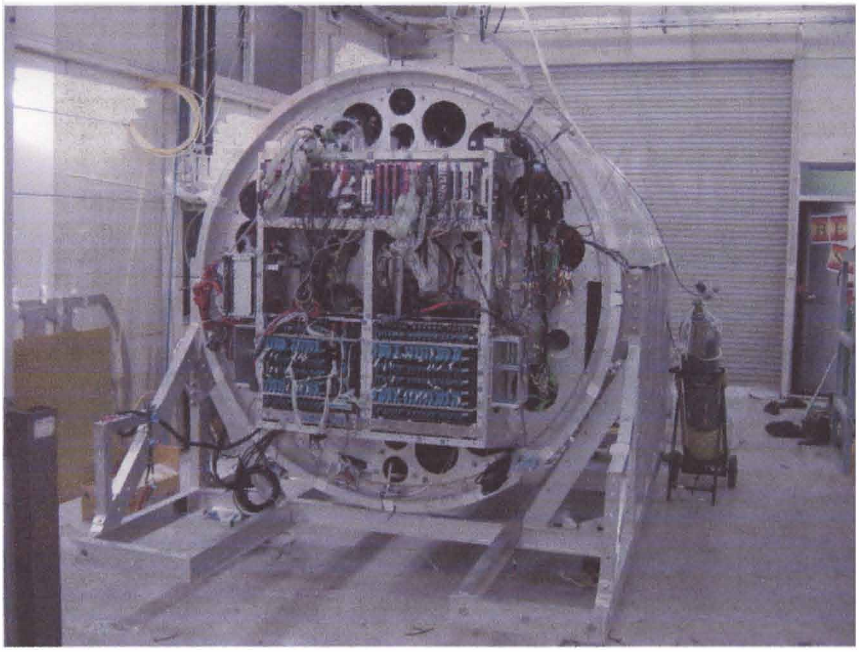

Figure 2.3: Cross-sectional view of the BESS2001 instrument

identified (see Figure 2.4). A probability of charge mis-identification due to large angle scattering is negligibly small.

The uniform magnetic field strength over the large tracking volume assures nearly constant geometrical acceptance for wide energy ranges. The acceptance changes only a few percent from the lowest detectable energy (~200 MeV) up to > 100 GeV. The detector performance changes little for various hit positions and incident angles too. These characteristics are essentially important for reliable determination of the absolute flux of the cosmic radiation.

We use hereafter a cylindrical coordinate system; r, φ and z, and a Cartesian coordinate; x, y and z, where y and z being the vertical axis and the axis of the solenoid, respectively.

2.1.2 Particle Identification

Particle identification in the BESS experiment is basically performed by mass reconstruction according to the relation, $m = ZeR\sqrt{1/\beta^2 - 1}$. The rigidity, momentum per charge ($R \equiv pc/Ze$), is precisely measured by reconstructed particle trajectory. The velocity, β, is derived from the path length and the time-of-flight between the upper and the lower layers of the TOF. The energy deposit in the TOF provides the magnitude of the charge, Z, and additional information on the velocity according to the relation, $\mathrm{d}E/\mathrm{d}x$

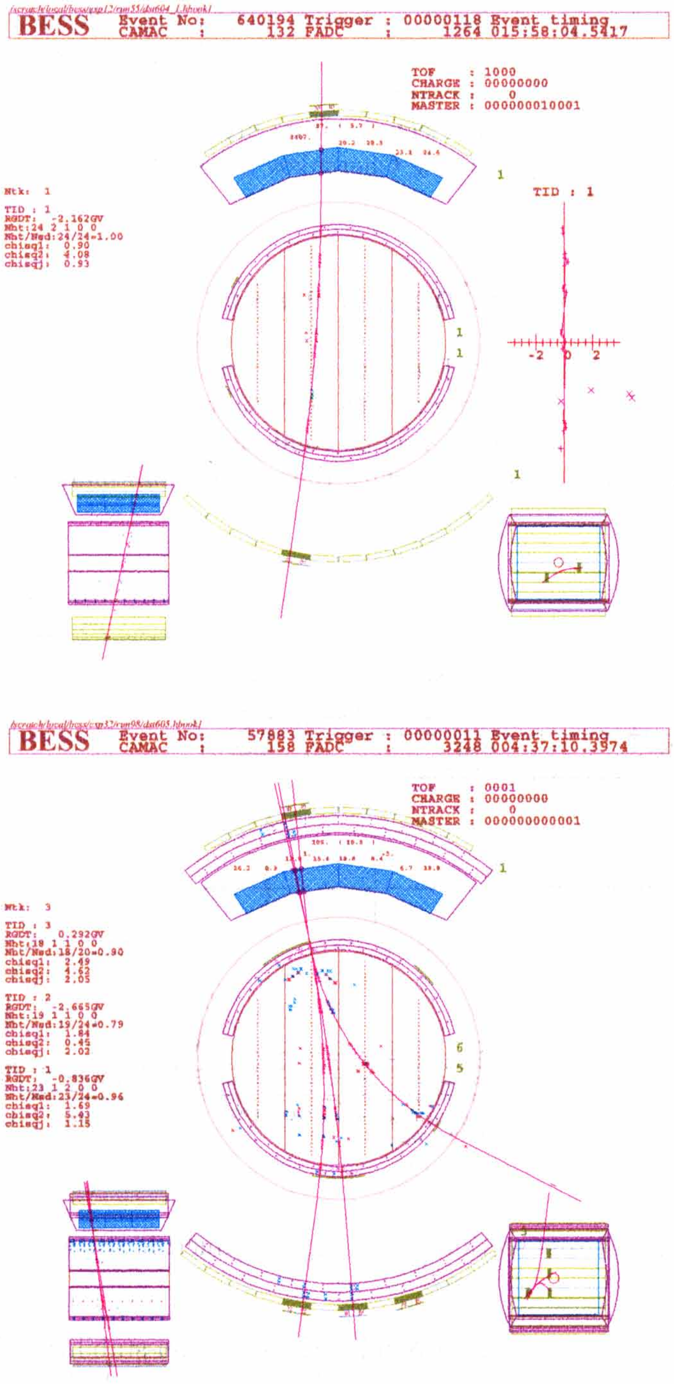

Figure 2.4: Examples of event display collected during the flight: (top) a typical single-track event and (bottom) three-track event showing the interaction at the coil.

$\approx (Ze/\beta)^2 f(\beta)$. The sign of charge is determined by the deflection and the particle direction, up-going or down-going, determined by the TOF. The mass is finally calculated from these measurements.

The separation of muons and electrons from protons is further performed by ACC. Protons of energies below Cherenkov threshold are distinguished from the muon and electrons.

2.2 Superconducting Solenoid

The superconducting solenoid magnet is the central core component of the magnetic rigidity spectrometer. The magnet was specially designed to provide uniform magnetic field in a large solid-angle acceptance with minimizing incoming particle interaction with the magnet wall material[?, 15].

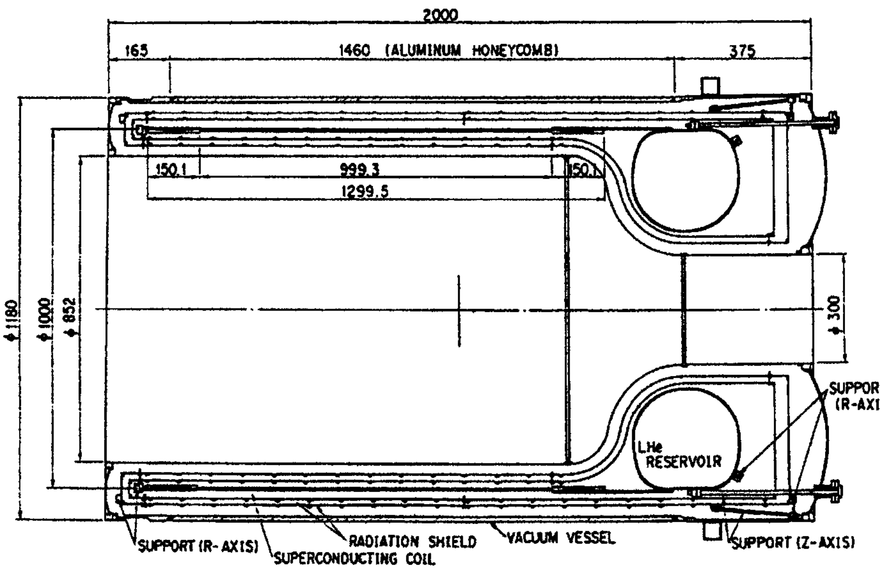

Figure 2.5: Cross section of the superconducting solenoid.

The superconducting coil was wound with aluminum-stabilized NbTi/Cu superconductor in four layers in the central area and in eight layers in both axial ends for a better field uniformity. Figure 2.5 shows the cross section of the solenoid. A central magnetic field of 1.2 Tesla was generated with the field uniformity of 12 % in the central trackers (JET/IDC) with a wall transparency of 0.2 radiation length.[16]

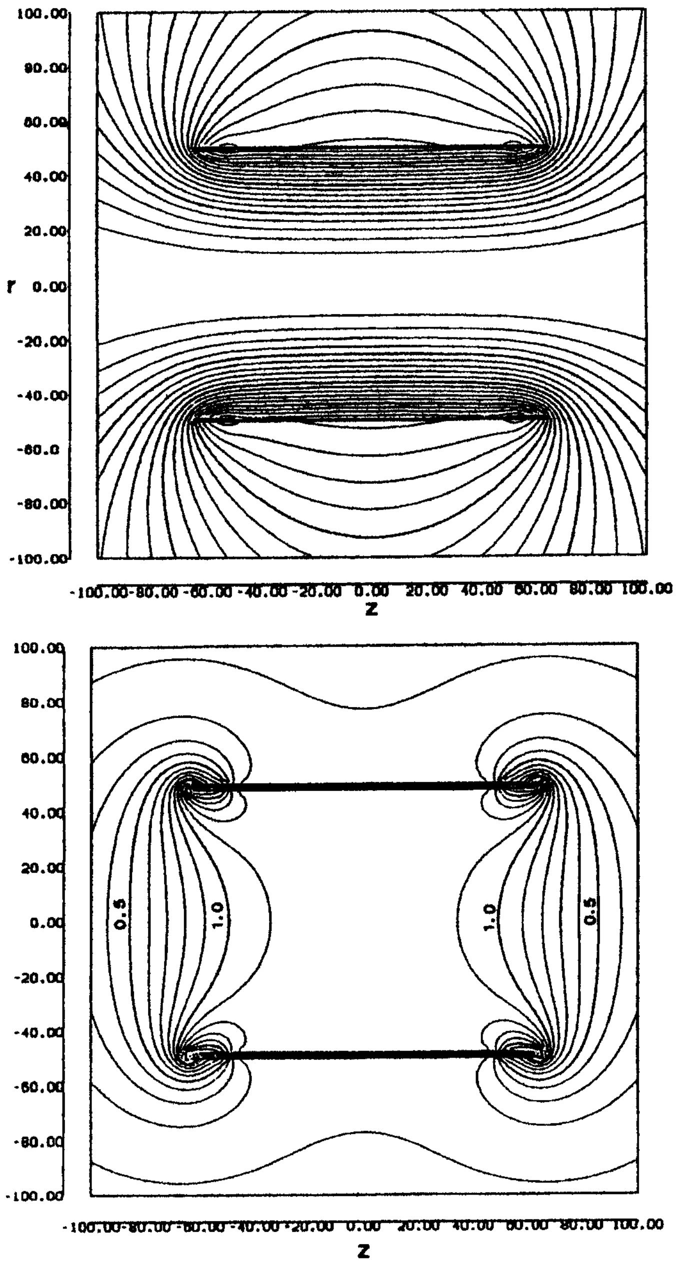

Figure 2.6: Flux line (top) and field strength contour (bottom) of the superconducting solenoid.

Table 2.1: Main parameters of the superconducting solenoidal magnet (MAG).

Dimensions		
Coil diameter	1.0 m	
length	1.3 m	
coil thickness (center)	5.2 mm	
(end notch)	10.4 mm	
Cryostat diameter	1.18 m	
length	2.0 m	
Useful aperture diameter	0.85 m	
length	1.0 m	
Central field	1.0 T	(1.2 T*)
Current	430 A	(520 A*)
Stored energy	815 kJ	
Wall thickness	0.22 X_0 per wall 4.7 g/cm^2 per wall	
Total weight	430 kg	
Conductor	Nb/Ti/Cu	
Stabilizer	Pure Al(99.999%)	

$*$Tested

The coil was indirectly cooled by thermal conduction through pure-aluminum strips and the outer support cylinder linked to a liquid helium reservoir located in one end of the solenoid coil. This configuration realized advantages of the minimum wall material in the detector acceptance and also an intrinsic safety protection against a magnet quench with suppressing sudden pressure rising in the reservoir.

The solenoid coil was successfully tested up to a central magnetic field of 1.2 Tesla and was operated at 1 Tesla in the scientific balloon flights[17]. Major parameters of the solenoid magnet are summarized in Table 2.1, and the flux line and the field strength contour are shown in Figure 2.6.

2.3 Tracking

2.3.1 JET Chamber

The JET chamber was located inside the warm bore (0.85 m in diameter and 1.34 m in length) of the solenoidal magnet, providing a particle trajectory in r-φ plane by drift time measurement and in z direction by charge division read-out.

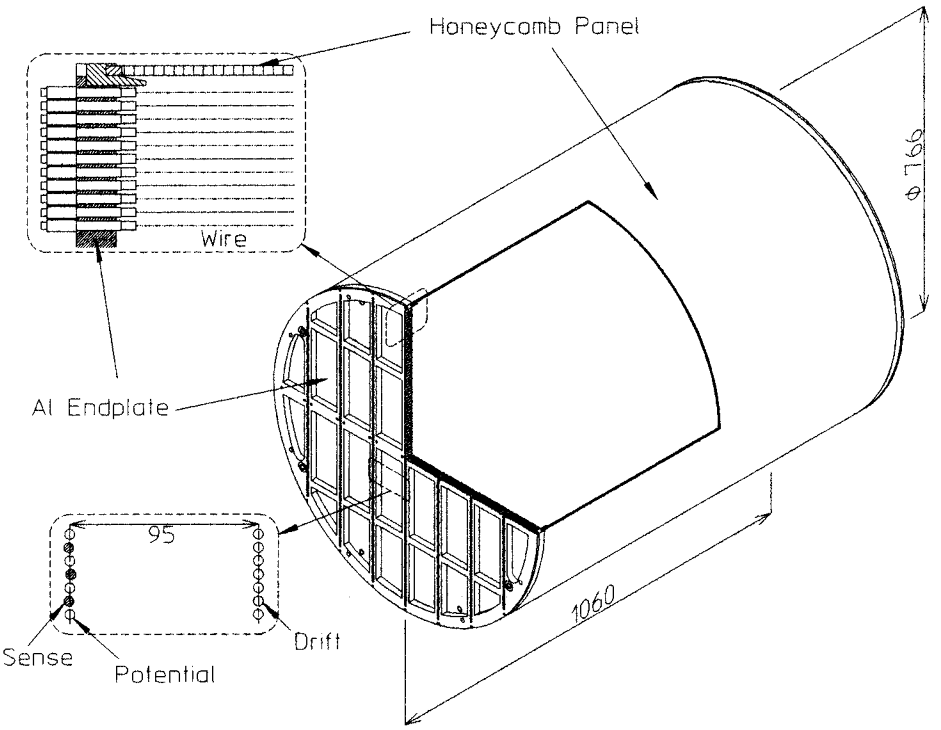

Figure 2.7: Schematic view of the JET chamber.

A schematic view of the JET is shown in Figure 2.7, and its parameters are summarized in Table 2.2.

The sensitive volume of the JET is a cylinder of 1 m in length and 754 mm in diameter. The chamber is subdivided into four sections in vertical by cathode planes in which gold-plated aluminum wires of 200 μm in diameter are stretched at 6.7 mm interval. At the center of each section, there is a signal wire plane in which sense wires (gold-plated tungsten-rhenium alloy, 20 μm in diameter) are equally spaced at 13.4 mm intervals alternated with potential wires (gold-plated aluminum, 200 μm in diameter). Each of the two central (side) sections contains 52 (32) sense wires. In order to resolve left-right ambiguity, the sense wires are staggered by ±500 μm from the center plane defined by the potential wires. The maximum drift distance of one section is 95 mm.

The high voltages of the potential and cathode wires are -2.85 kV and -10.80 kV, respectively. The sense wires are kept at ground level. The electric field strength in the drift region is about 0.85 kV/cm, which corresponds to the maximum drift time of 12.3 μs using a gas mixture described below.

Every wire is positioned and fixed by a feed-throughs, which is stuck in

Table 2.2: Parameters of tracking chambers.

JET	
Shape and Size	Cylindrical, 766 mm$\phi\times$ 1060 mm
Sense wires	W/Re(Au plated), 20 μmϕ, 176 wires
Tension	0.392 N
Wire spacing	13.4 mm (y), Staggering of $\pm$500 μm (x)
Potential wires	Al(Au plated), 200 μmϕ, 196 wires
Tension	2.94 N
Wire spacing	13.4 mm
Cathode wires	Al(Au plated), 200 μmϕ, 301 wires
Tension	2.94 N
Wire spacing	6.7 mm
Maximum drift length	95 mm
Spatial resolution	175 μm (x), 2.0 cm (z)
Maximum Detectable Rigidity	220 GV
IDC	
Shape and Size	Arc-shaped, R =384–420 mm, $\|\varphi\| < 82.0°$, $L = 1060$ mm
Sense wires	W/Re(Au plated), 20 μmϕ, 11/12 wires
Tension	0.392 N
Wire spacing	13.0°
Potential wires	Al(Au plated), 200 μmϕ
Tension	3.43 N
Spatial resolution	220 μm (φ), 470 μm (z)

a hole drilled through the end plate. The feed-through has a Derlin bush for positioning, a brass lead for soldering and a Derlin sleeve for electrical insulation. The inner diameter of the bush is 270 μm for potential/cathode wires and 80 μm for sense wires enabling us to achieve a positioning precision better than 50 μm. The wire tensions are adjusted to be half their elastic limits to allow for deformation of the chamber due to temperature variation and acceleration impact.

In order to reduce weight and material, the wall of the cylinder was constructed with a honeycomb plate. It was made of 6 mm thick Aramid core with skins of 125 μm thick copper plated Kapton sheets. The field shaping strips with various widths depending on the azimuth were etched on the inner surface of the cylinder. Resistors connect the neighboring strips with proper resistance to form a uniform drift field.

The end plates were made of 20 mm thick aluminum, rigid enough to support a total wire tension of 1.53 kN. From the weight consideration, many pits of 15 mm depth were scooped out in the end plates. The pits are used to house preamplifier boards. Inside the end plates, G10 boards with copper-etched field shaping patterns were glued to complete the field cage.

The total weight of the JET chamber is about 80 kg. The average material passed by a penetrating particle is 0.48 g/cm^2 including two chamber walls and wires.

2.3.2 Inner Drift Chambers

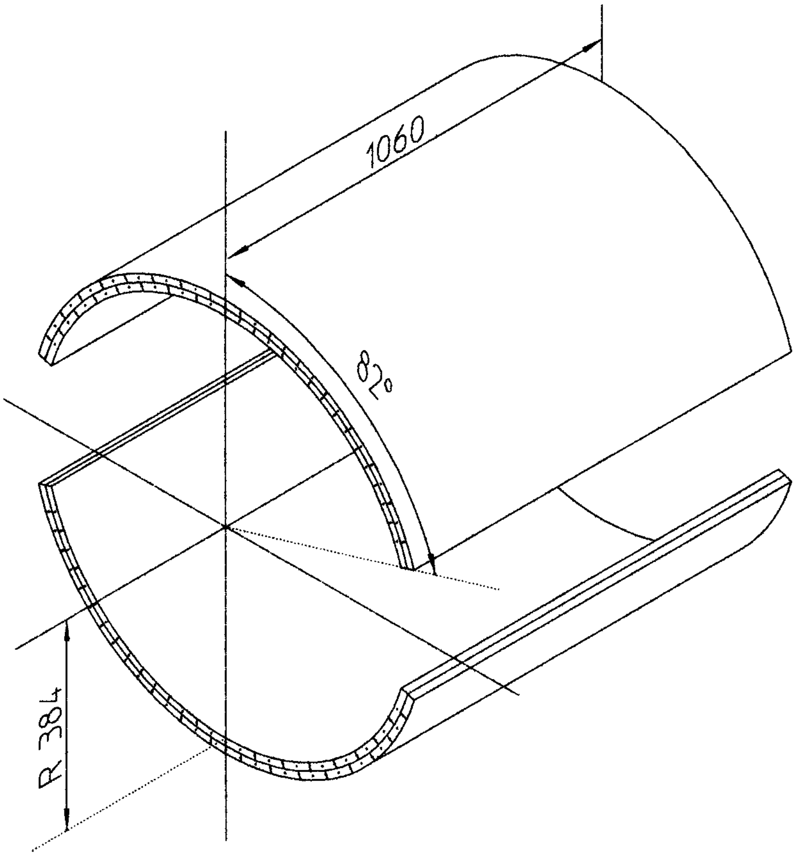

Figure 2.8: Schematic view of IDC.

The IDCs, located just inside the cryostat, provide track hit positions in the z-direction with high precision through diamond-shaped vernier strip readout as well as in the azimuthal direction through drift time measurement. Their cell structure in the azimuthal direction is also used by the second-level trigger for track-pattern recognition making a quick determination of the angular deflection and the sign of charge of incident particles.

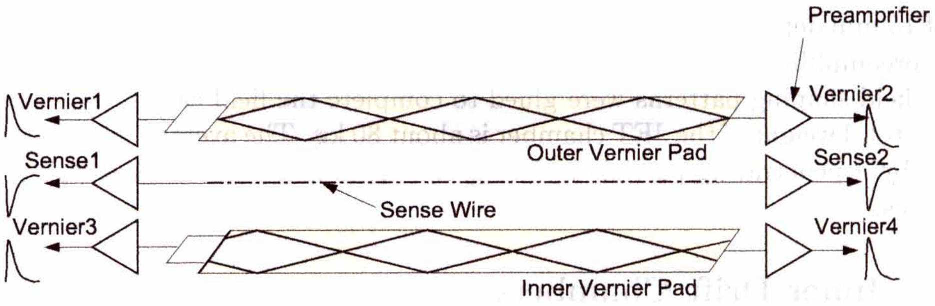

Figure 2.9: Read-out scheme for IDC signals.

The IDCs are arc-shaped drift chambers with identical double layer structure except for their dimensions. A schematic view of them is shown in Figure 2.8 and main parameters are summarized in Table 2.2.

Each chamber is composed of four Aramid-core honeycomb panels with G10-plastic end and side plates. The skins of the honeycomb panels, copper-plated Kaptons sheets, electrically isolate the two layers. The sensitive volume of each layer is 12 mm thick and is divided into cells by alternately stretched sense and potential wires. The wires are fixed by the same feed-throughs as used in the JET at an interval of 6.50° in azimuth for the IDC, corresponding to a half-cell size of about 50 mm. The wire position in one layer is shifted by a half-cell pitch with respect to the other layer. By adopting this double layer configuration, the left-right ambiguity can be automatically resolved and quick hit cell information is available by making a coincidence of the two overlapping cells.

Field shaping strips of 1.5 mm in width are etched on the inner surface of the copper-plated Kapton sheet at a 3 mm interval. The strip pattern on opposite side of the IDC layer is slightly shifted so that the direction of the electric field is tilted by 5.5° with respect to the drift (azimuthal) direction in order to compensate for the Lorentz angle arising from the magnetic field of 1 Tesla.

Vernier-cathode-strip pairs of 7.5 mm width are etched on both sides of the sense wires. As shown in Figure 2.9, each pair consists of a diamond-shaped inner strip and an outer strip with complementary shape. A cycle length of the pattern is 100 mm for the IDC. The strip patterns on opposite sides are shifted by a quarter pitch along the z-direction to give a precise hit coordinate. There are four strips in total associated to a single sense wire, which are read out separately.

In order to set a potential of vernier strips at ground level, the high voltage applied to the sense wires is +2.68 kV and the high voltage to the potential wires is −4.06 kV for the IDC. The average electric field in the drift region is 0.8 kV/cm.

Since the chamber structure is fragile against over-/under-pressure, a 0.5 mm thick aluminum plate is glued to the outer surface of the chamber for mechanical reinforcement.

2.3.3 Outer Drift Chambers and Scintillation Fiber

The ODCs were cell-type arc-shaped drift chamber as same as IDC, and installed between TOF and the solenoid.

Each ODC consists of two layers in a radial direction. In each layer, two sense wires are stretched at the center of each cell. One ODC provided four hit points along the track. Spatial resolution of each hit is 150 μm in the r-ϕ direction.

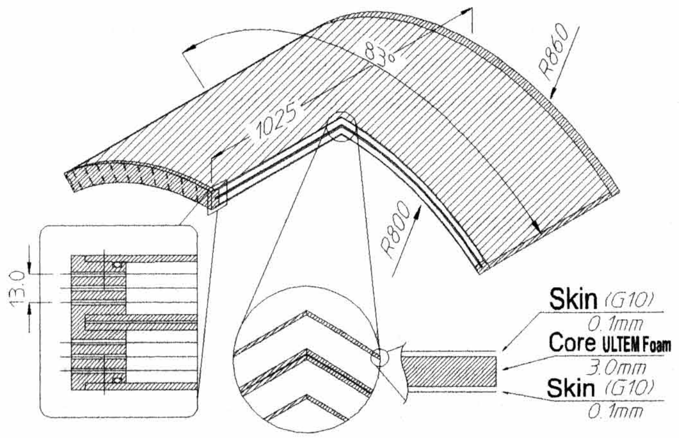

Figure 2.10: Schematic view of ODC.

In order to carry out real-time calibration of the ODCs during flight, a scintillation fiber detector covers outer and inner surface of one cell of the ODC.

Using these ODCs and scintillation fibers track length became almost doubled from JET/IDC's track length, and we can measure higher energy particles. But in the present analysis, we did not use these ODCs.

2.3.4 Chamber Gas

The JET, the IDCs and the ODCs are filled with the same gas mixture of CO_2 90 % and Ar 10 %, called "slow gas". The drift velocity at 1 atm and with an electric field of 1 kV/cm is about 8.1 mm/μs. Owing to its slow drift velocity and small longitudinal diffusion of drift electrons, good spatial resolution and good double-track separation can be achieved by using reasonably low power and moderate speed readout electronics, at the expense of delicate control of high voltages and pressure of the gas.

The pressure vessel is also filled with the same chamber gas. Thus any chamber suffering a small leak would still be operational during flight. The valves at the inputs and the outputs of the chambers are closed just before launching, and the chambers are operated without gas circulation during a one-day flight.

2.3.5 High Voltages

High voltage power supplies are compact DC-DC converter modules. The high voltages are applied to the chambers through low-pass filters. The output voltage is adjusted by an external resistor and is switched on/off by a command issued from the ground station. The ramping profile of the output voltage is internally controlled so that it takes fifty seconds before reaching the nominal value. The output voltage and current are monitored by the monitor system. A small iron cylinder inside the module shields magnetic components.

2.3.6 Readout Electronics

Preamplifiers

The signals from the sense wires of all the chambers and the vernier strips of the IDCs are fed to the same type of preamplifiers (Fujitsu MB43458), which can cope with both polarities, negative signals from the wires and positive signals from strips. The preamplifier chip is a monolithic IC with four equivalent amplifier circuits with a gain of 7 mV/μA and 96 Ω input impedance[?]. Typical pulse height of the preamplifier output is 10 mV while the noise level remains below 0.2 mV.

The preamplifier boards for the JET have four or three amplifier chips (16 or 12 channels/board). They are individually buried in the pit of the aluminum end plates covered with aluminum plates for noise shielding. Because of the high power consumption of the digitizing electronics, all the wires of the JET could not be read out. The number of channels was compromised considering a required momentum resolution and the total power consumption. In each of the two central (side) sections, 24 (16) sense wires out of 52 (32) are read out. And the signals of 16 (8) sense wires out of 24 (16) are read at both ends for charge division. Up to 24 points in r-φ and in z are sampled for an incident charged particle penetrating the central region of the JET.

The preamplifier boards for the IDCs have a single chip. They are attached to the end plates of the chambers and are housed in a copper shield cage. The IDCs are read out from a single end of each sense wire and four strips.

FADC

The output of preamplifiers of the JET wires and the IDC vernier strips were fed to flash analog-to-digital converter (FADC) modules. The FADC module has 16 input channels. 23 modules (368 channels in total) were housed in two EUROCARD industry standard crates. The 128 channels were used for JET chamber readout, the 176 channels for IDC vernier strips and the remaining 64 channels for ODC readout.

The FADC system was newly developed to meet the requirements of this experiment, low power consumption and fast data compression[25]. The input signal to the FADC module is further amplified by a main-amplifier with a gain of 10 (40) for the JET (IDC). It is digitized by a FADC (HITACHI HA19211BMP) with 8-bit resolution at a rate of 28.5 Msps for a duration of 18 μs (512 samples in total). A digital comparator then compares the digitized data with a preset value and only data above the threshold are written in a FIFO memory. This zero suppression process is executed synchronously with the digitization on each FADC channel without costing any extra time. Then a data compressor module in the FADC crate further compresses a sequence of the non-zero data train into a small number of useful information; the channel number, the total charge of the pulse, the timing of the signal arrival, the pulse width and the first two raw data of the pulse. Thus the data volume was reduced by a factor of 3 in average. For a typical single track event, the data compression process took less than 200 μs.

Amplifier/Discriminator

The sense wire signals from the IDCs are further amplified and discriminated by amplifier/discriminator (A/D) modules. The discriminated sense wire signals from the A/D modules are used to issue a second level trigger. A detailed discussion on the trigger process is made in Section 2.6.

2.3.7 Performance

The transverse and total rigidity of a particle is determined by fitting the three-dimensional hit positions measured by the drift chambers. Energy loss in the chamber gas is also measured using the charge information of the JET. To obtain hit positions in r-φ plane, the drift velocity was calibrated using the flight data. Although the drift length is approximately proportional to the drift time, some nonlinear effects exist due to distortion of the electric field. This non-linearity was corrected by fitting the x-t relation with a third-order polynomial function.

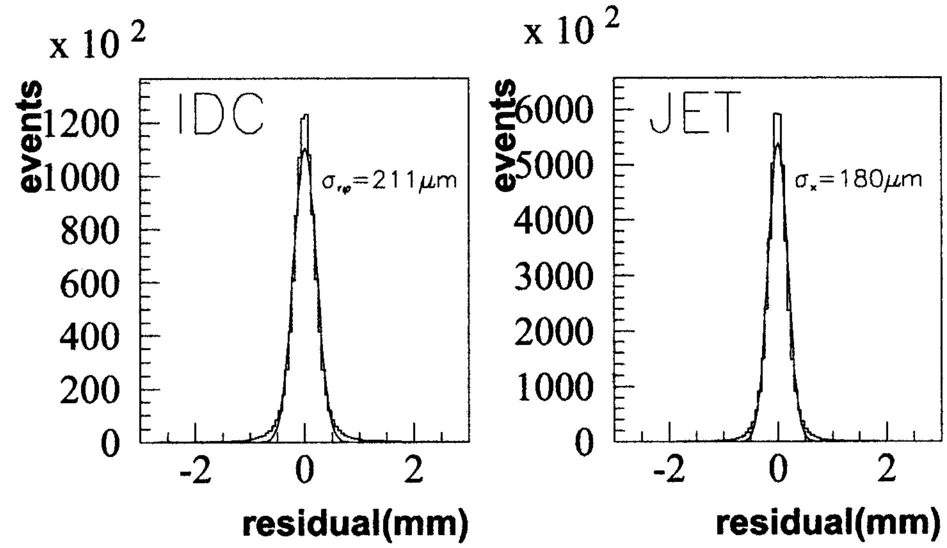

Figure 2.11: Fitting residuals for (right)JET and for (left)IDC in r-φ plane.

r-ϕ Position Measurement

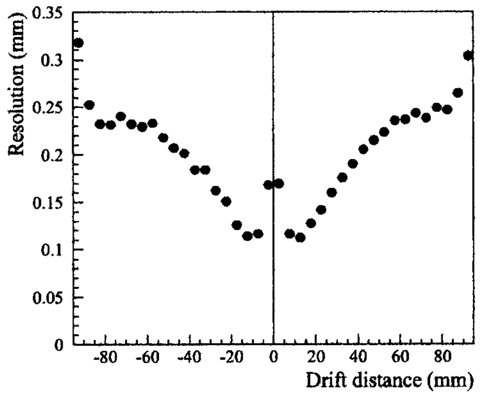

Figure 2.12: JET chamber r-φ resolution as a function of the drift distance.

The JET and the IDCs determine the rigidity of a track. First, good hits, defined as hits with enough charge and pulse width, are selected. They are connected to form a candidate trajectory. The transverse rigidity, R_{T}, is then calculated by applying a circular fitting to those hits associated to the track. This procedure is iterated adding new hits close to the track and dropping deviant hits. The resultant R_{T} is then corrected for the non-uniformity of the magnetic field. From a Monte Carlo simulation for various trajectories in the exactly calculated magnetic field, correction factors to the rigidities were derived as a function of track position, inclination, and rigidity. The correction factors reproduce the original rigidities within a typical accuracy of ±0.2 % for tracks within a fiducial volume, the central sections plus the inner half of the side sections of the JET.

To determine the total rigidity, R, we obtain a dip angle, θ_{dip}, which is defined as an angle between the total rigidity vector and r-φ plane. A sinusoidal fitting in r-z plane is applied to the selected hits in the JET and the IDCs iteratively, as in the r-φ fitting, to eliminate irrelevant hits. All possible combinations of IDC hits are examined, since the IDCs provide only the z-positions within a vernier strip pattern cycle of 100 mm. The resultant θ_{dip} is the one obtained from the combination which gives the minimum χ^2 value. The total rigidity R are derived from R_{T} and θ_{dip} as $R = R_{\mathrm{T}}/\cos\theta_{\mathrm{dip}}$.

Based on the residual distributions shown in Figure 2.11, the overall spatial resolutions of the JET and the IDCs in r-φ plane are respectively estimated to be 175 μm and 187μm. Figure 2.12 shows drift length dependence of the spatial resolution.

z-position Measurement

The z-coordinate of a hit position is obtained by using the charge division of the JET, and the vernier strip readout for the IDCs.

First we roughly determine hit positions along the sense wires of the JET by the charge division method. The z-coordinate of a hit position is derived from the charges read out at both ends of the hit wire (Q_a and Q_b). Hit position (z) is given by

$$\frac{z}{L} = \frac{(R+r)Q_b - rQ_a}{R(Q_a + Q_b)}$$

where L and R are the length and the resistivity of the sense wire and r is the input impedance of the preamplifier. We obtained the z-position resolutions of 11.6 mm for single-charged particles (Figure 2.13), by the JET, which are precise enough to identify the particular vernier strip cycle of the IDCs hit by a track.

After the coarse determination of the z-coordinate, we use the vernier strips of the IDCs to get the z-coordinate precisely. The hit position along the z-axis is measured using the signal charges induced on the associated vernier-strip pairs. We define a normalized charge ratio, ε, for a pair of vernier-strips, A and B.

$$\varepsilon_{\mathrm{I(O)}} = \frac{Q_{\mathrm{AI(O)}} - Q_{\mathrm{BI(O)}}}{Q_{\mathrm{AI(O)}} + Q_{\mathrm{BI(O)}}}$$

where $Q_{\mathrm{AI(O)}}$ and $Q_{\mathrm{BI(O)}}$ denote the charges induced on A and B of the inner vernier-pad pair (outer vernier-pad pair). The ε parameters are linearly

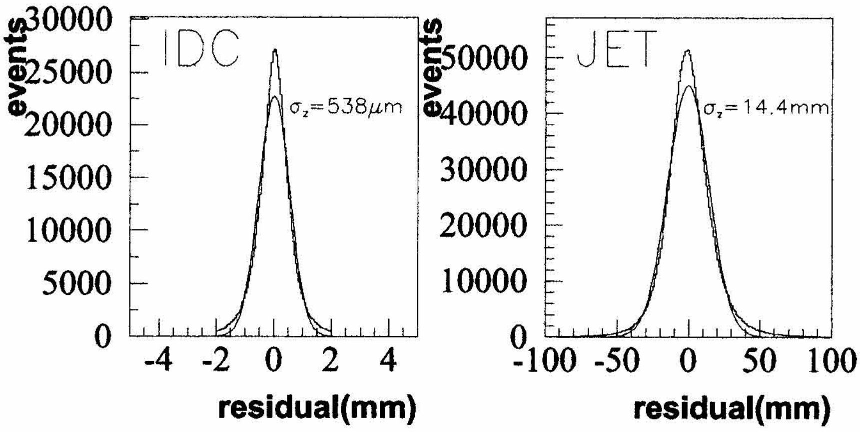

Figure 2.13: Residual distribution of the JET and IDC along the z-coordinate.

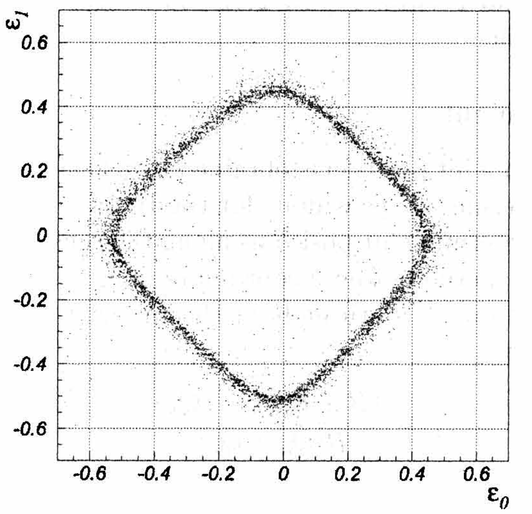

Figure 2.14: Scatter plot of the ε parameter of the inner (ε_I) and outer (ε_O) pad.

related to the z-axis position of the avalanche point. Figure 2.14 shows a scatter plot of ε_I vs. ε_O for the IDC vernier strips. A circuit along the round-square locus corresponds to a vernier-strip pattern cycle of 100 mm along the z-axis. We can derive the z-coordinate of a hit position by comparing a measured ε pair with the numerically calculated values. The deviations of the measured ε values from the calculated line are translated to the z-position resolution, giving the resolution of 422 μm by the IDC vernier strips as shown in Figure 2.13. The performance of the tracking system is summarized in Table 2.2.

Energy Loss Measurement

The pulse height measurement of the JET provides independent and redundant information as for particle identification. However, it was found that the $\mathrm{d}E/\mathrm{d}x$ resolution of the JET deteriorates, particularly in the higher signal charge region, due to the space charge effect. After a detailed study of the effect, a correction method for saturation was obtained as follows.

The saturation strongly depends on the inclination angle θ_{y-z} between the track and the z-direction, and also slightly depends on the inclination angle $\theta_{r-\phi}$ of the track in the r-ϕ plane. Using pure proton and helium samples, the energy deposit was derived from the two-dimensional function of the θ_{y-z} and the measured charge, and then corrected for the $\theta_{r-\phi}$ dependence. The correction for the drift length is then applied to obtain the energy loss $\mathrm{d}E$. In order to remove the Landau tail, a truncated mean method is adopted, i.e., the hit points in lower 10 % and higher 50 % are eliminated, and the mean $\mathrm{d}E/\mathrm{d}x$ is calculated using the rest of the hit points.

Figure 2.15 shows the $\mathrm{d}E/\mathrm{d}x$ measured by the JET for an unbiased data sample. We can clearly distinguish protons, muons/pions/electrons, deuterons, and helium nuclei. The truncated mean method effectively removes the higher tail of the $\mathrm{d}E/\mathrm{d}x$ distribution. The resultant $\mathrm{d}E/\mathrm{d}x$ resolution was 13 % for single charged particles.

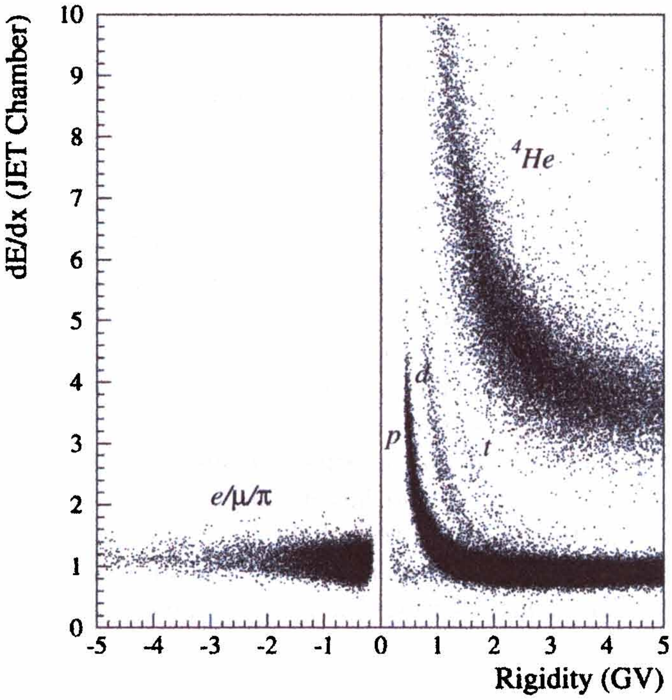

Figure 2.15: dE/dx measurement by JET.

2.4 Time-of-Flight

2.4.1 TOF Hodoscopes

The TOF hodoscopes consist of ten upper- and twelve lower- plastic scintillation counter paddles (950 × 100 × 20 mm, BICRON BC-404). A light-guide (Fig. 2.16) made of UV-transparent acryl plate(Mitsubishi Rayon) is affixed to the scintillator with optical epoxy(BICRON BC-600), connecting each end of a counter to a 2.5-in.fine-mesh magnetic-field-resistant photomultiplier tube (PMT), i.e., a Hamamatsu R6504S assembly type. To minimize the loss of photo-electrons in the PMT caused by the magnetic-field, PMTs are placed tangential to the acryl plate such that the angle between their axis and magnetic field lines is less than 16°. Ends with attached light-guide are fit into circular holes in an aluminum plate, and four springs (Fig. 2.16) are used to prevent separation from a light-guide. A 1-mm-thick silicon pad (Shin-Etsu OF113) lies between the light-guide and PMT to minimize shock and vibration during shipping, launching, and parachute landing. Connection points on both sides of the pad are coated with optical grease (Shin-Etsu optseal, refractive index n = 1.47).

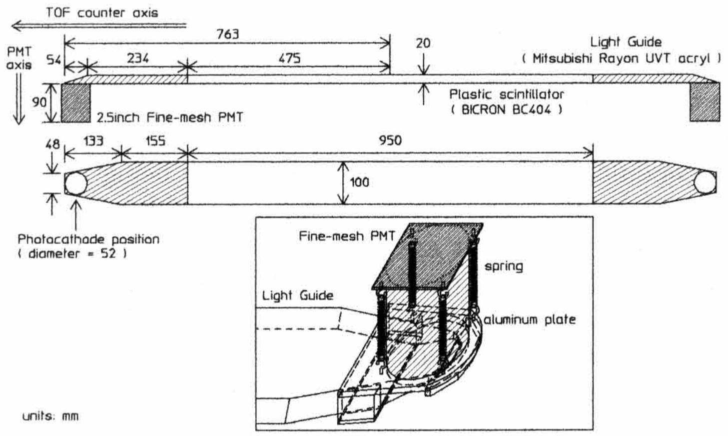

Figure 2.16: Overview of a TOF counter.

To determine the most suitable light-guide shape regarding timing resolution and effective [20, 21] number of photoelectrons (N_{pe}) , we investigated various fish-tail-shaped light-guides using a simulation code (GUIDE7 [22]) in conjunction with cosmic-ray and beam test data, which ultimately allowed us to optimize the angle and shape of the planes. Briefly, after selecting three shapes based on simulation results and cosmic-ray data, the best was determined using the results of beam tests.

The 2.5-in. FM-PMT has the bialkali (Sb-Rb-Cs, Sb-K-Cs) photocathode of which the effective diameter is typically 52 mm resulting to 2.01 times as large compared to that of the corresponding 2-in. one used in the '95 flight. It exhibits a wide sensitivity for wavelengths ranging from 300 to 650 nm, while also well matching the scintillator light spectrum which has its maximum emission at 408 nm. The FM-PMT has 19 dynodes situated about 0.8 mm apart. Electrons are accelerated by parallel electric fields between the dynodes; hence allowing the device to be used in a magnetic field if the direction of the magnetic field is parallel to the PMTs longitudinal axis. The signal from the anode provides timing information and that of the 19th dynode is used as a first-level trigger. Signals from 18th dynodes are used to obtain the energy loss ($\mathrm{d}E/\mathrm{d}x$) of incident particles. The signal from the former dynode is used for highly charged particles.

2.4.2 Electronics and Signal Processing

The output signals from the TOF counters were used for three different purposes; timing measurement, charge measurement and first-level trigger generation. To avoid the interference in the electronics with each other, three signals extracted from the anode, 18th and 19th dynodes were utilized for the above purposes, respectively.

The anode signals were used to issue STOP pulses for timing measurements, because they have the highest pulses suitable for the discrimination. The leading-edge type discriminator was implemented in a 16 channel single-width CAMAC module developed for this experiment, being composed of ECL comparators and differential drivers for output STOP pulses. Threshold levels were set to 15 mV, that are about 1/60 compared to the anode pulse-heights of minimum ionizing particles (MIPs). Pulses from the discriminators are fed into CAMAC TDC module [?], which has a 12 bit resolution with the conversion gain of 25 ps/count.

Every 18th dynode signal is distributed, after converted its polarity by a pulse-transformer (with a low permeability material core) and delayed by a air-core delay-line, to the CAMAC ADC module [?] for charge measurement during a common gate of 250 ns.

The 19th dynode signals were used to generate the first-level trigger, from which START pulse was issued for digitization. Concerning the trigger process, details are discussed in Section 2.6.

2.4.3 Principle of timing measurement

We discuss here on the crossing time of a particle and time-of-flight, i.e., its difference between upper and lower layers of TOF counters of the BESS spectrometer including the details of their deriving processes. In the following discussion, we assign the numbers 1 and 2 to the test counter PMTs.

PMT signals have the time jitter associated with pulse heights, so called the 'time-walk' effect [28, 29]. Therefore the measured TDC time must be corrected for the time-walk effect(the time-walk correction). The time-walk corrected timing for PMT i, t_{ic} is expressed as,

$$t_{ic} = t_i - W_i/\sqrt{q_i} \tag{2.1}$$

where t_i, q_i and W_i are respectively the measured TDC time, the measured charge of the PMT signal, and a correction parameter fitted from data.

Using the time-walk corrected timings for each PMT, we then define the crossing time based on the hit position and the timing information. The hit position of the counter is defined using z coordinate along the counter's longitudinal direction as shown in figure 2.17 where the counter center is defined as $z = 0$. The crossing time of a particle in this paper is the timing based on the reference timing, T_{ref} which is subtracted as the offset timing and determined by the TDC common start. We define the crossing time for PMT1,2 of a counter, $T_1(z)$ and $T_2(z)$ to be

$$T_1(z) = t_{1c} - (\frac{L}{2} - z)/V_{eff} - T_{ref} \tag{2.2}$$

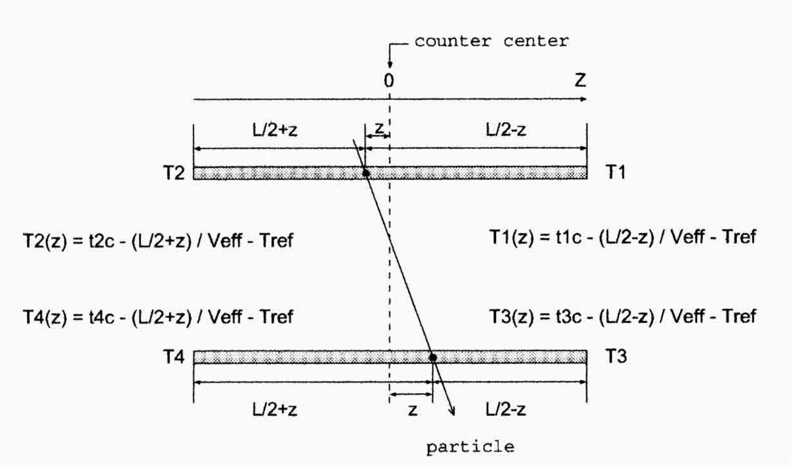

Figure 2.17: The definition of z coordinate and crossing time.

$$T_2(z) = t_{2c} - (\frac{L}{2} + z)/V_{eff} - T_{ref} \tag{2.3}$$

where $t_{1c,2c}$, and T_{ref} are respectively the time-walk corrected timings, reference timings; while z is the hit position of the counter, L the length of the counter including light guides, and V_{eff} the effective velocity of light in the scintillator. The measured root mean square (rms) of $T_1(z)$ and $T_2(z)$ are denoted as σ_1, σ_2, respectively. We use $1/\sigma_1{}^2$ and $1/\sigma_2{}^2$ as the weight of the combination of $T_1(z)$ and $T_2(z)$, respectively, for crossing time measurements.

We then construct the weighted average [30] of crossing time measurements, $T_{w.a.}(z)$ as follows:

$$T_{w.a}(z) \equiv \frac{T_1(z)/\sigma_1{}^2 + T_2(z)/\sigma_2{}^2}{1/\sigma_1{}^2 + 1/\sigma_2{}^2} \tag{2.4}$$

For upper and lower TOF counters of the BESS spectrometer, the crossing times are calculated as combined timing of two PMTs of a TOF counter by using Eq.(2.4) together with z-position. The TOF of the BESS spectrometer obtained from the data for TOF counter PMTs, T_{tof}, is expressed as,

$$T_{tof} = T_L - T_U \tag{2.5}$$

where T_U and T_L are weighted averages (Eq. (2.4)) of the upper and lower layers of TOF counters, respectively.

2.4.4 Performance of TOF System

TOF data were analyzed with incident angle correction of the ADC counts using scintillator path length, time-walk correction, and correction of timing z-dependence. Figure 2.18 (a) shows the TOF resolutions (ΔT) during the

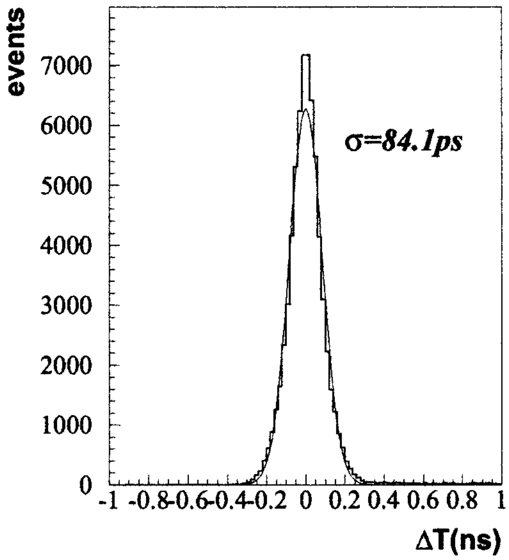

Figure 2.18: TOF performance. ΔT distribution during the ground measurement. Note that the distributions are obtained by using muon samples.

flight. TOF counters have a time resolution of 84.1 psec. The ΔT is the difference between the TOF obtained from the data of TOF PMTs, T_{tof}(Eq. (2.5)), and the TOF expected from the tracking information, T_{trk}, i.e.,

$$\Delta T = T_{tof} - T_{trk} \tag{2.6}$$

$$T_{trk} = \frac{L}{c}\beta_{trk}(R,m) = \frac{L}{c}\frac{p}{E} = \frac{L}{c}\sqrt{(ZR)^2/((ZR)^2+m^2)} \tag{2.7}$$

where L is the path length of the incident particles from upper to lower layer, Z the electric charge of the incident particles, R the rigidity of the incident particles, and c the velocity of light. Due to the error in R being small, the error in T_{trk} (Eq. (2.7)) is also small and the rms of ΔT represents the resolution of the TOF hodoscopes.

2.4.5 dE/dx Measurement

For ADC data analysis, we first subtracted its pedestal, and then normalized for the gains of the PMTs and the ADCs and for the efficiency of light collection, using the MIPs vertically traversing the center ($z = 0$) of the counter which yield about 500 photo-electrons at the photo-cathode. Coarse z-position is obtained from the ratio of these normalized ADC values of the both ends' PMTs, and is used for the matching with the extrapolated trajectory.

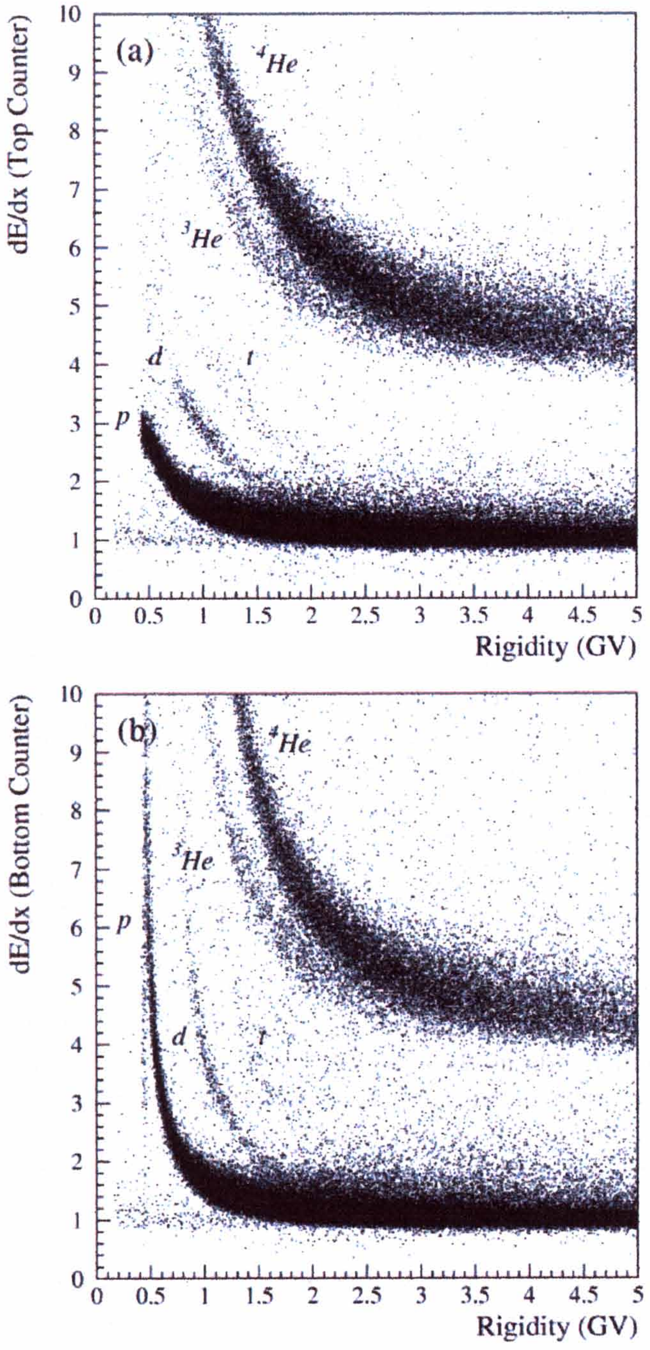

Figure 2.19: Scatter plots of $\mathrm{d}E/\mathrm{d}x$ versus rigidity for down-going positive-charged particles (a) at the top counters and (b) at the bottom counters.

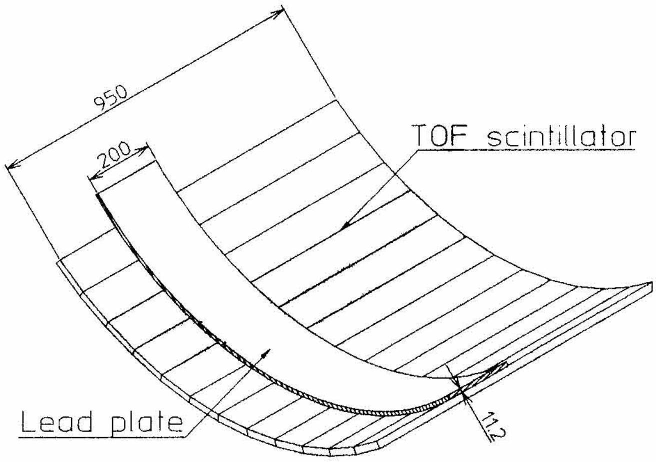

Figure 2.20: Configuration of the lead plate and lower TOF

The dE/dx in a scintillator is calculated, at first, for each PMT by dividing by the traverse length in the scintillator and by correcting for the attenuation of light in the scintillator using the extrapolated trajectory, and we finally adopted the dE/dx by averaging these dE/dx values of both ends. Although the z-position dependence of the attenuation nearly obeys an exponential law and consequently the geometrical average of both ends' ADCs is not expected to depend on the position the obtained value has slightly position dependence especially near both ends. We corrected this effect to produced the better resolution.

Figure 2.19 shows scatter plots of dE/dx versus rigidity measured in the chambers for the top and the bottom scintillators. In the figure are shown proton and helium bands as well as their isotopes, and the energy cut-off due to the energy losses between the top and bottom counters. The dE/dx distributions have longer tail on the upper side (Landau tail). We evaluated that the dE/dx resolution is 24 % at FWHM for all counters for MIPs in the flight data.

In 2001 flight, a lead plate with a thickness of 2 radiation length (11.2mm) was installed above the lower TOF. Configuration of the lead plate and lower TOF is shown in Figure 2.20. We used the lead and the lower TOF as a shower counter to identify muon and electron. As shown in Figure 2.20, a region in which we could use the TOF as shower counter was about 1/5 of the total TOF scintillator region.

2.5 Aerogel Cherenkov Counters

A Cherenkov counter with a silica aerogel radiator (aerogel Cherenkov counter) has been developed in order to improve particle identification capability.

Figure 2.21 shows an overview diagram of the aerogel Cherenkov counter, where the counter consists of a large diffusion box containing aerogel blocks viewed by 46 PMTs densely arranged at the both ends. The unit's weight and the amount of material were minimized using an aluminum-core honeycomb plate as the main structure.

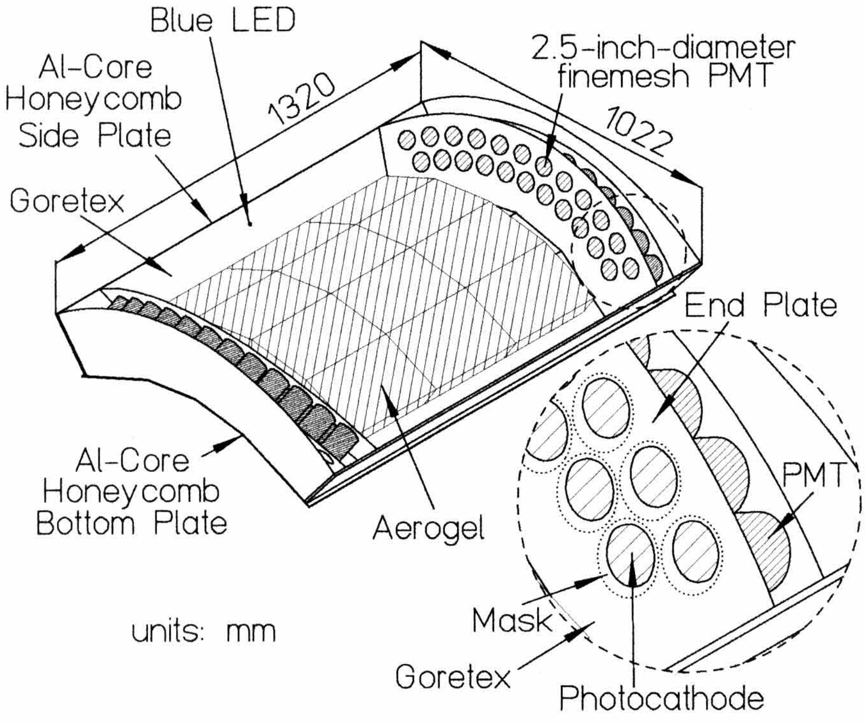

Figure 2.21: Overview of the aerogel Cherenkov counter.

Choosing an effective reflector material is a key aspect in counter design since most photons generated in the diffusion box will undergo numerous reflections prior to reaching the PMTs. We accordingly tested various type of sheet material, *i.e.*, Millipore, Tibex, and Goretex; ultimately finding that Goretex, which exhibits high reflectivity in the short-wavelength region (300–400 nm), is most suitable. From the standpoint of photon collection, this is consistent with the fact that the number of Cherenkov photons is inversely proportional to the square of wavelength; thereby making reflectivity in the short-wavelength region important.

In consideration of operating the counter in a 0.2-T fringe magnetic field, we selected 2.5-in. FM PMTs as used in the TOF hodoscopes.

Readout electronics consists of summing amplifiers that combines 46 PMT signals into 8 channels, which are digitized by a charge-integrated ADC. Blue LEDs (NLPB, NICHIA) with a peak of 450 nm are used to adjust the PMT gain such that all the PMTs provide the same ADC counts per photoelectron. Since PMT gain shows magnetic field dependence, final high-voltage tuning must be done in the counter after exciting the solenoidal magnet to the nominal field. Therefore, the blue LEDs were mounted on the both sides of the side plate at its center point; a configuration allowing PMT gain to be monitored throughout the experiment.

Another consideration concerns the magnetic field itself, since if the PMT axis and magnetic field direction form a nonzero angle θ, then the PMTs lose their effective photocathode area ($S_{\rm eff}$), *i.e.*, some secondary electrons produced at dynode, traveling inside the PMT in the direction of the magnetic field, cannot reach the anode. Accordingly, to avoid losing $S_{\rm eff}$, each end plate on which PMTs were mounted was slanted to reduce θ. The drawback in this approach, however, is that slanting in turn leads the loss of photoelectrons. It is for this reason that during prototype testing we focused our attention on optimizing the angle of slanting such that photoelectron loss is at an acceptable level. The slanting angle was determined to be 24.5° after optimizing photoelectron loss and $S_{\rm eff}$. This slanting angle reduced θ from 39° to about 18° in the lower PMTs and from 43° to about 26° in the upper PMTs. In this way $S_{\rm eff}$ increased by 20% in comparison with not slanting. A mask of Goretex was placed over the front surface of each PMT (Fig. 2.21) such that the photons hitting the insensitive photocathode area formed by residual θ would be reflected back.

2.6 Trigger System

Because of its large geometry factor of the BESS detector, the expected rate of particles penetrating the apparatus is as high as 2 kHz, mostly low energy protons around geomagnetic cut off rigidity. The typical data size of a single track event is 2 kbytes even after the zero suppression process is applied to the FADC data. If all the events were collected, the data rate would be 4 Mbytes/s and the total data size to be recorded during a 20-hour flight exceeds 280 Gbytes, which is beyond the on-board storage capacity. An intelligent trigger system has been developed to reduce the overall trigger rate while interesting events should not be lost.

The trigger generation proceeds in three stages. The first-level trigger (T0 trigger) is a simple coincidence between the upper and lower TOF counters

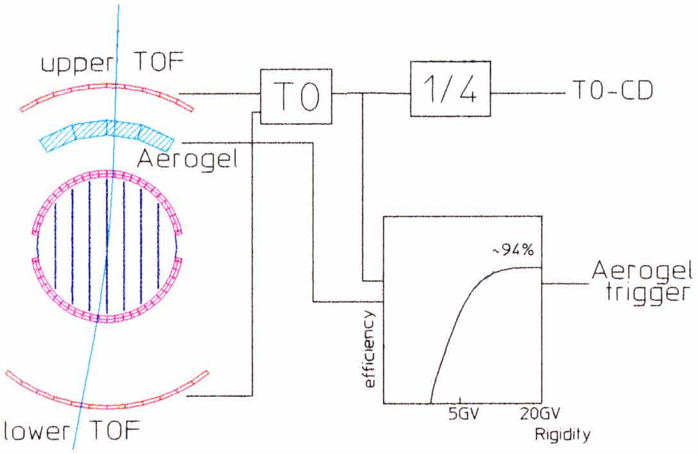

Figure 2.22: Two trigger mode used in this analysis. T0-CD and aerogel trigger.

and initiates digitization of various FADC/ADC/TDC modules and event building processes. The aerogel trigger and the track trigger (TT) are the second level trigger. The aerogel trigger is generated by the Cherenkov light of the aerogel radiator and used for the effective data collection in higher energy region. The track trigger (TT), is a hard-wired logic which determines the coarse track rigidity (deflection^{-1}) based on the TOF/IDC hit information. At TT in order to enrich the recorded data with negative particles such as antiprotons, the majority of the low energy positive tracks were rejected. However, a portion (~1/4) of the all events bypassed the second level trigger and were recorded irrespective of their track rigidity. This event sample forms an unbiased data set and is used to study most abundant protons and helium nuclei and to evaluate various efficiencies and correction factors in the off-line analysis. The Transputer bank composed of the microprocessor cluster performs the third level trigger, which will be described in detail in the next section.

In this analysis we used only T0-CD and aerogel trigger. T0-CD was used in lower energy region and aerogel trigger was used in higher energy region.

2.6.1 First-level Trigger

The first level trigger (T0) was provided by a coincidence between the upper and the lower layers of the TOF counters. A pair of 19th dynode output pulses from PMTs at the both end of each TOF counter were integrated with a time constant of 20 ns and then linearly summed with a simple ca-

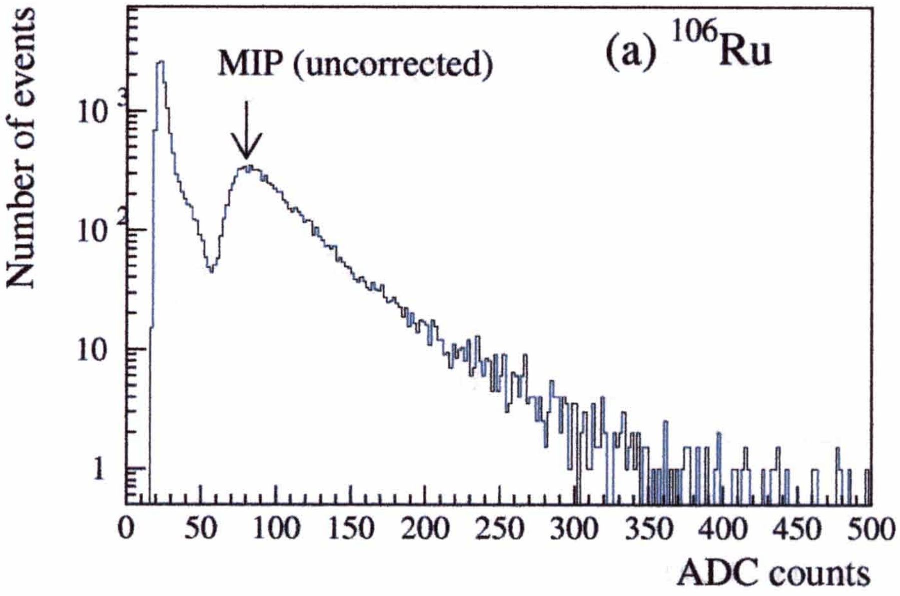

Figure 2.23: Integrated charge distribution of PMT outputs irradiating a TOF counter by a ^{106}Ru radioactive source.

pacitor/resistor circuit. The integration was to smooth the pulse shape so that the timing of the peaks were equalized irrespective of the hit position. The summation was to moderate the trigger efficiency variation along the counter.

The summed signal was discriminated and the output signal is converted to TTL compatible level.

The threshold voltage should be low enough to trigger single-charged particles with good efficiency. It was set at ~1/3 of the pulse height of vertically incident MIPs at the center of the TOF counter. In order to determine the correspondence between the threshold voltage and the integrated charge of the PMT outputs normalized by the MIPs, the TOF counters were irradiated by a radioactive source (^{106}Ru) prior to each balloon flight. Figure 2.23 shows a charge distribution of the events triggered by the RI source in the pre-flight test. The left peak shown in the figure arises from the continuous spectrum given by the RI source which is sharply cut by the discriminator threshold. The right peak corresponds to cosmic ray muons, which are not corrected for the incident angle. From these figures, it was verified that the threshold was set at 1/3 of the MIPs signal.

The discriminated signals in each layer (top and bottom) were ORed, and the T0 trigger was generated when a coincidence was made between the top and the bottom layer. A dedicated T0-trigger module has been developed to minimize the power consumption (1.3 W) and propagation delay and to implement a special function, "count down", denoted CD hereafter. An internal counter counts down on every trigger input starting from a preset value N, which can be set by a CAMAC command, and the output pulse is issued when the count reaches zero. The T0-CD is issued every N-th T0 trigger to collect the unbiased event sample. The rest of the events await subsequent decision made by the TT. In the 2001 flight, the preset value N was set at 4 for the T0-CD.

2.6.2 Second-level Trigger

Aerogel Trigger

For the effective data collection in higher energy region, the aerogel trigger mode was equipped. The aerogel trigger is generated by the Cherenkov light of the aerogel radiator with the refractive indexe of 1.022. The efficiency of this trigger and its energy dependence were evaluated as a ratio of the aerogel triggered events among the unbiased trigger samples. It was about 70% at 6 GeV, 4 GeV/n and 0.7 GeV/c for proton, helium nuclei and muon respectively, and smoothly increased with energy. The efficiency for relativistic particles ($R > 20$ GV, $\beta \rightarrow 1$) was 93.8 %.

Above 7.36 GeV for protons, 3.98 GeV/n for helium nuclei and 0.78 GeV/c for muons, the aerogel trigger events together with unbiased trigger events were analyzed to obtain the energy spectra in higher energy region, where much better statistics were achieved.

Track Trigger

The TT module performs the hit pattern recognition and the track curvature determination. The block diagram of the circuit is shown in Figure 2.24. The TT module was implemented in a double width CAMAC module. An onboard microcode-programmable sequencer controlled the entire operation of the module as described below.

The TT is enabled on receiving the T0 with a delay of $\sim$5 μs, the maximum drift time of the IDCs. A coincidence between the overlapping pair of cells defines a hit cell in each chamber. The TT module is capable of receiving up to 128 inputs corresponding to 32 hit cells in the four detectors (upper TOF, upper IDC, lower IDC and lower TOF). The number of hits in each TOF/IDC is obtained from a look-up-table and is encoded into a 5-bit integer. A 20-bit *N-hit* pattern expresses the number of hits in the TOFs and IDCs.

When the *N-hit* pattern matches with one of the six acceptable patterns, (1,1,1,1) for example, the events are subject to rigidity analysis. The microsequencer scans all the hit cells and picks up a combination of four hits in the four detectors. From the location of hit cells, it then retrieves a 6-bit deflection from a look-up-table. The minimum and the maximum possible deflection corresponding to each hit pattern was calculated prior to the experiment and their mean value was stored in a 16M-bit EEPROM.

There are six different threshold values prepared for the track rigidity selection. A 6-bit rigidity-selection flag is retrieved by specifying the 6-bit deflection. The above process repeats for all the combinations one after another. The TT can be switched to three hit mode in case of some trouble with one of the chambers. By combining the *N-hit* pattern and the 6-bit rigidity-selection flag, the final TT trigger bits are set.

Since the trigger rate and the dead time depends largely on the rigidity threshold values, they should be carefully tuned by a simulation study before the flight.

2.6.3 Master Trigger

The T0 trigger bits, aerogel trigger bits and the TT trigger bits are combined and the final decision to accept the event or not is made in the master trigger (MT) module. The MT module distributes fast clear signals to all the digitizing modules for rejected events. The accepted events are subject to the Transputer bank for further on-line filtering, which is called the third level trigger in the previous section. The CD events are accepted irrespective of the TT trigger bits.

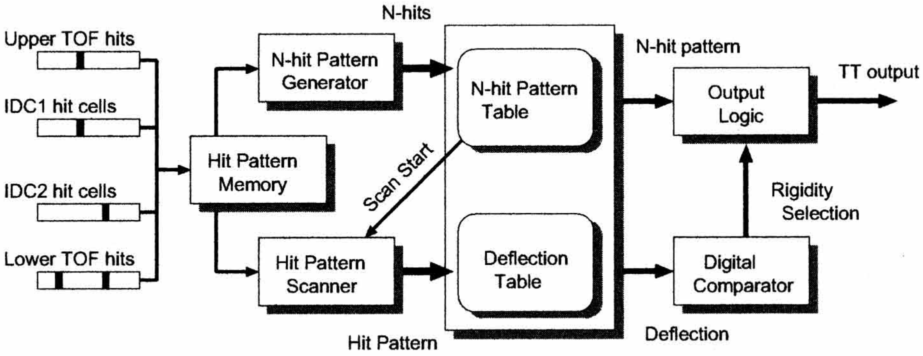

Figure 2.24: Block diagram of TT process.

2.7 Data Acquisition System (DAQ)

The BESS-DAQ is divided into five subsystems as illustrated in Figure 2.25. They were (1) control (2) event-process, (3) data-storage, (4) monitor and (5) communication. A microprocessor Mitsubishi M32R is installed in the control subsystem which manages the other four subsystems via Local Operating Network (LON) and RS232. For much heavier tasks in the event-process, parallel-processing oriented microprocessors, Transputers (INMOS & SGS-Thomson), are employed. The huge amount of event-data are transfered from the event-process subsystem to the data-storage subsystem through Transputer link rather than using LON which has limitation in transferring speed.

In the following subsections, each subsystem is described in detail.

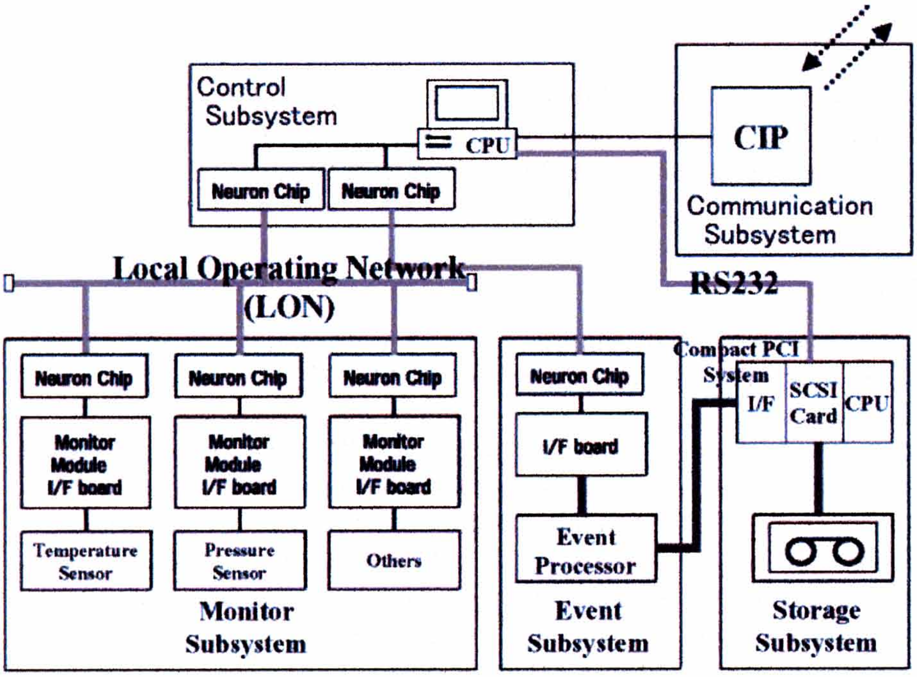

Figure 2.25: Block diagram of the data acquisition system.

2.7.1 Event-Process Subsystem

The event-process subsystem was designed to collect digitized data from front-end electronics of sub-detectors and to build formatted data for an event. The subsystem consisted of a FADC system, a CAMAC system, an event builder (EVB), and a Transputer bank (Figure 2.25). The digitized data from FADC and CAMAC front-end modules were gathered through FADC and CAMAC Crate Controller's (CC) and processed into "an event-data" by EVB. The event-data was sent to the Transputer bank for further on-line filtering.

In the subsystem, a total of 36 Transputers were employed. Each Transputer possesses a processing speed of 20 MIPS and supports execution of parallel tasks. In addition, each Transputer is provided with four serial bus line ports. Two Transputers can be connected with a serial "Transputer link" using these ports and can communicate each other. The Transputer link has a data transfer rate of 20 Mbps[23], but a rate of 1 Mbytes/s has been achieved in our particular application. Each crate controller had a Transputer inside and the Transputer bank contained sixteen Transputers. These were connected with Transputers links to construct a "Transputer network". Programs for the Transputer network are written in OCCAM high level language[24] to utilize Transputer's hardware implementation most effectively.

This unique design enabled high-speed parallel data processing and transferring of the BESS DAQ. Under typical experimental conditions, the subsystem is expected to operate at the event rate of 240 Hz with about 8.9 % dead time.

FADC System

The FADC system[25] was comprised of 21 FADC modules, two data compressor modules and two crate controllers (FADC-CC), for read-out of the JET and IDC data.

On receiving a first level trigger, the FADC-CC starts distributing clock signals through a back-plane of the crate and initiates digitization and zero suppression of the FADC modules. After generating 512 clock signals, a "conversion end" is issued by the FADC-CC, which then enables a scanning process of the compressor. The compressor scans all the data stored in the FADC modules channel by channel. It compresses the data size and the compressed data are stored in a FIFO memory.

In addition to the normal event processing described above, the FADC-CC has several auxiliary functions for debugging and monitoring. Here one of the most essential functions is described shortly. The zero suppression of FADC system reduces the data size significantly, but it requires to monitor the baseline of FADC outputs which slightly drift during a flight. In order to set the zero suppression threshold to an optimum value throughout an experiment, the baseline monitoring and threshold adjustment run which is called "calibration run" is performed every one hour. It takes approximately 100 seconds for one "calibration run".

CAMAC System

A variety of CAMAC modules were housed in two CAMAC crates for readout of TOF data, the implementation of trigger system, and counting trigger statistics and hitting statistics of various counters. An intelligent CAMAC crate controller (ICCC)[31] has been developed specially for this experiment. The ICCC is equipped with three Transputer in it and can be naturally embedded in a Transputer network. In the CAMAC crate which contains the master trigger module (MT), the ICCCs receives a trigger signal directly from the MT. Then two ICCC's start gathering data from CAMAC modules in parallel, and send them to the EVB through the Transputer links.

Event Builder

The EVB is composed of four input ports, one DMA controller, and three output ports. Data from FADC compressors and the CAMAC-CCs are gathered by the input ports, the DMA controller merges them into formatted event-data and the event-data is transmitted to the Transputer bank through one of the output ports. These tasks are processed in parallel; If the input ports receive T0 trigger, they starts gathering data from FADC compressors and CAMAC-CCs. When the fast clear signal is received, the gathering process is terminated and the input ports are cleared to accept next T0 trigger. After all data are transfered into one of two buffers, the DMA controller starts merging and formatting these data into a event-data. and at the same time the trigger lock is released. If the next T0 trigger is received, the FADC and CAMAC data of the next event can be transfered into another buffer so as to reduce readout dead-time. The event-data is transmitted through one of three output ports into the Transputer bank. Another two output ports can transmit the next event-data. Thus the EVB may process a series of different five events concurrently. The processing speed of the EVB is about 24Mbytes/s, i.e., the EVB can accept the trigger rate of up to 12 kHz for typical data size of 2 kbytes.

Transputer Bank

The main role of the Transputer bank is to select desirable events using the whole detector information: (1) Trigger mode, (2) TOF hits, and (3) rigidity of JET tracks reconstructed using FADC data.

For JET track reconstruction and rigidity calculation, the following algorithm is employed:

1. Determine hit position, total amount of charge, and pulse width using FADC data. Since the charge information in FADC data is the sum of pedestal and charge of the hit, the pedestal is subtracted for each hit.

The pedestal value of each FADC channel is automatically updated at every 1 hour of the calibration run.

2. Select "good" hits which are defined as hits enough charge and width.
3. Find arrays by connecting the "good" hits in central region of JET chamber, and perform line fitting.
4. Extrapolate each of the line trajectories to find "good" hits near the trajectory, and associate the hits to the array.
5. Perform circular fitting on the array and the associated hits. The circular fitting algorithm is based on non-iterative method by following Karimaki [32].
6. Scan all of "good" hits in JET chamber to check whether they are close enough to the circular trajectory or not. Only the hits passing this check are used in the following process.
7. Perform circular fitting once more and calculate the transversed rigidity in $r\phi-$plane.

Fifteen Transputers arranged in a 3×5 matrix are dedicated to this job in the Transputer bank. They execute the same program to process events simultaneously. One of the first three Transputers receives the formatted event-data from the EVB through a Transputer link. Then the Transputer processes the event-data, or otherwise if it is already busy, the event-data is relayed down to the following Transputers. Consequently, the Transputer bank can process fifteen events concurrently. If all the Transputers are occupied and busy, the EVB stops sending event-data to the Transputer bank.

Each Transputer executes the above task typically within 20 ms. Therefore, the whole bank including fifteen Transputers is capable of processing events at 1 kHz. The accepted event-data are relayed down and are finally sent to the data-storage subsystem via a Transputer link.

2.7.2 Monitor Subsystem

The monitor subsystem handles the monitor-data which are sent from various sensors distributed in the payload for the house-keeping purpose. The transducers generate voltage outputs according to the measured values of temperature, pressure and alttitude of the payload. In the flight we monitored temperatures, pressures, a magnet status, a chamber high voltage status, high voltage status of TOF and Cherenkov counter's PMTs and the GPS receiver and clinometers. The data are transmitted to the ground station and are utilized to monitor and check the detector statuses during a flight.

They are also transferred to the data-storage subsystem to be recorded for the off-line analysis.

2.7.3 Communication Subsystem

The communication subsystem manages communication between the payload and the ground station. A serial radio link is used for the transmission media. As a transceiver terminal of the radio link, Consolidated Instrument Package (CIP) is provided and attached to the payload by the National Scientific Balloon Facility (NSBF). The ground station sends commands to the payload through the radio link, and the CIP receives and interprets the commands as a 16-bit data. The control subsystem fetches the data from the CIP, and dispatches them to the other subsystem. And inversely, responses to the commands, message-data generated constantly by all subsystems, monitor-data for the house-keeping, and event-data sampled at two-second intervals are sent via the control subsystem to the CIP. Then the CIP sends them to the ground station through the radio link. Communication history is also recorded by the data-storage subsystem for off-line analysis.

2.7.4 Data-Storage Subsystem

The data-storage subsystem receives the event-data from the event-process subsystem via a Transputer-PCI interface card. The data-storage subsystem controller handles the SCSI III bus interface and record the communication-, monitor-, and event-data from the other subsystems are recorded into an EXABYTE 8-mm magnetic tape.

The data storage capacity of an 8-mm tape is 60 Gbytes and is not large enough to record all the data collected during a one-day flight. Therefore two tape drives were employed and the data recording was switched from one drive to the other serially after running through the first tape. The tape drives were housed in an iron steel box located outside the pressure vessel for the magnetic shield.

2.8 Power Distribution System

2.8.1 Regulators

Most of the electronic circuits were implemented in custom made modules, which were housed in several crates. The power from the battery bank was directly fed to the power bus lines of the dedicated crates. The output voltage of the battery droops as time elapses. Every module of electronics was equipped with commercially available low-dropout voltage series regulators.

The DC-DC converters were not used from the noise consideration except for high voltage supplies.

The Transputer bank consists of several commercial VME modules and their total load current exceeds 10 A. The distributed regulator configuration could not be applied to this subsystem. Therefore a 5 V high current (30 A) series regulator with low dropout voltage (500 mV) has been developed to cope with requirement.

2.8.2 Control

A flexible and reliable power switch system is important to conduct the whole balloon experiment. Some of the power lines must be switched on/off simultaneously to assure proper operation of the system. Unbalanced voltage supplies might cause damage to the circuits. In addition, only a part of the apparatus is sometimes desired to be powered. In the pre-flight test with batteries, for example, the power consuming subsystem should be switched off after a short checkout to save the battery power while the detector status are to be continuously monitored. The power control system is to switch on/off the individual battery groups by commands transmitted through radio link.

The BESS power control system has been developed on the platform of Echelon LonWorks a technology that facilitates developments of distributed, intelligent control networks. A LonWorks network consists of a series of nodes, each of which is implemented with Neuron integrated circuits[33] communicating with one another through a message-based protocol called LonTalk[34]. Receiving a command, the neuron interprets the command and initiates a sequence of operations accordingly. The power control system consists of five relay nodes and a command node distributed along the local network. The command node functions as a controller of the relay nodes and issues messages to designated relay nodes, according to the commands addressed to the power control system. In the relay node the neuron, with its 11 I/O pins, is interfaced with 11 PhotoMOS relays[35]. The load currents of the power supplies varies from less than 1 A to about 50 A among the subsystems. Some of the PhotoMOS relays, which can switch a current up to 4 amperes, directly switch on/off the power supplies with lower load currents. For the higher current loads, the PhotoMOS relays indirectly switch the power through driving solid state relays equipped with N-channel power FETs. The solid state relays are connected in parallel according to the load currents so that the voltage drops at the relays can be kept within a few tens mV.

The control system was duplicated for reliability. The power should be kept during the flight even in the case of accidental hardware failure or command loss due to bad radio link. Two relay nodes were connected in parallel and they were controlled by different sets of commands. The power was turned off only when the both switches were off.

Chapter 3

Ground Observation

3.1 Experimental sites

A ground observation was carried out on September 4, 2001 at Ft.Sumner, New Mexico, U.S.A. (see Figure 3.2 [39]) during a standby for a balloon flight($\sim$ 36 km above sea level). The altitude of the experimental site is 1270 m above sea level and its latitude and longitude are $34°29.34N$ and 104°13.17W, respectively. The average atmospheric depth during a 4-hour data taking was 892 g/cm^2. Figure 3.1 [38] shows the geographical distribution of the vertical cut-off rigidity for the primary cosmic rays entering the earth. The vertical cut-off rigidity at Ft.Sumner is 4.2 GV.

3.2 Experimental Surroundings

The observation was performed in September 4, 2001. The atomospheric pressure and temperature during the observation are shown in Figure 3.3. However temperature represents a room temperature in the hangar. During the observation, mean atomospheric pressure was 892 g/cm^2.

3.3 The Observations

The trigger rate, i.e., the rate of the coincidence of upper and lower TOF signals (T0 trigger) was about 35 Hz. A pedestal run of 100 seconds was carried out every hour to re-adjust the thresholds for FADC data suppression as low as possible, because the pedestal value of FADC outputs varied depending on temperature. During the whole observation time of about 4 hours, 399427 events were collected. We named the obtained data set as "run", and put the number to indicate when it was observed. Table 3.1 summarizes the status, DAQ time, live time, dead time fraction, and the number of observed events in each run.

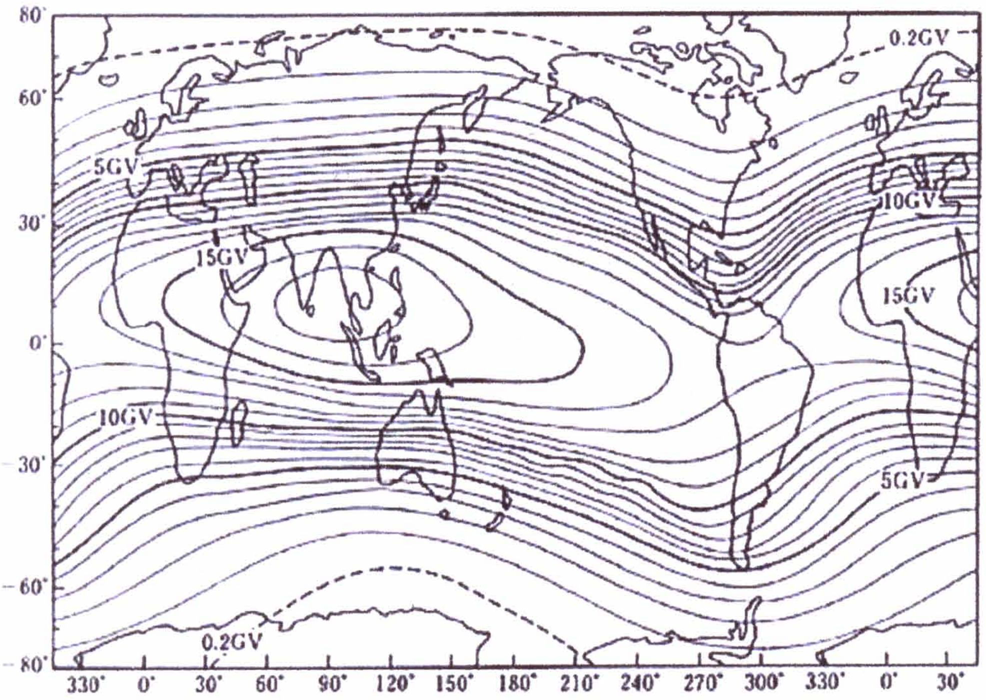

Figure 3.1: The geographical distribution of the vertical cut-off rigidity in order that primary cosmic rays enter the earth [38].

Table 3.1: Summary of four runs of the BESS-2001 ground experiment

Run #	Local time		Pressure (g/cm^2)		DAQ time (sec)	Live time (sec)	Dead time (%)	Recorded events
	start	stop	min	max				
95	14:39:17	15:22:23	891.9	892.8	2508.12	2488.25	0.80	86478
96	15:38:36	16:16:12	891.5	892.2	2180.67	2163.28	0.80	75115
97	16:25:50	17:25:44	891.4	892.2	3516.69	3488.75	0.80	120592
98	17:27:05	18:25:25	892.0	892.8	3425.31	3398.12	0.80	117242

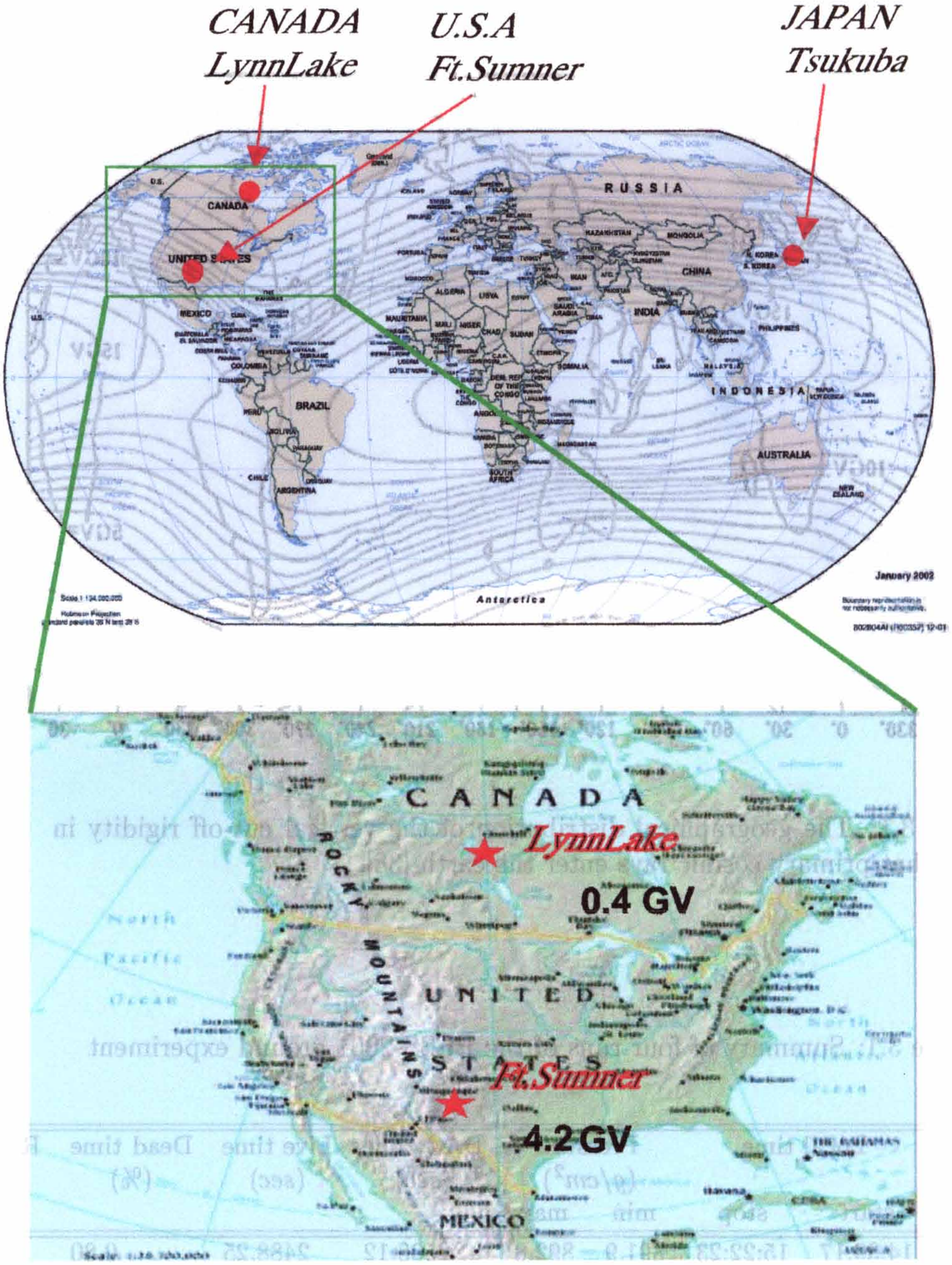

Figure 3.2: Ground experimental sites of previous and in 2001 [39].

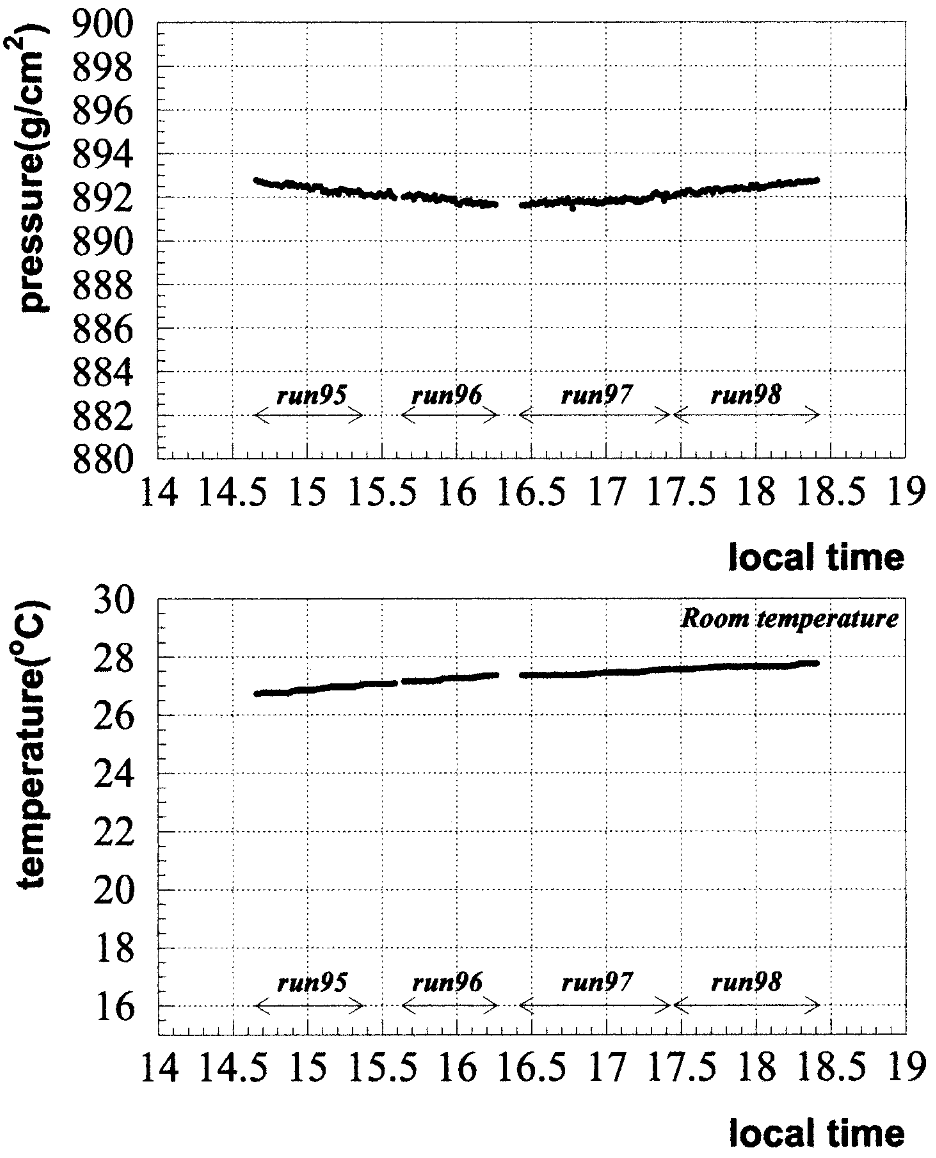

Figure 3.3: The atmospheric pressure and temperature at Ft.Sumner, September 4, 2001. However temperature represents a room temperature in the hangar.

Chapter 4

Data Analysis

In this chapter, we describe the data analysis for positive and negative muon flux. First, we select negative muon events and check the detector performance. After estimating the background contamination, we obtain positive and negative muon flux.

4.1 Event Selection

Selection of muons is divided into two steps, "pre-selection" and "particle identification". The pre-selection selects "Single track" i.e., particles which passed through the detector without any interactions, and with "fiducial volume". Particle indentification is performed by dE/dX selection and mass determination.

In order to calculated the absolute fluxes of muons, we need to know the kinetic energy of the particle at the top of instrument(TOI), detection efficiency, and background contamination. Therefore, it is inevitably important to select mass-identified events without interaction inside the detector.

4.1.1 Pre-Selection

In this analysis, we used events triggered by the following triggering conditions. The condition was unbiased T0-CD trigger which required only a coincidence between the upper and lower TOF scintillation counters. Therefore, the data contained events in which more than one particle passed through JET chamber at the same time. These events seem to be generated by showers in the atmosphere above the instrument or in the upper part of the instrument itself.

At the first stage of the event selection, following cuts are applied to select single track events which are fully contained in the fiducial region.

- **Single Track Selection**

- N_{TOFU}=1 or 2, N_{TOFL}=1 or 2

  There should be one or two hits in each upper and lower TOF hodoscopes. When a particle passes through very close to the edge of counter, it may hit two adjacent counters.

- N_{longTK}=1

  The number of isolated long tracks inside tracking detector should be only one. The "long track" is defined as following:
  (1)We search for arrays of 10 or more hits in JET chamber.
  (2)For each arrays the number of JET hits expected from the trajectry(N_{expect}) is calculated.
  (3)Array with enough hits($> 0.6 \times N_{expect}$) is regarded as a " long track".

  Even if accidental particles which were unrelated with the trigger passed through the instruments, their tracks were not counted in N_{longTK}.

- **Fiducial Volume Cut**

  - $N_{expect} \geq 16$

    N_{expect} is the number of hits inside the JET chamber expected from the trajectory. JET chamber is divided into four columns by three cathode planes. Each column is further divided by an anode plane into two columns. Central six columns out of eight were used for fiducial region. This cut defines the fiducial region in the $r-\phi$ plane to eliminate the track which scratches the outer almost region, where the position measurement is less accurate then the central region due to the distortion of the electric field.

  - (1) -475$\leq Z_{trackU} \leq$ 455, -475$\leq Z_{trackL} \leq$ 455 (whole region)
    (2) -475$\leq Z_{trackU} \leq$ 455, -223$\leq Z_{trackL} \leq$ -38 (with lead region)
    (3) -475$\leq Z_{trackU} \leq$ 455, -475$\leq Z_{trackL} \leq$ -243,
    -18$\leq Z_{trackL} \leq$ 455 (without lead region)

    By extrapolating the track trajectory found in the JET chamber, the expected hit positions at the upper and the lower TOF counters are calculated. This cut defines the fiducial region in the y-z

plane, and ensure a particle should pass through the TOF scintilators area.
(1)whole region:
Muon candidates were selected from events pass through the whole region.
(2)with lead region:
Detection efficiency for events which passed through the lead plate are defferent from that for events which did not pass through the lead. The fiducial volume without lead are three times as large as the volume with lead. In order to estimated electron contamination, we used the fiducial volume with lead plate.
(3)without lead region:
In order to estimate proton events, we used the fiducial volume without lead region for the clearer events selection.

  - TOF hit counters should be consistent with the rϕ trajectory.

    In the $r\phi$-plane the extrapolated trajectory ahould pass through the upper and the lower hit TOF counter. This condition ensures that the track information and the TOF information are concerned with the same particle.

  - $\cos\theta_{zenith} \geq 0.9$ ($\theta_{zenith} \leq 25.8°$)

    In order to obtain nearly vertical fluxes, we required that cosine of zenith angle, $\cos\theta_{zenith}$, is larger than 0.9.

- **Others**

  - Albedo particle rejection($\beta > 0$)

    We selected downward-going particles. Albedo particles are elininated by using the time of flight since we intend to derive the muon fluxes at the top of the instrument.

Further analysis of particle identification was applied to the events which passed the above pre-selection.
The "Pre-selection" criteria are summarized in Table 4.1.

Table 4.1: Summary of the event-selection criteria.

Pre-selection	
Single track	
1. Hits in TOF	$N_{TOFU} = 1 or 2$, $N_{TOFL} = 1 or 2$
2. Number of long track	$N_{longTK} = 1$
Fiducial volume	
3. Expected hits in JET	$N_{expect} \geq 16$
4. z hit-position in TOF(whole region)	-475$\leq Z_{trackU} \leq$ 455, -475$\leq Z_{trackL} \leq$ 455
5. z hit-position in TOF(with lead region)	-475$\leq Z_{trackU} \leq$ 455, -223$\leq Z_{trackL} \leq$ -38
6. z hit-position in TOF(without lead region)	-475$\leq Z_{trackU} \leq$ 455, -475$\leq Z_{trackL} \leq$ -243, -18$\leq Z_{trackL} \leq$ 455
7. Zenith angle	$\cos\theta_{zenith} \geq 0.9$
others	
8. Albedo particle rejection	$\beta > 0$

4.2 Muon Identification

We applied lower TOF dE/dX band cut and $1/\beta$ band cut to identify muons. As mentioned in Section 4.1.1, we used the fiducial volume with lead plate to estimate electron contamination, and used the volume without lead plate to estimate proton contamination.

4.2.1 dE/dX Cut

We selected "Single charged particles" and reject electron events. Figure 4.1 shows dE/dX vs momentum plots of the upper TOF scintillators for events. Almost single charged particles are shown in Figure 4.1. Thus, upper dE/dX band cut region was applyed as loose as possible not to reject muon candidates. Figure 4.2 shows dE/dX vs momentum plots of the lower TOF scintillators with lead region for events. Electrons are shown negligibly in Figure 4.2, almost minimum ionizing particles(MIPs) are distributed. Since lower TOF dE/dX-band cut region was also applyed as loose as possible. Atmospheric cosmic-ray particles on the ground are almost single charged particles. The boundary region of the upper and the lower dE/dX cut was applyed from 0.5 to 3.5 MIPs between red lines in figure.

As shown in Figure 4.3, rigidity vs beta inverse were distributed consistently before and after dE/dX-band cut.

4.2.2 $1/\beta$ Cut

Particle mass is related to rigidity R, β and charge Z as;

$$M^2 = R^2 Z^2 \left(\frac{1}{\beta_{mes}^2} - 1 \right). \tag{4.1}$$

Since we already selected single charged particles($|Z| = 1$) with "dE/dX band cut", we can identify muon events by using rigidity and β. The band width of $1/\beta$ band cut was set to 3.89 σ to reject proton events. Figure 4.4 shows the boundaries of this "muon $1/\beta$ band cut" applied to the events survived the pre-selection, quality cut, and dE/dX band cut. Because $1/\beta$ distribution were described well by Gaussian as shown in Figure 4.5 and half-width of the $1/\beta$ selection band was set at 3.89 σ, the efficiency is very close to unity(99.99% for pure Gaussin).

As shown in Figure 4.5, $\Delta 1/\beta (\equiv 1/\beta - 1/\beta_{mes})$ distributions for various rigidities are fitted well by the Gaussian function. β is calculated by using the following formula;

$$1/\beta = \sqrt{\left(\frac{M_\mu}{R}\right)^2 + 1}, \tag{4.2}$$

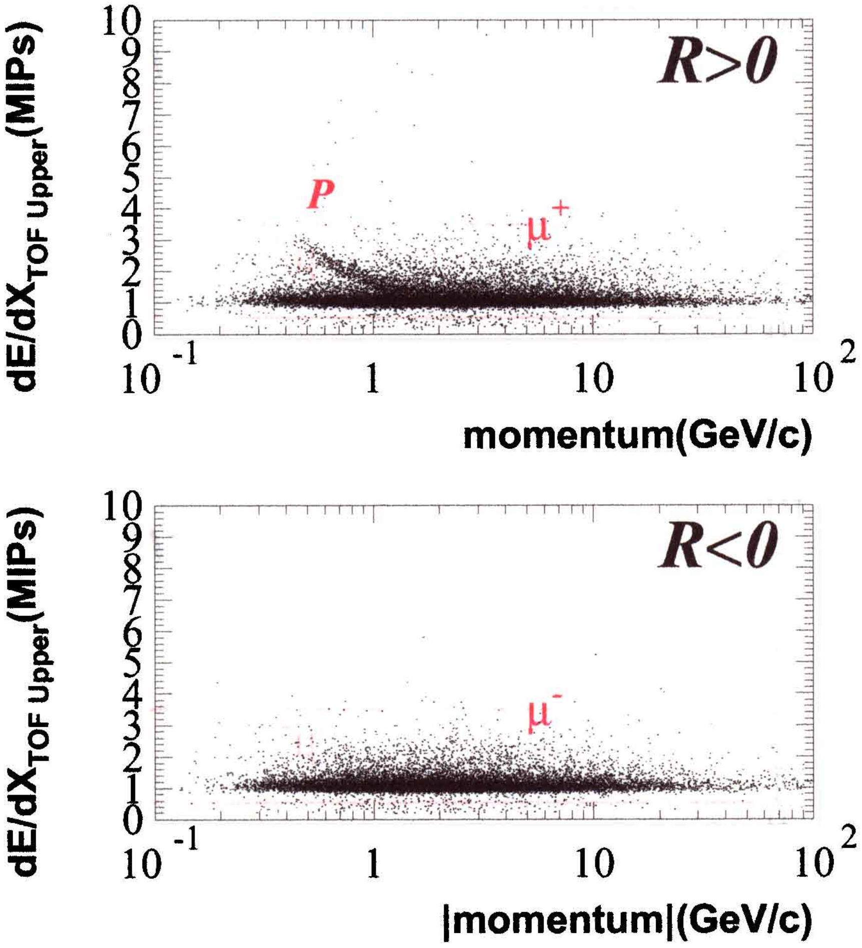

Figure 4.1: dE/dX cut for the upper TOF scintillation counters (whole region)

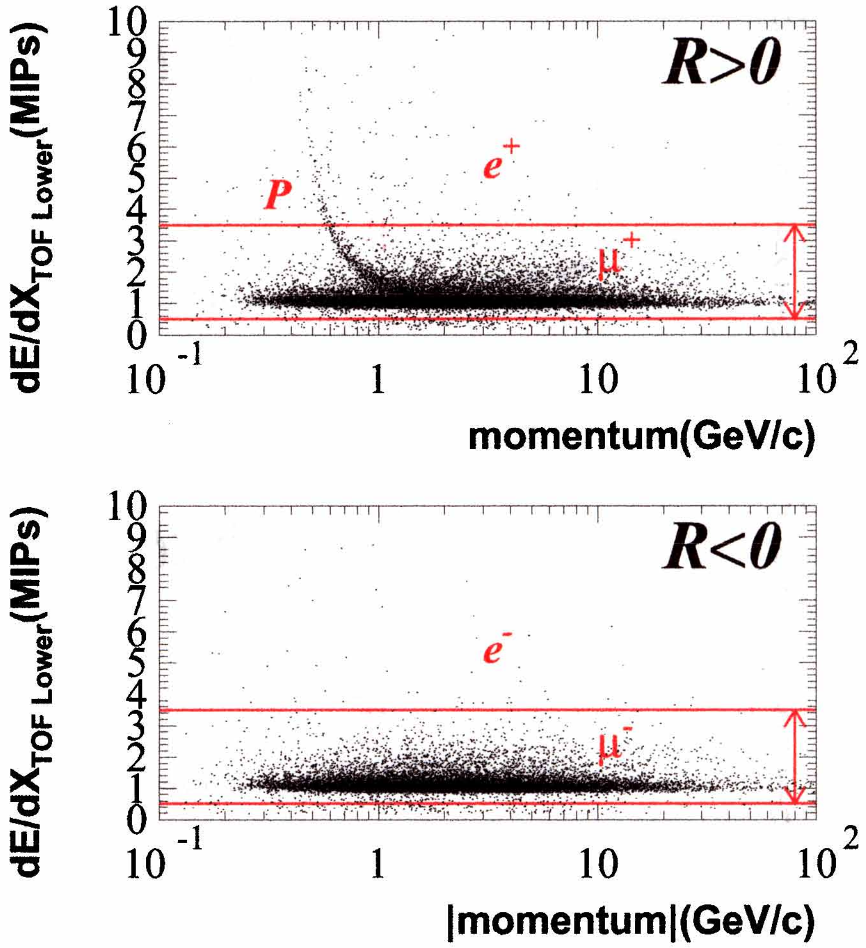

Figure 4.2: dE/dX cut for the lower TOF scintillation counters (with Pb region)

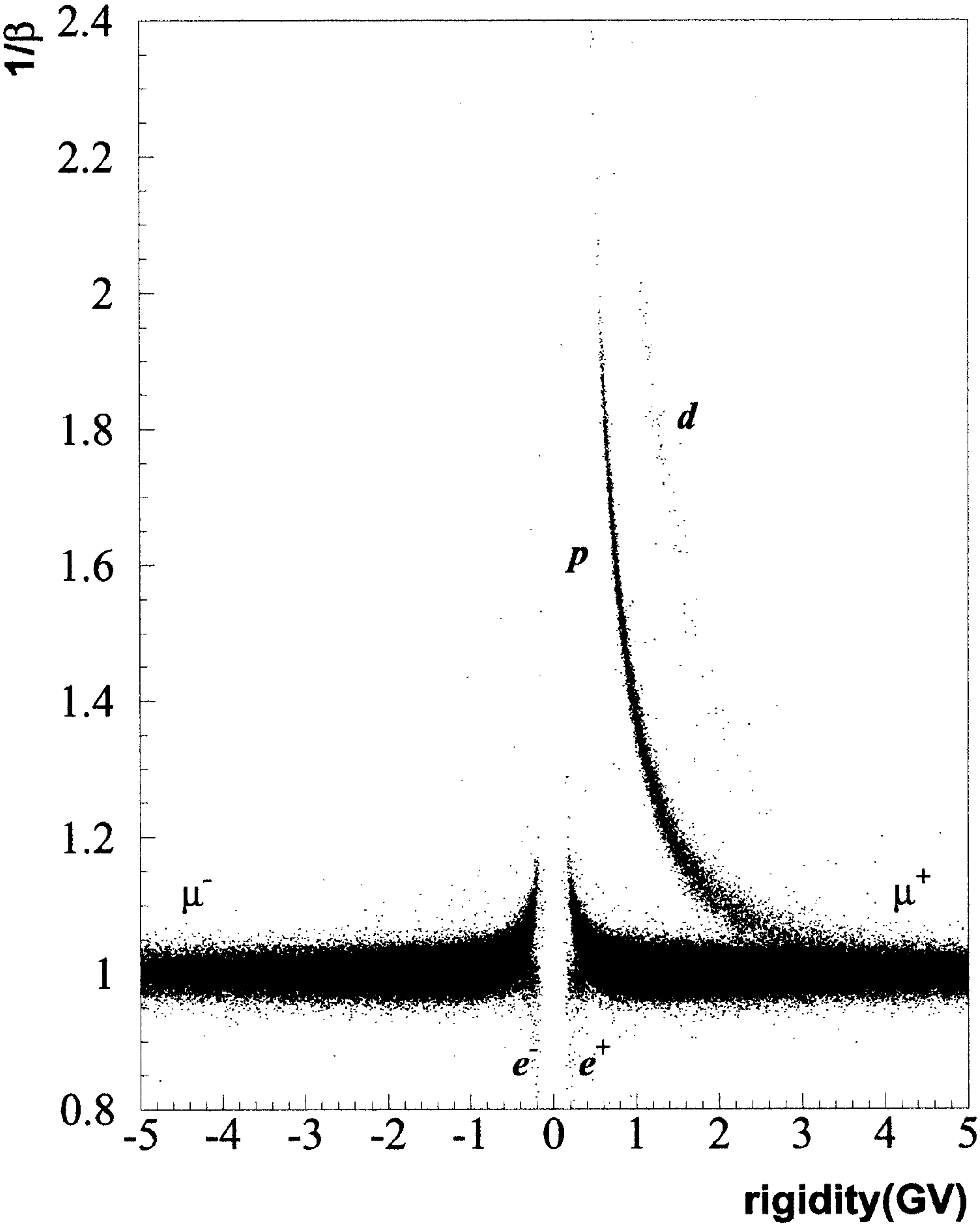

Figure 4.3: $1/\beta$ vs rigidity plot after "dE/dX-band Cut"

where M_μ denotes the muon mass. The central values of the $\Delta 1/\beta$ distributions were zero as shown in the Figure 4.5.

Figure 4.6 shows the $1/\beta$ resolution($\sigma_{1/\beta}$) as a function of rigidity, where $\sigma_{1/\beta}$ denotes the mean square values of the $\Delta 1/\beta$ distribution.

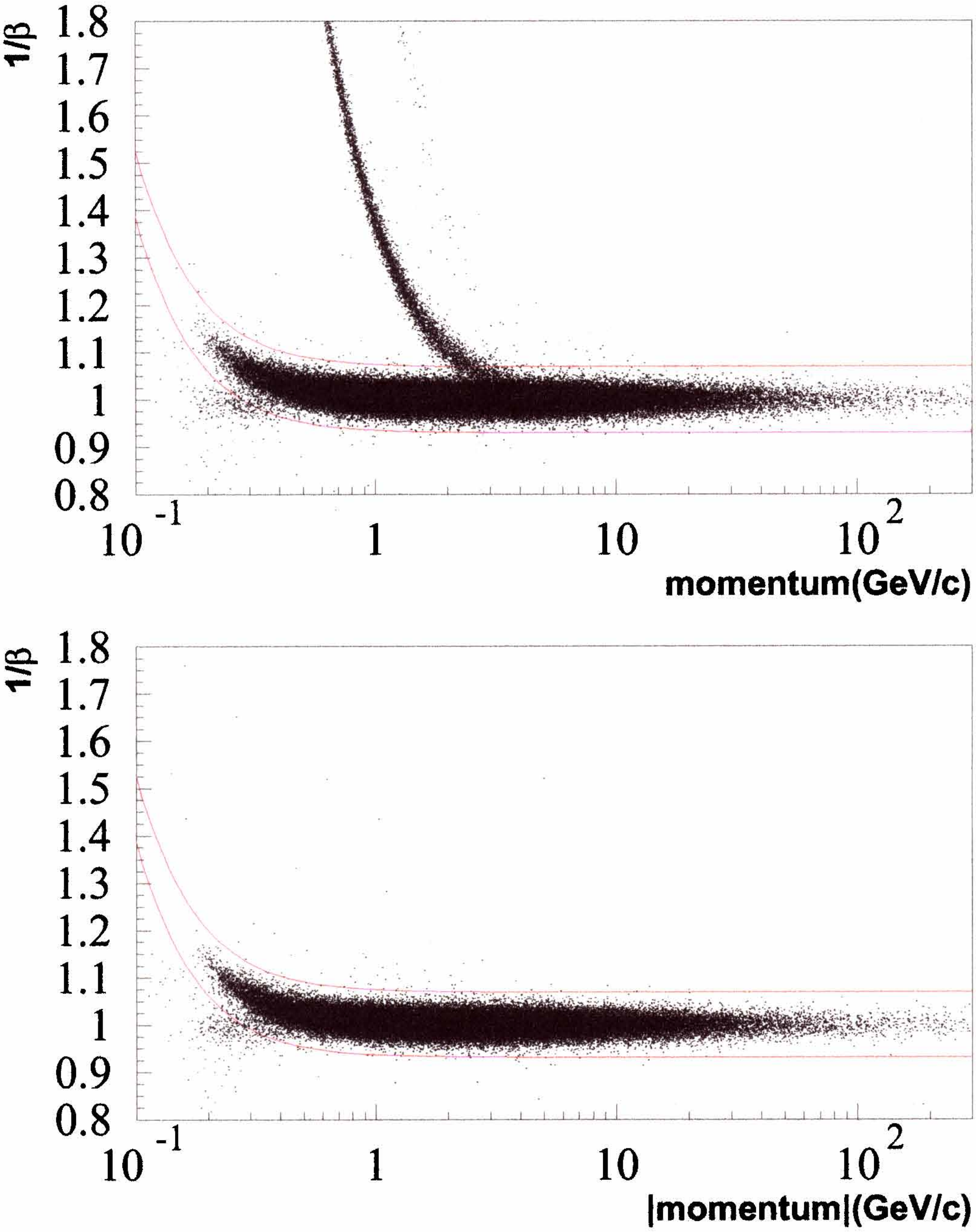

Figure 4.4: $1/\beta$ vs rigidity plot after "dE/dX-band Cut". (Top) Positive momentum range. (Bottom) Negative momentum range.

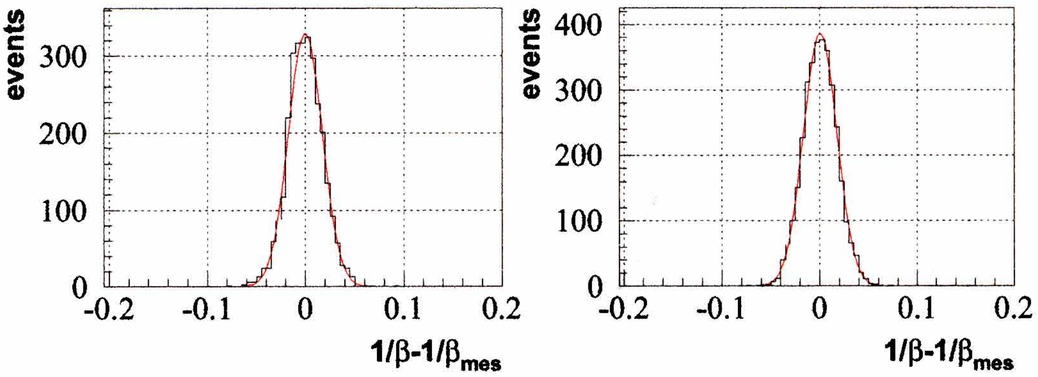

0.6<Rigidity<0.7 *0.7<Rigidity<0.8*

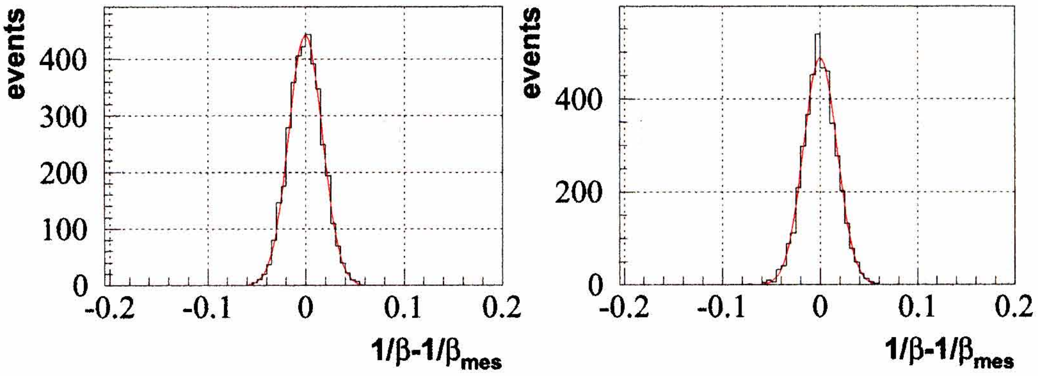

0.8<Rigidity<0.9 *0.9<Rigidity<1.0*

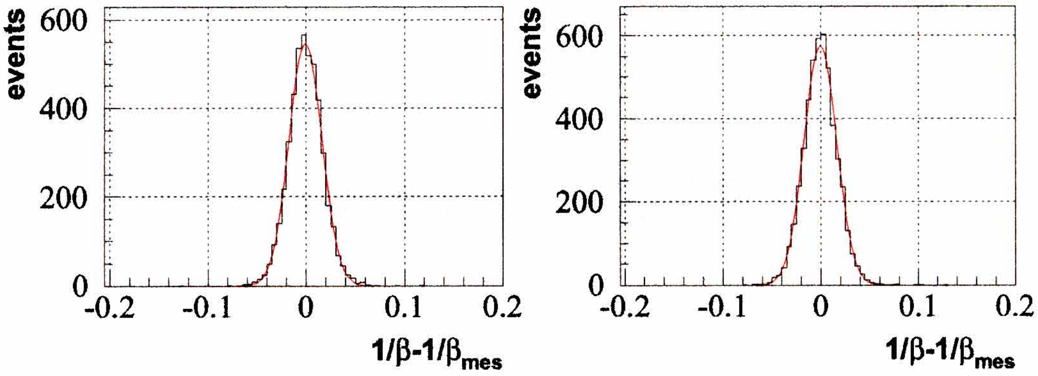

1.0<Rigidity<1.2 *1.2<Rigidity<1.4*

Figure 4.5: $1/\beta$ distribution for muon events with various rigidities. The red curves represent the Gaussian fits.

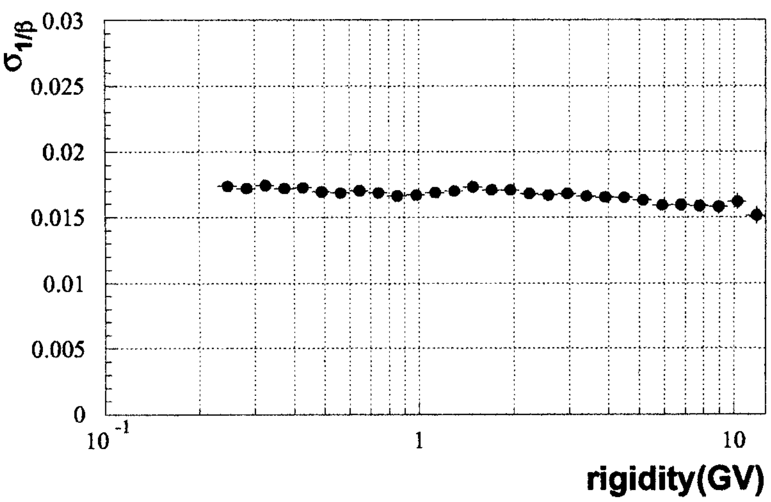

Figure 4.6: Resolution of $1/\beta$ distribution as a function of rigidity.

4.3 Detector Performance

We checked the detector performance using the samples of muons selected in Section 4.1.

4.3.1 Rigidity measurement

The uncertainties of the rigidity measurement is estimated in the $r\phi$-fitting process.

To determine the total rigidity, R, we obtain a dip angle, θ_{dip}, which is defined as an angle between the total rigidity vector and r-ϕ plane in Figure 4.7. The total rigidity R are derived from R_t and θ_{dip} as $R = R_t/\cos\theta_{dip}$.

Figure 4.8 shows the estimated errors of the $1/R_t$, where R_t denotes the transverse rigidity projected onto the $r\phi$ plane. The opened histogram is for all the muons samples selected in section 4.1($N_{expect} \geq 16$). The hatched and the cross hatched histogram is for the events with long trajectory, $N_{expect} \geq 20$ and $N_{expect} \geq 24$, respectively. These histograms have a clear peak around $\Delta(1/R_t) \sim 0.004$, which represents maximum detectable rigidity(MDR) $\sim$ 250GV.

Figure 4.9 shows rigidity resolution $\Delta(1/R_t)$ as a function of rigidity.

4.3.2 dE/dX measurement

We have discussed already shown in section 4.2

4.3.3 β measurement

We have discussed already shown in section 4.2

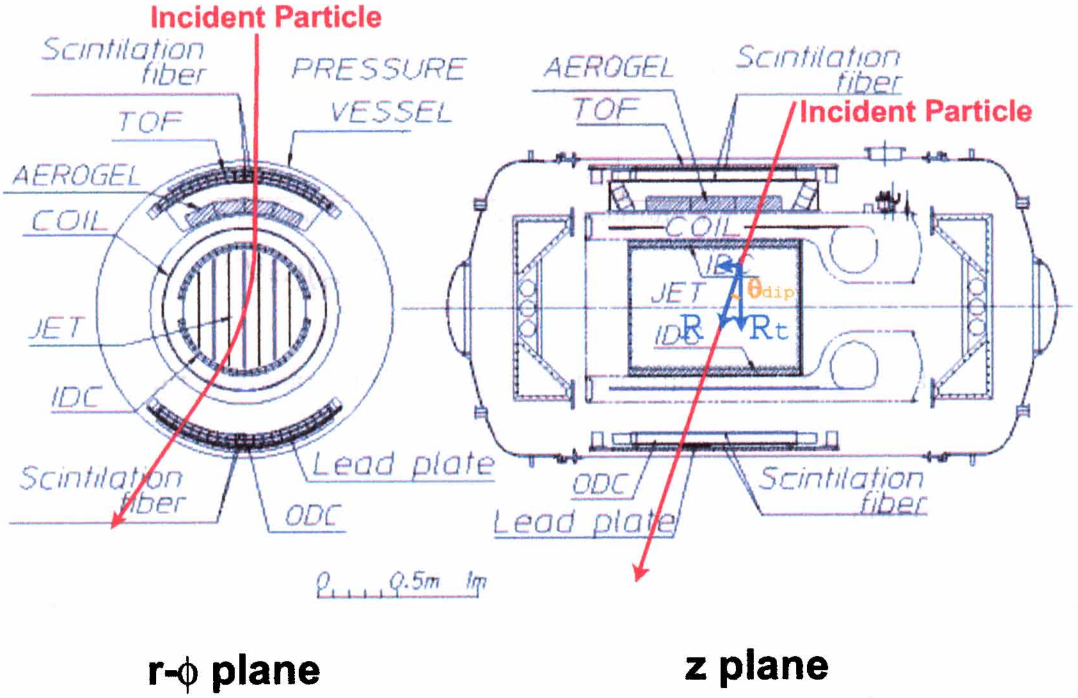

Figure 4.7: Definition of coordinate. (Left) r-ϕ plane. (Right) z plane.

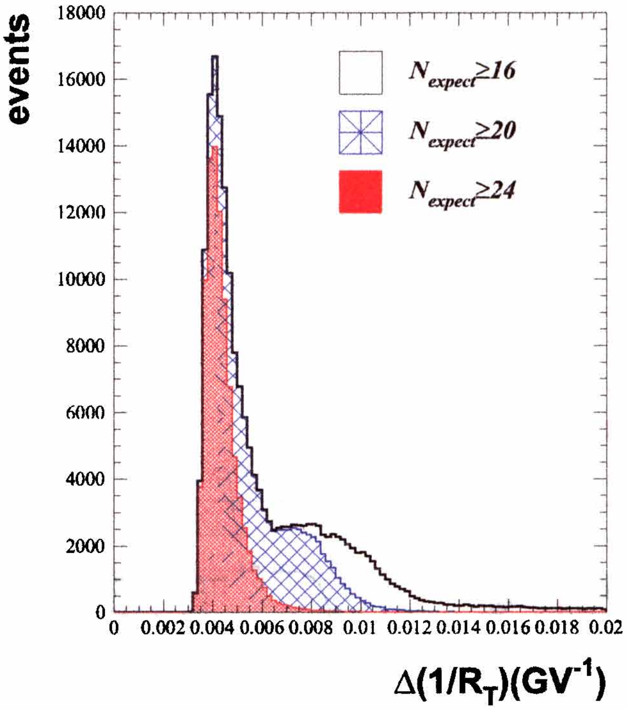

Figure 4.8: Distributions of error in inverse of transverse rigidity.

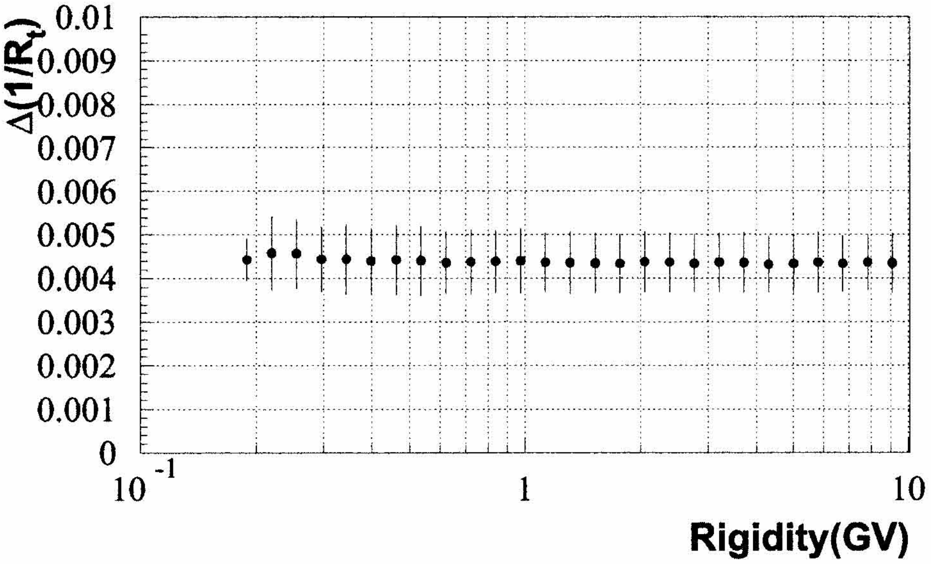

Figure 4.9: Rigidity dependence of $\Delta(1/R_t)$.

4.4 Normalization and Corrections

In conformity with previous experiments, muon spectrum is shown as a function of momentum. From the number of observed candidates(N_{obs}) obtained in Section 4.1, the differential flux of muon at the top of the instrument (F_{TOI}) is calculated as follows:

$$F_{\mathrm{TOI}} = \frac{(N_{\mathrm{obs}} - N_{\mathrm{BG}})/\varepsilon}{S\Omega \cdot T_{\mathrm{live}} \cdot \mathrm{d}P}, \tag{4.3}$$

where

N_{obs} : Number of observed candidates,

N_{BG} : Number of expected background contamination,

ε : Detection efficiency of each particle,

$S\Omega$: Geometrical acceptance,

T_{live} : The total live time,

In this chapter, we discuss about estimations of each factor in Equation 4.3.

4.4.1 Ionization energy loss in the detector

Incoming particles measured in the JET chamber lose a certain fraction of energy while they traverse materials in an upper half part of the detector. After traversing the material of x g/cm^2, the energy of particle $E(x)$ is reduced to be as:

$$E(x) = E(0) - \int_0^x \frac{dE}{dx}(E,x)dx,$$

where $E(0)$ is particle energy at the top of the instrument. The actual thickness of the material for a particle to traverse depends on the particle trajectory. The energy loss was calculated for each event by summing up the energy losses at every steps in the detector components.

4.4.2 Exposure Factor

The exposure factor consists of geometrical acceptance ($S\Omega$) and live time (T_{live}), and is given by

$$Exposure\ Factor = S\Omega \cdot T_{\mathrm{live}}. \tag{4.4}$$

- Geometrical Acceptance($S\Omega$)

  The geometrical acceptance is defined by the simple geometry of the acceptance of an incoming particle. It can be calculated reliably by a Monte Carlo simulation based on GEANT [40], in the following way [41]:

  1. Define a sphere (A) of radius R_A which include the whole instrument.
  2. The geometrical acceptance of A for isotropic down-going flux can be easily calculated as:

     $$S\Omega_A = \frac{1}{2}4\pi \cdot \pi R_A^2 = 2\pi^2 R_A^2,$$

     because the sphere with a radius of R_A has a projection area of πR_A^2 from any angle of observation. The factor of 1/2 multiplied to 4π corresponds to down-going incidence of observed flux.
  3. Using the incident particles from A, we trace the particles through the instrument with GEANT with a solenoidal magnetic field of 1 Tesla by switching off both the interaction and energy losses.
  4. We applied the same fiducial volume cut to the Monte Carlo events, as the fiducial volume cut in the pre-selection described in Section 4.1.1. The ratio (r_{fiducial}) is obtained as the fraction of survived events to the generated events.
  5. The geometrical acceptance of the detector ($S\Omega$) is calculated from $S\Omega_A$ and r_{fiducial} as:

     $$S\Omega = S\Omega_A \cdot r_{\text{fiducial}}.$$

  Figure 4.10 shows the geometrical acceptance SΩ for muons.

- Live Time (T_{live})

  The live time of observation was directly measured by 1 MHz-clock pulse generator and scalers. The resultant live times are summarized in Table 3.1.

4.4.3 Detection Efficiencies

The detection efficiency is defined as

$$\epsilon = \frac{N_{observe}}{N_{incident}},$$

Figure 4.10: The geometrical acceptance SΩ for muons with a given momentum.

where $N_{incident}$ is the number of incident particles within the acceptance of the detector, and $N_{observe}$ is the number of identified particles. The detection efficiency is decomposed into some factors:

$$\epsilon = \epsilon_{single} \cdot \epsilon_{reconst} \cdot \epsilon_{1/\beta} \cdot \epsilon_{dE/dX} \cdot (1 - \epsilon_{accident}),$$

ϵ_{single} : Single track efficiency

$\epsilon_{reconst}$: Track reconstruction efficiency

$\epsilon_{1/\beta}$: $1/\beta$ cut efficiency

$\epsilon_{dE/dX}$: dE/dX cut efficiency

$\epsilon_{accident}$: Accidental hits efficiency

(1) Single Track Efficiency (ϵ_{single})

Only the cosmic-ray particle recognized as a single track undergoes further analysis. The definition of the "single track" is described in the section 4.1.1. This "Single Track Selection" efficiency is determined mainly by 'N_{TOFU}=1 or 2','N_{TOFL}=1 or 2'. Nuclear interaction length is about 100 g/cm^2 for

Table 4.2: Table of correction factors and calculation methods of those factors for μ^+ and μ^-

Correction Factor	μ^+	μ^-
Energy loss	calculate for each events	calculate for each events
Track reconstruction ϵ	scan 1008 events	use same value as μ^+
Single track selection ϵ	use GEANT simulation	use GEANT simulation
Exposure factor SΩ	use GEANT simulation	use GEANT simulation
Event selection efficiency **(1)dE/dX cut ϵ** **(2)1/β band cut ϵ**	use real μ^+ data	use real μ^- data
background	use real proton and electron data	real positron data

BESS detector's materials (aluminum, plastics, and so on). Since muons have no strong interactions, they penetrate easily detector.

To estimate energy dependent efficiency, we need to rely on the Monte Carlo simulations in the following way. We generate a simulation as below;

1. We define a half sphere with radius R above the instrument, and through it generate a uniform flux of muons with the initial energy E_{TOI} and the incident angle ω_{TOI}.

2. We trace the muons through the instrument with GEANT, taking into account the actual geometry, all materials inside the detectors including support frames, 1 Tesla uniform magnetic field in the solenoidal magnet. We take into account all interactions such as multiple scattering, energy loss, knock-on electrons, hadronic interactions and annihilation.

Finally, ϵ_{single} is given by

$$\epsilon_{single} = \frac{A \bigcap B}{A},$$

where A is the number of events passing through "fiducial volume", B is the number of events under the condition of "single track".

The momentum dependent single track efficiency is shown in Figure 4.11.

(2) Track Reconstruction Efficiency ($\epsilon_{reconst}$)

Since JET chamber and IDC's have insensitive region very close to sense wires due to the dead time of FADC, reconstruction of the trajectory could

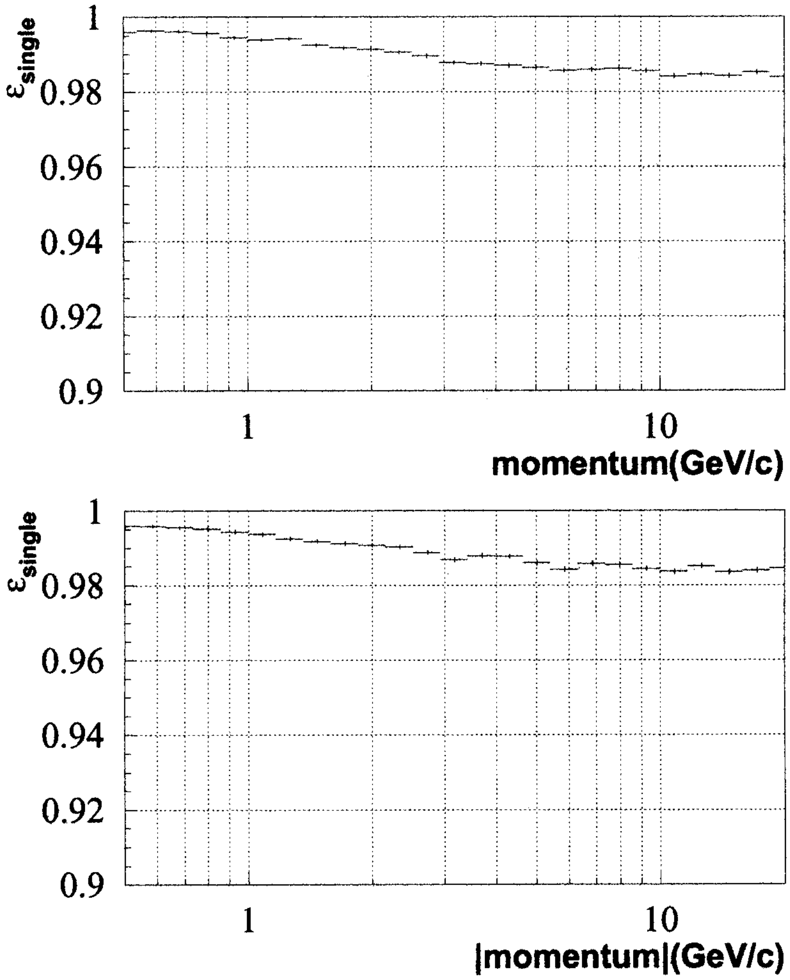

Figure 4.11: Single track efficiency for muons. (top)positive muon, and (bottom)negative muon.

be made failure even if there are hit points of enough in chambers. In these events no trajectory is found(i.e., N_{track}=0) even if enough hits were left in JET chamber and IDC's. In order to estimate the track reconstruction efficiency($\epsilon_{reconst}$), we scanned 1008 unbiased events with appropriate TOF hits and enough JET, among which the failures of reconstruction were found only in 5 events. As a result, we estimate

$$\epsilon_{reconst} = 99.5 \pm 0.1\%.$$

(3) $1/\beta$ cut efficiency ($\epsilon_{1/\beta}$)

The band width of $1/\beta$-band cut was set within 3.89 σ which covers 99.99 % integral area for a Gauss function. Figure 4.4 shows the boundaries of this "muon $1/\beta$-band cut" applied to the events survived the pre-selection cuts and dE/dX cuts. Because $1/\beta$ distribution were described well by Gaussian as shown in Figure ?? and half-width of the $1/\beta$ selection band was set at 3.89 σ, the efficiency is very close to unity (99.99 % for a pure Gaussian).

(4) dE/dX cut efficiency ($\epsilon_{dE/dX}$)

The data sample in lower TOF scintillators was used to estimated the dE/dX cut efficiency. The region of dE/dX-band cut is applied to 0.5-3.5 MIPs in dE/dX distribution as shown in Section 4.2.1. dE/dX cut efficiency is given by

$$\epsilon_{dE/dX} = \frac{C \bigcap D}{C},$$

where C is the number of events passing through "fiducial volume" and applying to "$1/\beta$-band cut", D is the number of events under the condition of "dE/dX cut". Figure 4.12 shows the dE/dX cut efficiencies for positive and negative muons.

(5) Accidental Hits Efficiency ($\epsilon_{accident}$)

When an accidental particle passed through the TOF and left "accidental hits", the pre-selection would eliminate the event. The inefficiency of this rejection for the accidental hits can be estimated by utilizing the random trigger samples during the experiments. The random triggers were made at every 0.8 second during the flight independent of T0 trigger. Therefore, the numbers of hits in the random trigger samples corresponds to the number of accidental hits.

Figure 4.13 shows the number of hits in the upper and the lower TOF for all random trigger samples.

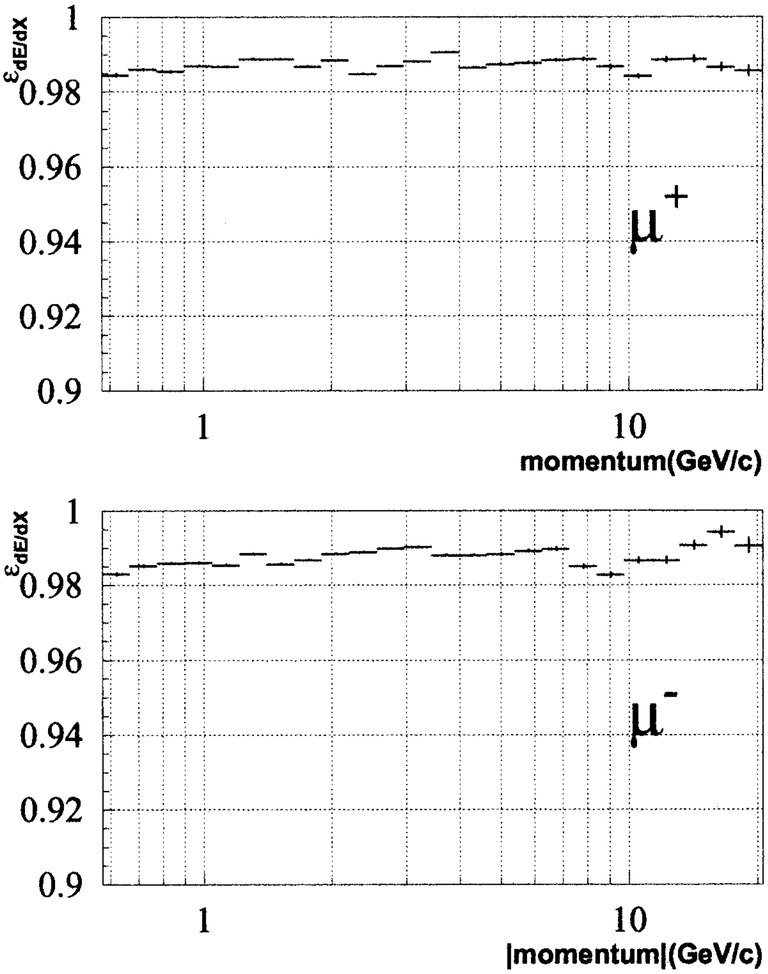

Figure 4.12: dE/dX cut efficiency for muons. (top)positive muon, and (bottom)negative muon.

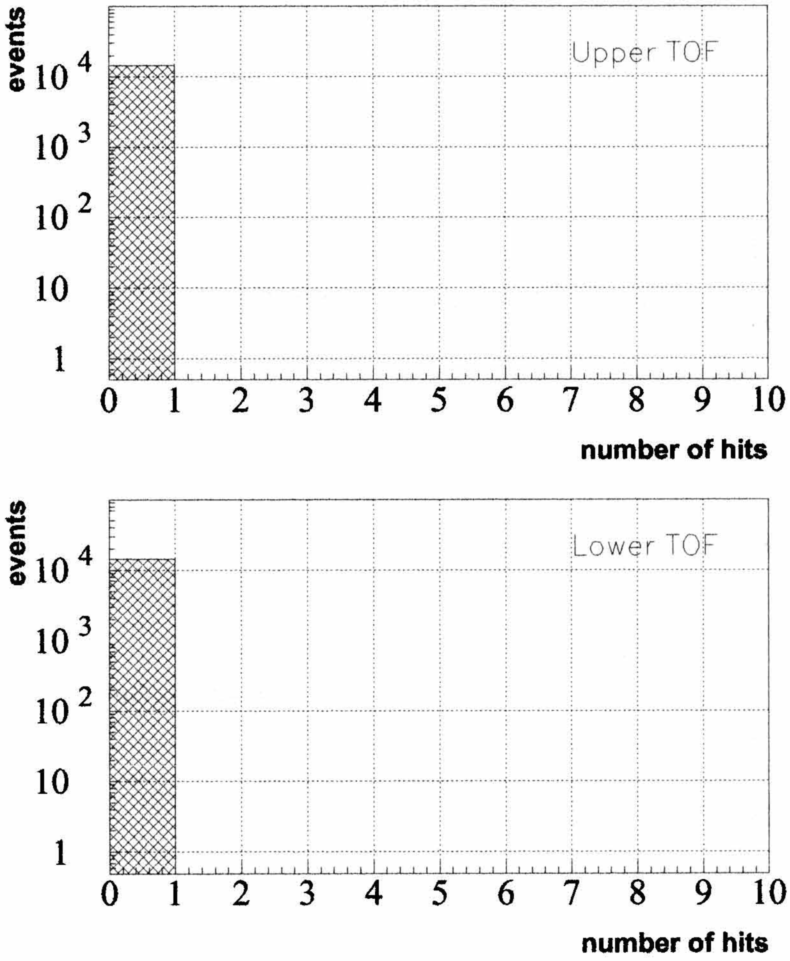

Figure 4.13: Distributions of the number of TOF hits among random trigger samples in (top)upper TOF and (bottom)lower TOF

Since the pre-selection allows one or two hits in upper and lower TOF counters, random trigger events are eliminated due to the upper and lower accidental hits. From this study, accidental hit efficiency is zero and we estimate,

$$(1 - \epsilon_{accident}) \sim 100\%.$$

4.5 Background Corrections

4.5.1 Electrons and Positrons

To estimate electron contamination in the muon, we used the information of dE/dX in the lower TOF scintilator. In the fiducial volume for muons, lead plate of two radiation length were placed just above the lower TOF hodoscope. Electrons produce electromagnetic shower and thus leaving large energy deposite inside the lower TOF counters, while muon events are minimum ionizing particles(MIPs) with no strong interactions.

Using real data for muons and Monte Carlo simulation(M.C.) for electrons, number of electrons which are not rejected in dE/dX cut(Section 4.2.1) was examined in the region of dE/dX in the lower TOF between 0.5 and 3.5 MIPs.

Figure 4.14, Figure 4.15 and Figure 4.16 show dE/dX distribution in the lower TOF for electrons using M.C. in the top view and observed data in the bottom view, in momentum regions 0.5-0.9, 1.6-3.0 and 5.4-10.0 GeV/c, respectively. The dE/dX in the lower TOF for electrons using M.C. distributes broadly in whole region of dE/dX distribution. The dE/dX in the lower TOF for observed data distribute around 1 MIP. Since muon candidates are almost observed, electron candidates are scarcely observed on the ground in the momentum region 0.5-10.0 GeV/c, comparing with Figure 4.14, Figure 4.15 and Figure 4.16 indicate the results in different momentum region. However there are a few electron candidates in a region of lower TOF dE/dX between 0.5 and 3.5 MIPs.

In order to estimate electron contamination, at first, three regions are divided dE/dX in the lower TOF distribution in figure 4.17 In Figure 4.17, in momentum region 0.5-0.9 GeV/c, a region of dE/dX in the lower TOF between 0.5 and 3.5 MIPs is denoted as the region (A), two regions of dE/dX in the lower TOF below 0.5 MIPs and above 3.5 MIPs are denoted as (B). Table 4.3 is summarized the definition of two regions devided dE/dX in the lower TOF distribution. In observed data, all events in regions of (B) were assumed electron cadidates because these are distributed broadly in dE/dX in the lower TOF by cascade shower.

Table 4.3: The definition of two of (A) and (B) deviding dE/dX distribution.

$dE/dX_{lowerTOF}$(MIPs)	region
0.5 - 3.5	(A)
<0.5, >3.5	(B)

Second, the number of electrons for observed data and M.C. are defined each regions of (A) and (B). The number of electrons for observed data in regions of (B) notes $N_{obs(B)}$. The number estimated of electrons for observed data in the region (A) is denoted as $N_{obs(A)}$. In the same way, the number of electrons for M.C. in regions of (B) is denoted as $N_{mc(B)}$. the number of electrons for M.C. in regions of (A) as $N_{mc(A)}$.

The ratio of $N_{mc(A)}$ to $N_{mc(B)}$ is calculated, the ratio of $N_{obs(A)}$ to $N_{obs(B)}$ is compared with $N_{mc(A)}/N_{mc(B)}$ ratio.

The number of electron candidates for observed data in a region of (A) was estimated as follow;

$$N_{obs(A)} = N_{obs(B)} \cdot \frac{N_{mc(A)}}{N_{mc(B)}} \tag{4.5}$$

where

$N_{obs(A)}$: number of electrons estimated for observed data in the region (A)
$N_{obs(B)}$: number of electrons for observed data in the region (B)
$N_{mc(A)}$: number of electrons estimated for M.C. in the region (A)
$N_{mc(B)}$: number of electrons estimated for M.C. in the region (B)

In the same way, the number of electrons for observed data in a region of (A) is estimated each momentum region.

Figure 4.18 shows e/μ ratio for each momentum in the fiducial volume with lead plate. The e^-/μ^- ratio decreased rapidly as momentum. The e^-/μ^- ratio was less than 1% above 0.5 GeV/c, and described as a simple power low as $e^-/\mu^- = a \times P^b$, where $a = 0.288 \times 10^{-2} \pm 0.286 \times 10^{-3}$, $b = -2.279 \pm 0.181$.

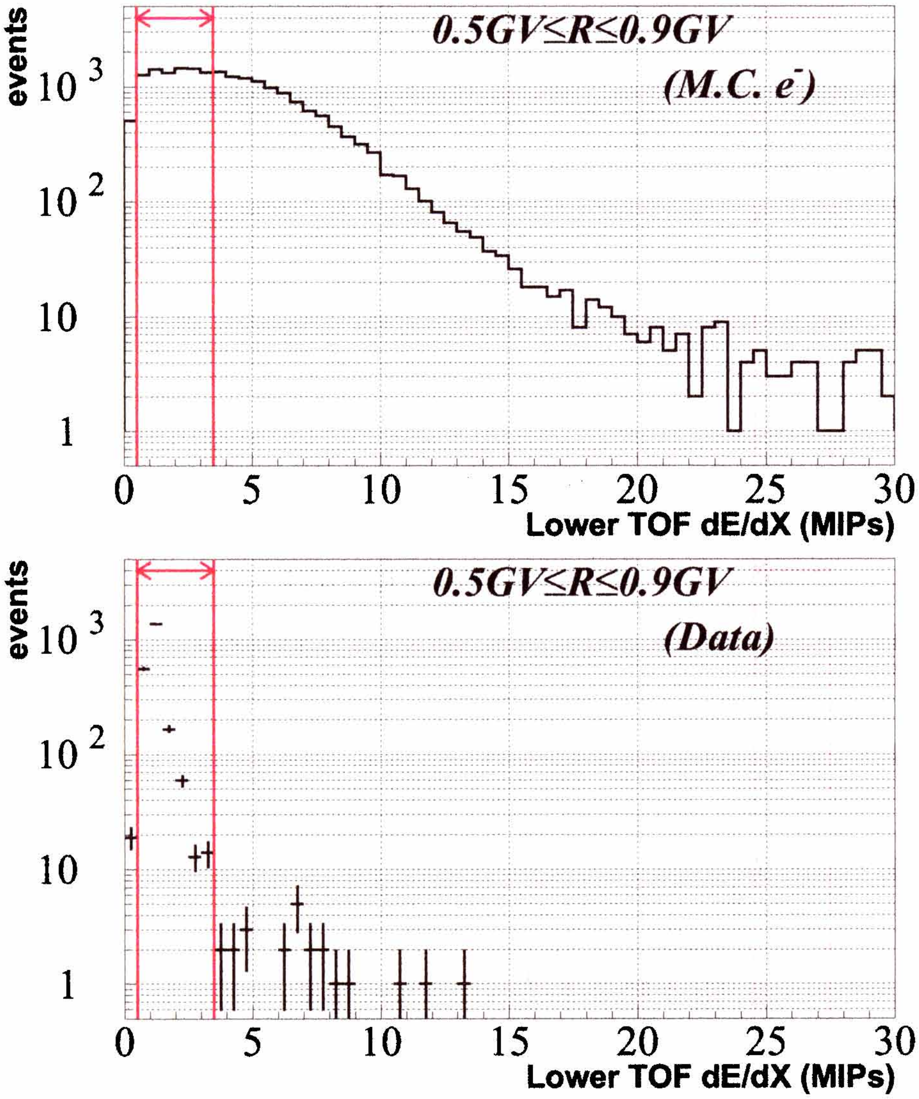

Figure 4.14: Lower TOF dE/dX distribution for (top)electrons using Monte Carlo and (bottom)real data in the momentum region 0.5-0.9 GeV/c. Red arrow means the region which is used in dE/dX cut criteria(see Section 4.2.1).

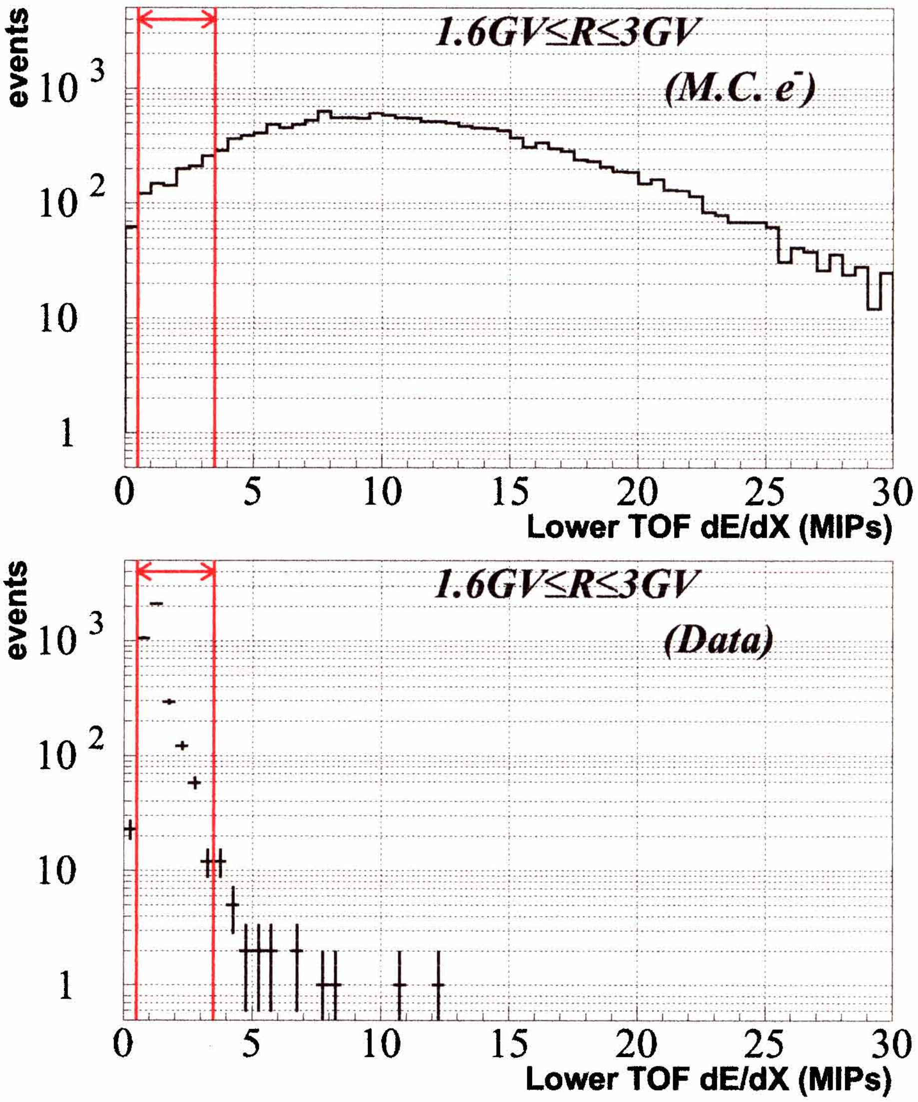

Figure 4.15: Lower TOF dE/dX distribution for (top)electrons using Monte Carlo and (bottom)real data in momentum region 1.6-3.0 GeV/c. Red arrow means the region which is used in dE/dX cut criteria(see Section 4.2.1).

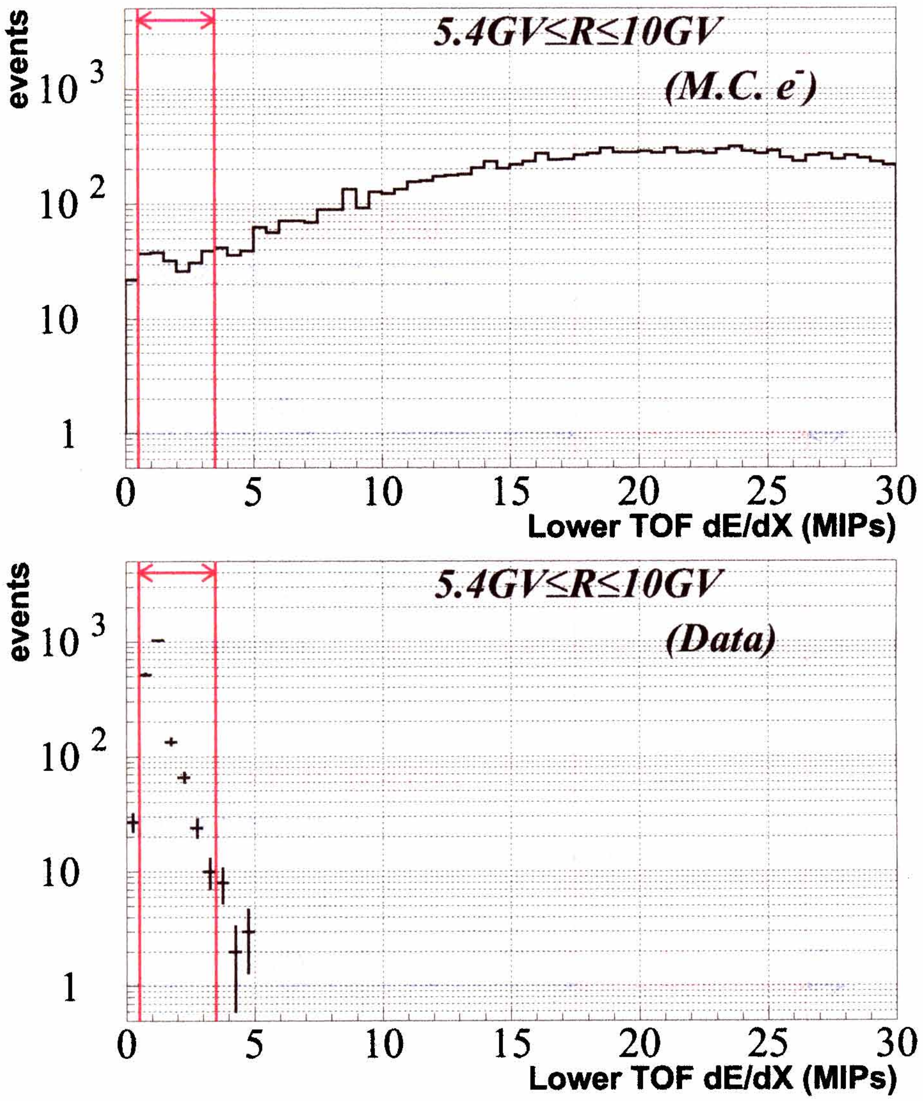

Figure 4.16: Lower TOF dE/dX distribution for (top)electrons using Monte Carlo and (bottom)real data in momentum region 5.4-10.0 GeV/c. Red arrow means the region which is used in dE/dX cut criteria(see Section 4.2.1).

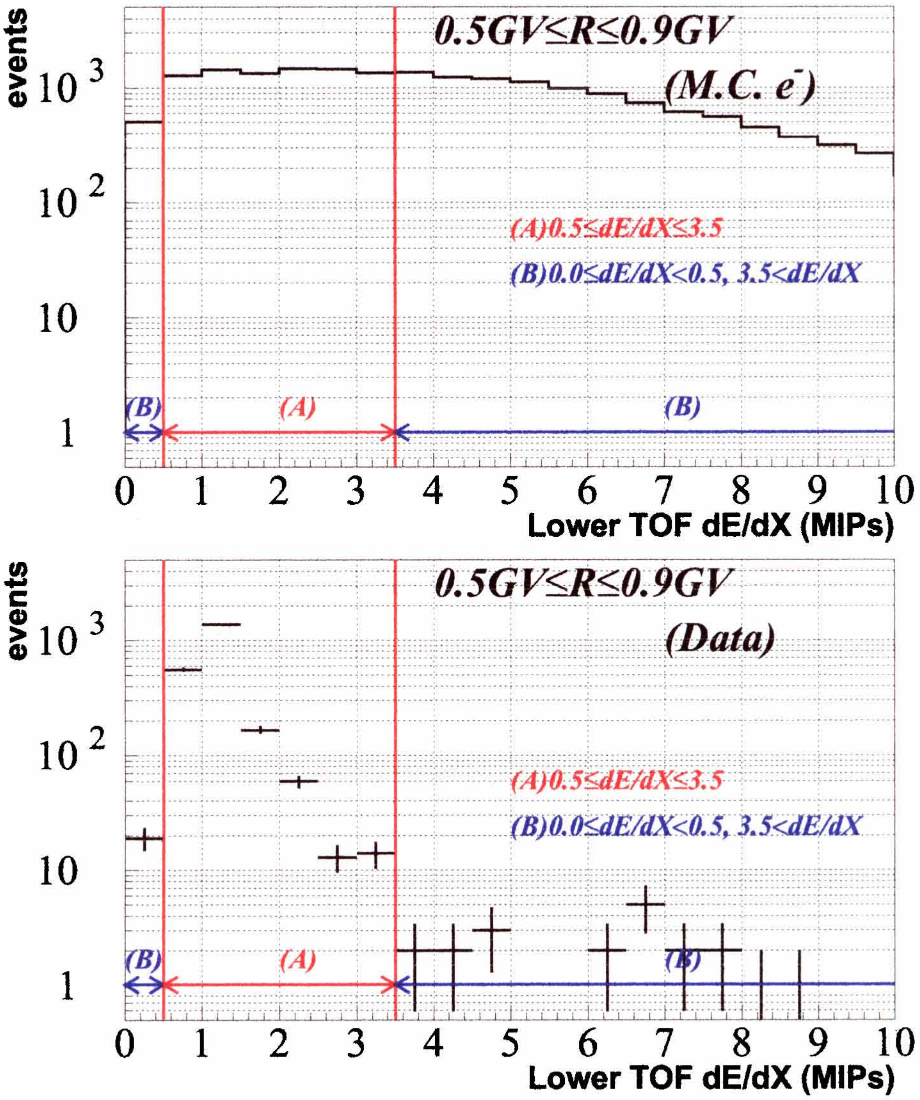

Figure 4.17: Lower TOF dE/dX distribution for (top)electrons using Monte Carlo and (bottom)real data in momentum region 5.4-10.0 GeV/c. Figure 4.14 is closed up in dE/dX range 0.0-10.0 MIPs.

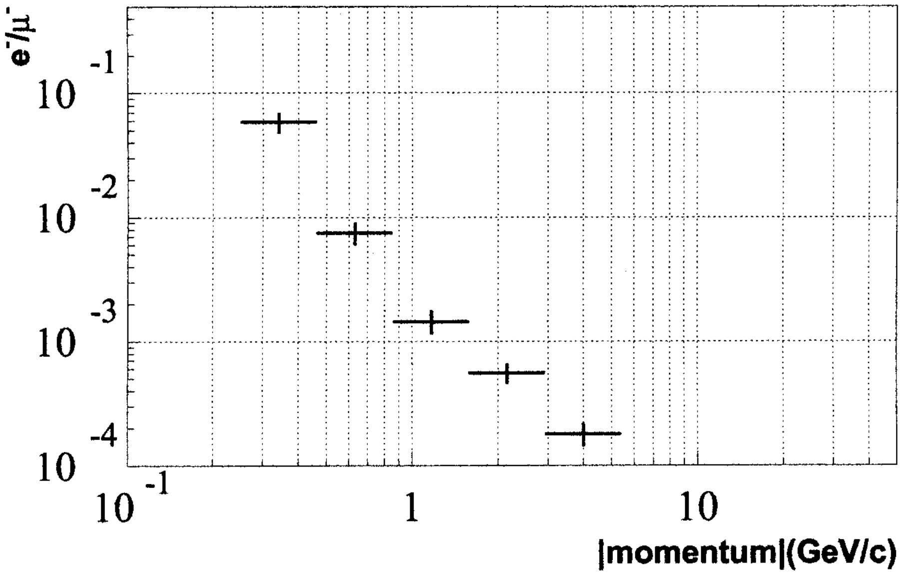

Figure 4.18: The e^-/μ^- ratio in whole fiducial volume and fiducial volume within lead region.

4.5.2 Protons

As seen in Figure 4.20(top), main background sources was proton for positive charged muons. To estimate the number of protons for each momentum, we divided into three momentum regions(see Table 4.4).

Protons were identified by examining $1/\beta$ distribution vs rigidity as shown in Figure 4.20(top). Below 1.6 GeV/c, protons were clearly separated from muons. Between 1.6 and 3.4 GeV/c, the proton contamination in the muon candidates was estimated by fitting the $1/\beta$ distribution with a double-Gaussian function as shown in Figure 4.19. The ratio of observed protons to muons was found to be well described as a simple power low as $p/\mu^+ = 0.14 \times P^{-0.98}$ in a momentum region of 1.0-3.4 GeV/c. The proton contamination above 3.4 GeV/c was estimated by extrapolating this power law. Above around 10 GeV/c, however, the p/μ^+ ratio will be constant [42].

Table 4.4: Three momentum regions for study of protons separation from muons

region	momentum(GeV/c)	comment
(a)	0.1 $\sim$ 1.6	Protons were clearly separated from muons.
(b)	1.6 $\sim$ 3.4	Begining of proton contamination.
(c)	3.4 $\sim$	Contaminated completely with protons.

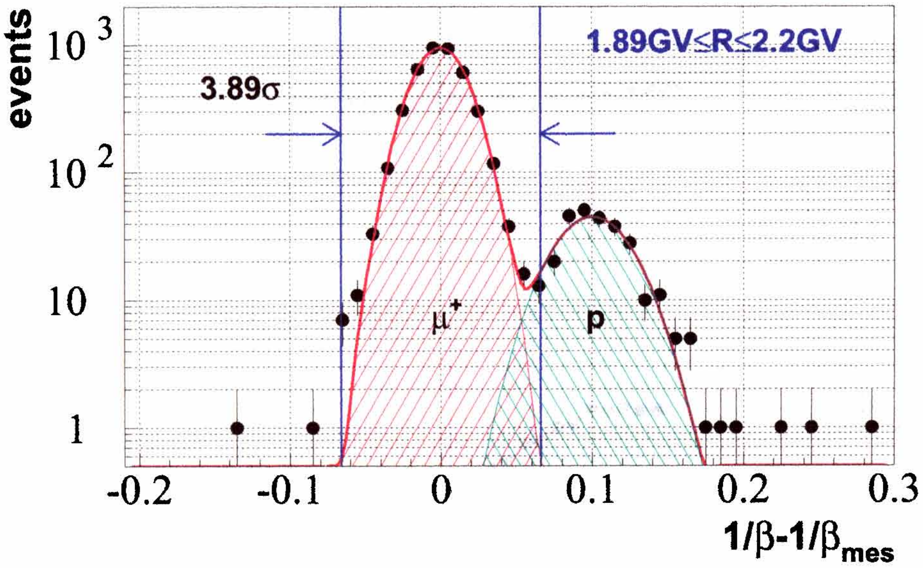

Figure 4.19: An estimation of proton contamination by lower TOF information.

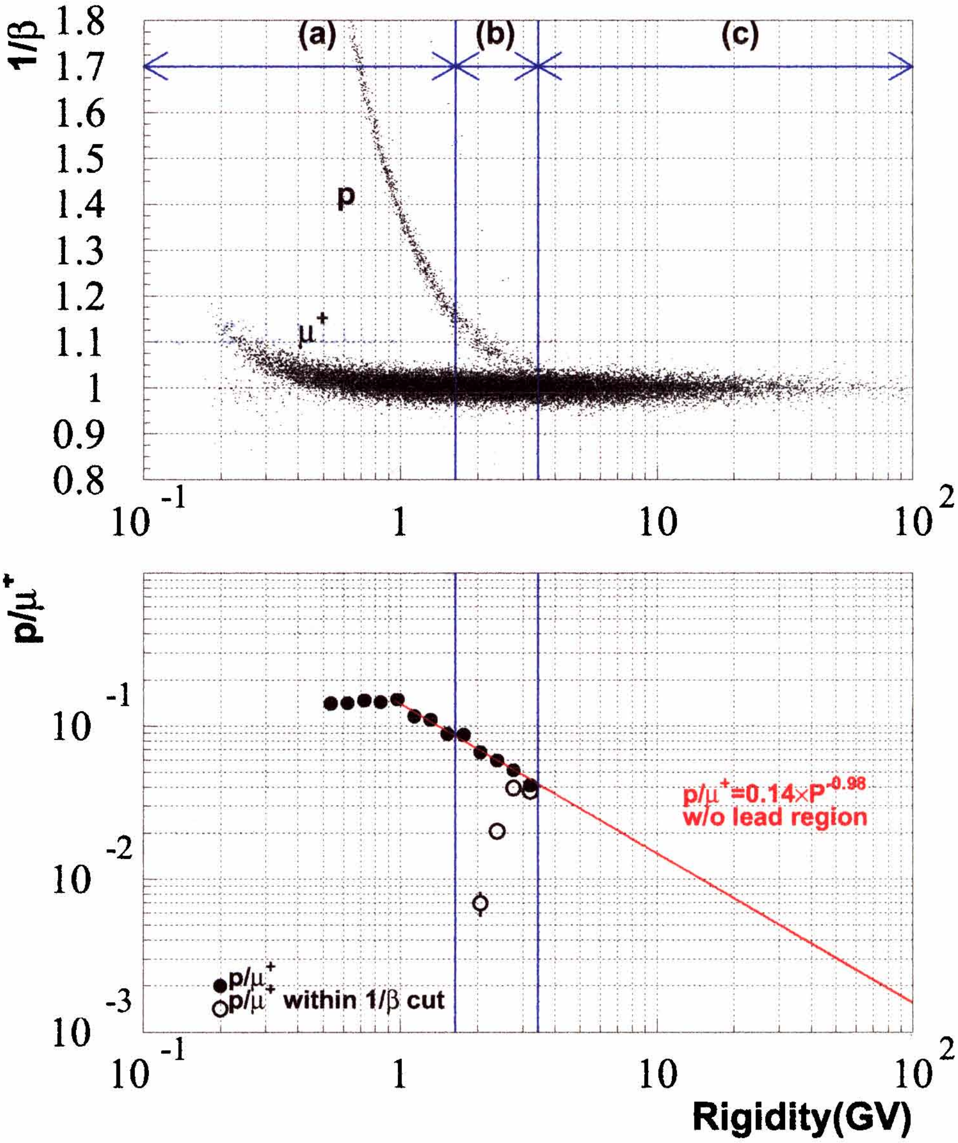

Figure 4.20: (top)$1/\beta$ distribution for positive region with three divisions. (bottom)p/μ^+ ratio and fitting result with power law

Chapter 5

Experiment results

5.1 Results

The fluxes of μ^+ and μ^-, and μ^+/μ^- charge ratio were obtained in the momentum range of 0.5-100 GeV/c, and they were given in Table 5.5 and Table 5.6. The fluxes and μ^+/μ^- charge ratio are shown in Figure 5.1 and Figure 5.2, respectively.

The resultant data of positive and negative differential muon fluxes are given in Table 5.5 and Table 5.6. Mean momentum in Table 5.5 and Table 5.6 are described mean value for events in each momentum range.

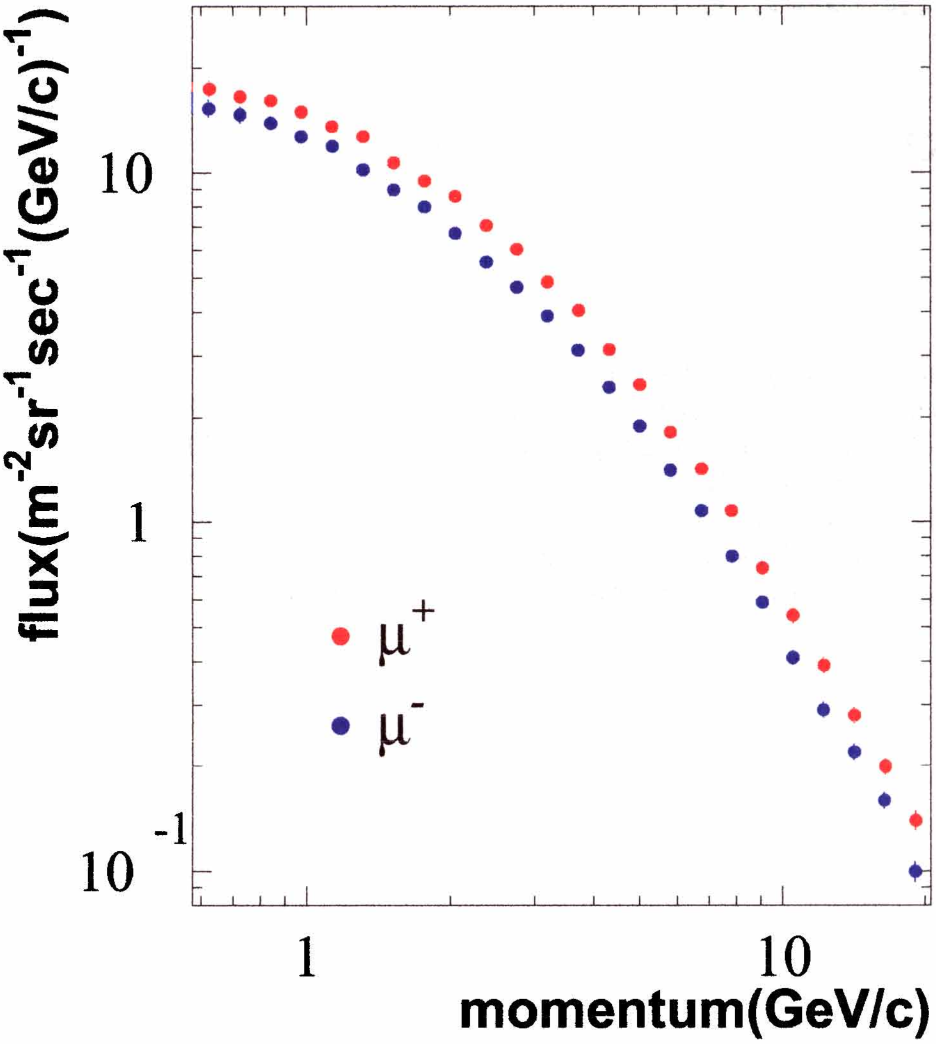

Figure 5.1: The measured vertical differential momentum spectra of the positive and negative muons at ground level.

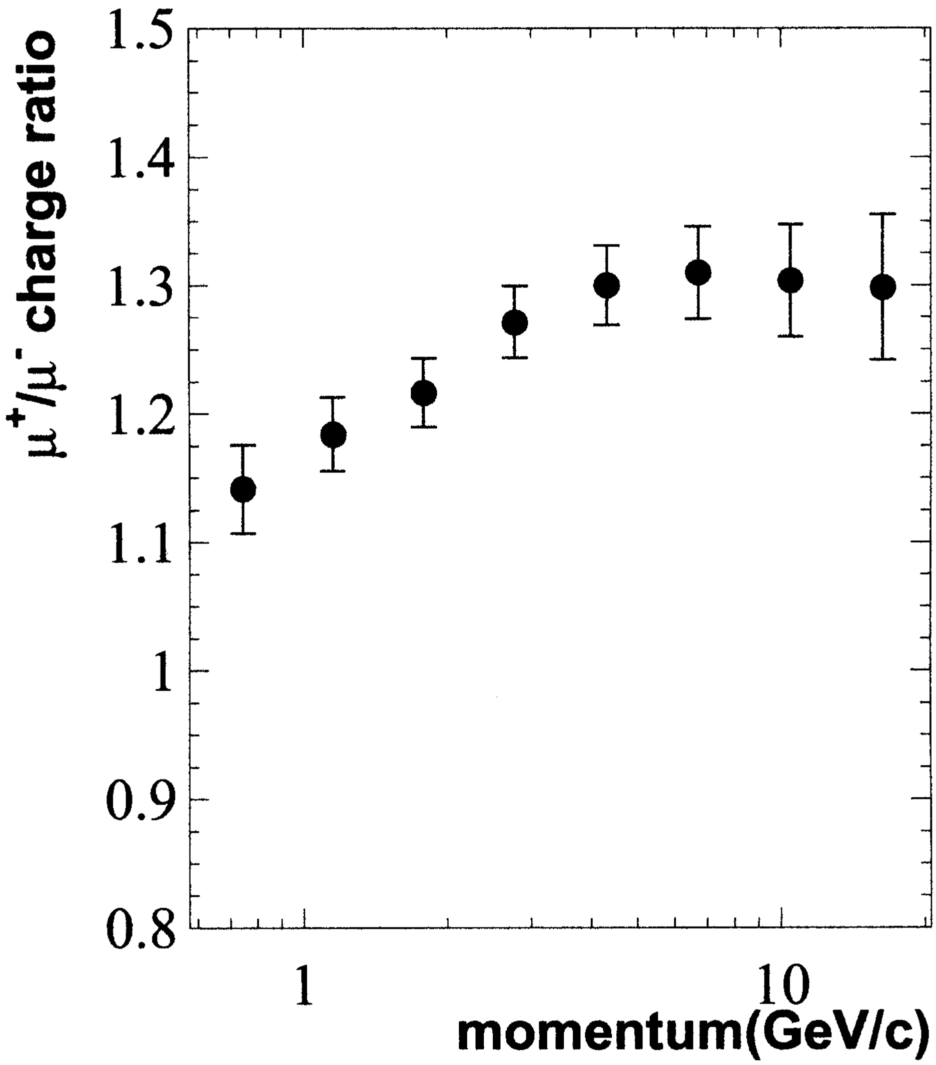

Figure 5.2: μ^+/μ^- charge ratio of atmospheric muons.

5.2 Estimation of Errors

The following expression of the uncertainty of fluxes is derived from the equation 4.3, assuming the variables are independent of each other:

$$\begin{aligned}\left|\frac{\Delta F}{F}\right|^2 = &\left|\frac{\Delta N_{obs}}{N_{obs}}\right|^2 + \left|\frac{\Delta (S\Omega)}{S\Omega}\right|^2 + \left|\frac{\Delta T_{live}}{T_{live}}\right|^2 + \left|\frac{\Delta \epsilon_{single}}{\epsilon_{single}}\right|^2 \\ &+ \left|\frac{\Delta \epsilon_{dE/dX}}{\epsilon_{dE/dX}}\right|^2 + \left|\frac{\Delta \epsilon_{1/\beta}}{\epsilon_{1/\beta}}\right|^2 + \left|\frac{\Delta N_{BG}}{N_{obs} - N_{BG}}\right|^2 .\end{aligned} \tag{5.1}$$

The first term is the statistical error and the others are systematic errors.

5.2.1 Statistical Errors $\left(\frac{\Delta N_{obs}}{N_{obs}}\right)$

For the positive and negative muon fluxes, the number of events in each momentum region is large as shown in Table 5.1 and Table 5.2.

In table 5.1 as proton contamination in the muon, muon events are free from the background of protons, since the number of protons in momentum range 0.496-1.634 *GeV/c* is zero. Above 1.634 *GeV/c* in momentum range, the number of protons within $1/\beta$-band were counted as the background (see Section 4.5.2).

For electron contamination in negative momentum range (Table 5.2) and positron contamination in positive momentum range (Table 5.1), the number of electrons and positrons were counted within dE/dX-band as the background (see Section 4.5.1).

Table 5.1: Estimated number of positive muons and background from positrons and protons.

momentum(GeV/c)	$N_{\mu^+_{obs}}$	N_{e^+}	N_p	N_{μ^+}
0.576 - 0.669	2513	21.40	0	2492±50
0.669 - 0.776	3017	18.51	0	2998±55
0.776 - 0.901	3496	15.46	0	3481±59
0.901 - 1.045	3977	12.67	0	3964±63
1.045 - 1.213	4268	9.80	0	4258±65
1.213 - 1.408	4696	7.77	0	4688±68
1.408 - 1.634	4667	5.57	0	4661±68
1.634 - 1.896	4779	4.11	0.96	4774±69
1.896 - 2.201	5077	3.14	35.31	5039±71
2.201 - 2.555	4859	2.17	100.10	4757±69
2.555 - 2.965	4889	1.57	192.63	4695±69
2.965 - 3.441	4600	1.07	172.04	4427±67
3.441 - 3.993	4382	0.73	169.43	4212±65
3.993 - 4.635	3934	0.47	131.45	3802±62
4.635 - 5.379	3626	0.31	104.71	3521±59
5.379 - 6.243	3110	0.19	77.61	3032±55
6.243 - 7.246	2745	0.12	59.20	2686±52
7.246 - 8.409	2416	0.08	45.03	2371±49
8.409 - 9.760	2012	0.05	32.41	1980±44
9.760 - 11.33	1726	0.03	24.02	1702±41
11.33 - 13.15	1431	0.02	17.21	1414±38
13.15 - 15.26	1142	0.01	11.87	1130±34
11.327 - 13.146	1431	0.02	17.21	1414±38
13.146 - 15.258	1142	0.01	11.87	1130±34
15.258 - 17.708	964	0.01	8.66	955±31
17.708 - 20.552	765	0.00	5.94	759±28

Table 5.2: Estimated number of negative muons and background from electrons.

momentum(GeV/c)	$N_{\mu^-_{obs}}$	N_{e^-}	N_{μ^-}
0.576 - 0.669	2243	19.10	2224 ± 47
0.669 - 0.776	2616	16.05	2600 ± 51
0.776 - 0.901	2984	13.20	2971 ± 55
0.901 - 1.045	3327	10.60	3316 ± 58
1.045 - 1.213	3686	8.46	3678 ± 61
1.213 - 1.408	3805	6.30	3799 ± 62
1.408 - 1.634	3988	4.76	3983 ± 63
1.634 - 1.896	4067	3.49	4064 ± 64
1.896 - 2.201	3956	2.45	3954 ± 63
2.201 - 2.555	3844	1.72	3842 ± 62
2.555 - 2.965	3787	1.22	3786 ± 62
2.965 - 3.441	3625	0.84	3624 ± 60
3.441 - 3.993	3397	0.57	3396 ± 58
3.993 - 4.635	3067	0.37	3067 ± 55
4.635 - 5.379	2740	0.24	2740 ± 52
5.379 - 6.243	2404	0.15	2404 ± 49
6.243 - 7.246	2096	0.09	2096 ± 46
7.246 - 8.409	1820	0.06	1820 ± 43
8.409 - 9.760	1568	0.04	1568 ± 40
9.760 - 11.33	1283	0.02	1283 ± 36
11.33 - 13.15	1065	0.01	1065 ± 33
13.15 - 15.26	915	0.01	915 ± 30
11.327 - 13.146	1065	0.01	1065 ± 33
13.146 - 15.258	915	0.01	915 ± 30
15.258 - 17.708	750	0.00	750 ± 27
17.708 - 20.552	527	0.00	527 ± 23

5.2.2 Systematic Errors

- **Geometrical acceptance** $\left(\frac{\Delta(S\Omega)}{S\Omega}\right)$

  The geometrical acceptance was obtained from the Monte Carlo simulation with turning off the interaction and energy loss switches. The geometrical acceptance is prescribed by "fiducial volume" cut, namely by N_{expect}, Z_{trackU}, and Z_{trackL} which were described in Section 4.4.2. The error comes from the uncertainty of the detector alignment which is estimated as less than 1 mm, corresponding to about 1 % systematic error of the acceptance by upper and lower TOF hodoscopes.

- **Live time** $\left(\frac{\Delta T_{live}}{T_{live}}\right)$

  The live time was directly measured by using a clock with the resolution of 10^{-6}sec. Therefore, the error in the live time should be negligibly small.

- **Single track efficiency** $\left(\frac{\Delta\epsilon_{single}}{\epsilon_{single}}\right)$

  To estimate the systematic error in single track efficiency, we compared the hit number of lower TOF(N_{TOFL}) covered with lead in observed and in simulation data. The differences in the observed and simulation data were 2.2 % at 0.5 GeV/c, 0.9 % at 1 GeV/c, 0.5 % at 3 GeV/c and 0.6 % at 10 GeV/c in positive momentum region, and 2.9 % at 0.5 GeV/c, 1.2 % at 1 GeV/c, 0.5 % at 3 GeV/c and 0.2 % at 10 GeV/c in negative momentum region. These differeces are mainly due to the uncertainty of material distribution in lower side of BESS detector. Since the material distribution in upper side is the same as lower side, we multiplied these value by $\sqrt{2}$ for the uncertainties of the material thickness. The total systematic error due to the uncertainty of material distribution was calculated to be 3.1, 1.3, 0.7 and 0.8 % at 0.5, 1.0, 3.0 and 10.0 GeV/c in positive momentum region, and 4.1, 1.7, 0.7 and 0.3 % at 0.5, 1.0, 3.0 and 10.0 GeV/c in negative momentum region, respectively.

$$\left(\frac{\Delta\epsilon_{single}}{\epsilon_{single}}\right)_+ = \begin{cases} \pm\ 2.4\ \% & (at\ 0.6\ GeV/c) \\ \pm\ 1.3\ \% & (at\ 1\ GeV/c) \\ \pm\ 0.7\ \% & (at\ 3\ GeV/c) \\ \pm\ 0.8\ \% & (at\ 10\ GeV/c) \end{cases}$$

$$\left(\frac{\Delta\epsilon_{single}}{\epsilon_{single}}\right)_- = \begin{cases} \pm\ 3.1\ \% & (at\ 0.6\ GeV/c) \\ \pm\ 1.7\ \% & (at\ 1\ GeV/c) \\ \pm\ 0.7\ \% & (at\ 3\ GeV/c) \\ \pm\ 0.3\ \% & (at\ 10\ GeV/c) \end{cases}$$

- **dE/dX cut efficiency** $\left(\frac{\Delta\epsilon_{dE/dX}}{\epsilon_{dE/dX}}\right)$

  We compared dE/dX cut in the lower TOF efficiencies of the observed data and the simulation data in the same conditioning cut. In the observed data, the events passed through the fiducial volume with lead region were selected. The systematic error of dE/dX cut efficiency was follows.

$$\left(\frac{\Delta\epsilon_{dE/dX}}{\epsilon_{dE/dX}}\right)_+ = \begin{cases} \pm\ 1.2\ \% & (at\ 0.6\ GeV/c) \\ \pm\ 1.1\ \% & (at\ 1\ GeV/c) \\ \pm\ 1.3\ \% & (at\ 3\ GeV/c) \\ \pm\ 1.6\ \% & (at\ 10\ GeV/c) \end{cases}$$

$$\left(\frac{\Delta\epsilon_{dE/dX}}{\epsilon_{dE/dX}}\right)_- = \begin{cases} \pm\ 1.8\ \% & (at\ 0.6\ GeV/c) \\ \pm\ 1.4\ \% & (at\ 1\ GeV/c) \\ \pm\ 1.1\ \% & (at\ 3\ GeV/c) \\ \pm\ 1.2\ \% & (at\ 10\ GeV/c) \end{cases}$$

- $1/\beta$ **cut efficiency** $\left(\frac{\Delta\epsilon_{1/\beta}}{\epsilon_{1/\beta}}\right)$

  We estimated $1/\beta$ band cut efficiency to be 99.99 % assuming that $1/\beta$ distribution is follows Gaussian distribution. We checked the efficiency for the muon events in observed data, which were selected using negative muon identification cuts except for $1/\beta$ band cut. The efficiency was found to be above 99.88 %. The systematic error of $1/\beta$ cut efficiency was subtracted $1/\beta$ cut efficiency in observed data from 99.99 % in Gaussian.

$$\left(\frac{\Delta\epsilon_{1/\beta}}{\epsilon_{1/\beta}}\right)_\pm = \begin{cases} \pm\ 0.02\ \% & (at\ 0.6\ GeV/c) \\ \pm\ 0.11\ \% & (at\ 1\ GeV/c) \\ \pm\ 0.05\ \% & (at\ 3\ GeV/c) \\ \pm\ 0.01\ \% & (at\ 10\ GeV/c) \end{cases}$$

- **Background subtraction** $\left(\frac{\Delta N_{BG}}{N_{obs}-N_{BG}}\right)$

  We subtracted the electrons from observed negative muon candidates. The systematic error comes from assuming electron candidates are the events between 0.5 and 3.5 MIPs in dE/dX distribution in the lower TOF with lead region.

$$\left(\frac{\Delta N_{BG}}{N_{obs}-N_{BG}}\right)_- = \left(\frac{\Delta N_{e^-}}{N_{obs}-N_{e^-}}\right) = \begin{cases} \pm\ 0.29\ \% & (at\ 0.6\ GeV/c) \\ \pm\ 0.08\ \% & (at\ 1\ GeV/c) \\ \pm\ 0.04\ \% & (at\ 3\ GeV/c) \\ \pm\ 0.03\ \% & (at\ 10\ GeV/c) \\ \pm\ 0.03\ \% & (at\ 20\ GeV/c) \end{cases}$$

We subtracted the positrons and protons from observed positive muon candidates. The systematic error comes from only positron candidates in momentum range 0.5-1.6 GeV/c because protons and positive muons are separated completely, and from both of proton and positron candidates in momentum above 1.6 GeV/c.

$$\left(\frac{\Delta N_{BG}}{N_{obs}-N_{BG}}\right)_{+} = \left(\frac{\Delta N_{e^+}}{N_{obs}-N_{e^+}}\right) = \begin{cases} \pm\, 0.29\ \% & (at\ 0.6\ GeV/c) \\ \pm\, 0.08\ \% & (at\ 1\ GeV/c) \end{cases}$$

$$\left(\frac{\Delta N_{BG}}{N_{obs}-N_{BG}}\right)_{+} = \left(\frac{\Delta (N_{e^+}+N_p)}{N_{obs}-(N_{e^+}+N_p)}\right) = \begin{cases} \pm\, 0.06\ \% & (at\ 3\ GeV/c) \\ \pm\, 0.03\ \% & (at\ 10\ GeV/c) \\ \pm\, 0.05\ \% & (at\ 20\ GeV/c) \end{cases}$$

The total and each systematic errors of positive and negative muons are shown in Figure 5.3 and Figure 5.4,respectively.

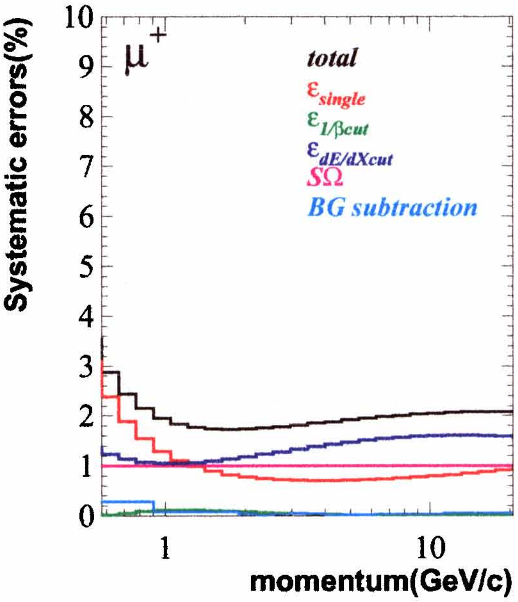

Figure 5.3: Total and individual systematic errors for positive muons.

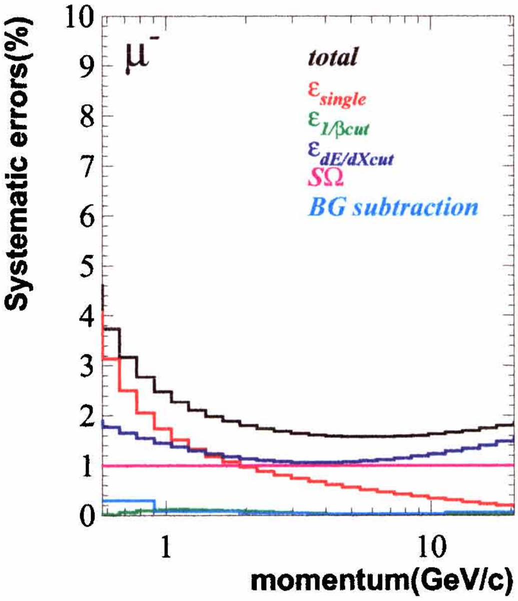

Figure 5.4: Total and individual systematic errors for negative muons.

Table 5.3: Summary of the systematic errors for positive muon flux.

momentum range(GeV/c)	$S\Omega$ (%)	ϵ_{single} (%)	$\epsilon_{1/\beta cut}$ (%)	$\epsilon_{dE/dXcut}$ (%)	Background subtraction(%)	Total (%)
0.576 - 0.669	1.00	2.39	0.02	1.23	0.29	2.88
0.669 - 0.776	1.00	1.89	0.06	1.14	0.29	2.44
0.776 - 0.901	1.00	1.54	0.09	1.08	0.29	2.15
0.901 - 1.045	1.00	1.29	0.11	1.05	0.08	1.95
1.045 - 1.213	1.00	1.12	0.12	1.05	0.08	1.84
1.213 - 1.408	1.00	0.99	0.12	1.07	0.08	1.77
1.408 - 1.634	1.00	0.89	0.11	1.10	0.08	1.74
1.634 - 1.896	1.00	0.82	0.09	1.14	0.08	1.73
1.896 - 2.201	1.00	0.78	0.08	1.18	0.04	1.74
2.201 - 2.555	1.00	0.74	0.07	1.23	0.01	1.76
2.555 - 2.965	1.00	0.72	0.06	1.29	0.04	1.78
2.965 - 3.441	1.00	0.71	0.05	1.34	0.06	1.82
3.441 - 3.993	1.00	0.71	0.04	1.39	0.04	1.85
3.993 - 4.635	1.00	0.71	0.03	1.43	0.03	1.88
4.635 - 5.379	1.00	0.71	0.03	1.47	0.03	1.92
5.379 - 6.243	1.00	0.72	0.02	1.51	0.03	1.95
6.243 - 7.246	1.00	0.74	0.02	1.54	0.03	1.98
7.246 - 8.409	1.00	0.76	0.01	1.57	0.03	2.01
8.409 - 9.760	1.00	0.78	0.01	1.59	0.03	2.03
9.760 - 11.327	1.00	0.80	0.01	1.60	0.03	2.05
11.327 - 13.146	1.00	0.83	0.01	1.61	0.05	2.07
13.146 - 15.258	1.00	0.85	0.01	1.61	0.05	2.08
15.258 - 17.708	1.00	0.88	0.01	1.60	0.05	2.08
17.708 - 20.552	1.00	0.91	0.01	1.59	0.05	2.09

Table 5.4: Summary of the systematic errors for negative muon flux.

momentum range(GeV/c)	$S\Omega$ (%)	ϵ_{single} (%)	$\epsilon_{1/\beta cut}$ (%)	$\epsilon_{dE/dX cut}$ (%)	Background subtraction(%)	Total (%)
0.576 - 0.669	1.00	3.13	0.02	1.76	0.29	3.74
0.669 - 0.776	1.00	2.50	0.06	1.65	0.29	3.17
0.776 - 0.901	1.00	2.05	0.09	1.54	0.29	2.77
0.901 - 1.045	1.00	1.74	0.11	1.45	0.08	2.48
1.045 - 1.213	1.00	1.50	0.12	1.36	0.08	2.27
1.213 - 1.408	1.00	1.33	0.12	1.29	0.08	2.11
1.408 - 1.634	1.00	1.18	0.11	1.23	0.08	1.98
1.634 - 1.896	1.00	1.07	0.09	1.18	0.08	1.88
1.896 - 2.201	1.00	0.97	0.08	1.14	0.04	1.80
2.201 - 2.555	1.00	0.88	0.07	1.10	0.04	1.73
2.555 - 2.965	1.00	0.81	0.06	1.08	0.04	1.68
2.965 - 3.441	1.00	0.74	0.05	1.07	0.04	1.64
3.441 - 3.993	1.00	0.68	0.04	1.06	0.03	1.61
3.993 - 4.635	1.00	0.62	0.03	1.06	0.03	1.59
4.635 - 5.379	1.00	0.56	0.03	1.07	0.03	1.57
5.379 - 6.243	1.00	0.51	0.02	1.09	0.03	1.57
6.243 - 7.246	1.00	0.46	0.02	1.12	0.03	1.57
7.246 - 8.409	1.00	0.42	0.01	1.15	0.03	1.58
8.409 - 9.760	1.00	0.38	0.01	1.19	0.03	1.60
9.760 - 11.327	1.00	0.34	0.01	1.23	0.03	1.62
11.327 - 13.146	1.00	0.30	0.01	1.28	0.05	1.66
13.146 - 15.258	1.00	0.26	0.01	1.34	0.05	1.70
15.258 - 17.708	1.00	0.23	0.01	1.41	0.05	1.74
17.708 - 20.552	1.00	0.20	0.01	1.48	0.05	1.79

Table 5.5: Summary of positive muon flux

Momentum range (GeV/c)	Mean momentum (GeV/c)	μ^+ flux $(m^{-2}sr^{-1}s^{-1}(GeV/c)^{-1})$	Statistical error	Systematic error
0.576-0.669	0.625	17.48	0.391	0.501
0.669-0.776	0.724	16.55	0.342	0.401
0.776-0.901	0.840	16.15	0.306	0.344
0.901-1.045	0.974	15.01	0.269	0.292
1.045-1.213	1.130	13.60	0.235	0.250
1.213-1.408	1.311	12.71	0.209	0.225
1.408-1.634	1.521	10.73	0.177	0.186
1.634-1.896	1.765	9.50	0.154	0.164
1.896-2.201	2.047	8.60	0.136	0.149
2.201-2.555	2.379	7.08	0.114	0.124
2.555-2.965	2.760	6.06	0.098	0.108
2.965-3.441	3.201	4.87	0.081	0.088
3.441-3.993	3.717	4.05	0.069	0.075
3.993-4.635	4.308	3.12	0.056	0.059
4.635-5.379	4.997	2.48	0.046	0.047
5.379-6.243	5.801	1.81	0.037	0.035
6.243-7.246	6.737	1.42	0.030	0.028
7.246-8.409	7.804	1.08	0.024	0.022
8.409-9.760	9.062	0.74	0.019	0.015
9.760-11.33	10.518	0.54	0.015	0.011
11.33-13.15	12.202	0.39	0.012	0.008
13.15-15.26	14.173	0.28	0.009	0.006
11.327-13.146	12.202	0.39	0.012	0.008
13.146-15.258	14.173	0.28	0.009	0.006
15.258-17.708	16.472	0.20	0.007	0.004
17.708-20.552	19.107	0.14	0.006	0.003

Table 5.6: Summary of negative muon flux

Momentum range (GeV/c)	Mean momentum (GeV/c)	μ^- flux ($m^{-2}sr^{-1}s^{-1}(GeV/c)^{-1}$)	Statistical error	Systematic error
0.576-0.669	0.623	15.35	0.367	0.572
0.669-0.776	0.724	14.70	0.322	0.464
0.776-0.901	0.840	13.90	0.284	0.383
0.901-1.045	0.975	12.71	0.248	0.315
1.045-1.213	1.132	11.95	0.220	0.270
1.213-1.408	1.313	10.23	0.188	0.216
1.408-1.634	1.522	8.97	0.162	0.178
1.634-1.896	1.765	8.00	0.141	0.151
1.896-2.201	2.048	6.72	0.120	0.121
2.201-2.555	2.378	5.55	0.101	0.096
2.555-2.965	2.761	4.72	0.086	0.079
2.965-3.441	3.199	3.89	0.073	0.064
3.441-3.993	3.710	3.11	0.060	0.050
3.993-4.635	4.308	2.43	0.049	0.039
4.635-5.379	4.998	1.89	0.040	0.030
5.379-6.243	5.806	1.41	0.032	0.022
6.243-7.246	6.743	1.08	0.026	0.017
7.246-8.409	7.814	0.80	0.021	0.013
8.409-9.760	9.061	0.59	0.017	0.010
9.760-11.33	10.513	0.41	0.013	0.007
11.33-13.15	12.191	0.29	0.010	0.005
13.15-15.26	14.183	0.22	0.008	0.004
11.327-13.146	12.191	0.29	0.010	0.005
13.146-15.258	14.183	0.22	0.008	0.004
15.258-17.708	16.400	0.16	0.006	0.003
17.708-20.552	19.050	0.01	0.005	0.002

Chapter 6

Discussion

We obtained the muon momentum spectra and μ^+/μ^- charge ratios at three different geomagnetic locations at the ground level. These locations are (i) Lynn Lake, Manitoba, Canada from 1997 to 1999, at an altitude of 360 m above sea level with vertical geomagnetic cut-off rigidity of 0.4 GV, hereafter called BESS-1997/98/99, (ii) Ft. Sumner, New Mexico in 2001, at an altitude of 1270 m with a cut-off rigidity of 4.2 GV, hereafter called BESS-2001, and (iii) Tsukuba, Japan in 1995, at an altitude of 30 m with a cut-off rigidity of 11.4 GV, hereafter called BESS-1995. The experimental conditions from (i) to (iii) are summarized in Table 6.1.

Because of the geomagnetic field, there is a cut-off rigidity, R_c, for each location on the earth. Variations of the muon fluxes and μ^+/μ^- charge ratio with geomagnetic latitude are expected in the low momentum region. In addition there is a "solar modulation effect" caused by the solar activity to the primary cosmic-ray fluxes, and an "altitude effect" caused by altitude dependence of the column profile of the atmosphere. In order to discuss quantitatively a "geomagnetic latitude effect", we estimate solar activity and altitude dependences to the observed muon flux.

Figure 6.1 shows the absolute fluxes of atmospheric positive and negative muons observed in this work with previous observations using the BESS detector. The flux of BESS-2001 (Ft. Sumner) is higher than that of BESS-1997/98/99 (LynnLake) and BESS-1995 (Tsukuba) around 1 GeV/c, because BESS-2001 (Ft. Sumner) was performed at about 1000 m higher than the other locations.

Comparing with the fluxes of BESS-1995 at Tsukuba and BESS-1999 at Mt.Norikura(see Table 6.1), BESS-1999 is higher than BESS-1995. Both experiments were performed at almost the same geomagnetic cut-off rigidities, but different altitude. Thus the flux of BESS-1995 (Tsukuba) is lower than that of BESS-1999 (Mt. Norikura) by the decay and ionization loss of muons. In the next section, we discuss more details of the difference of fluxes by the change of the observed altitude.

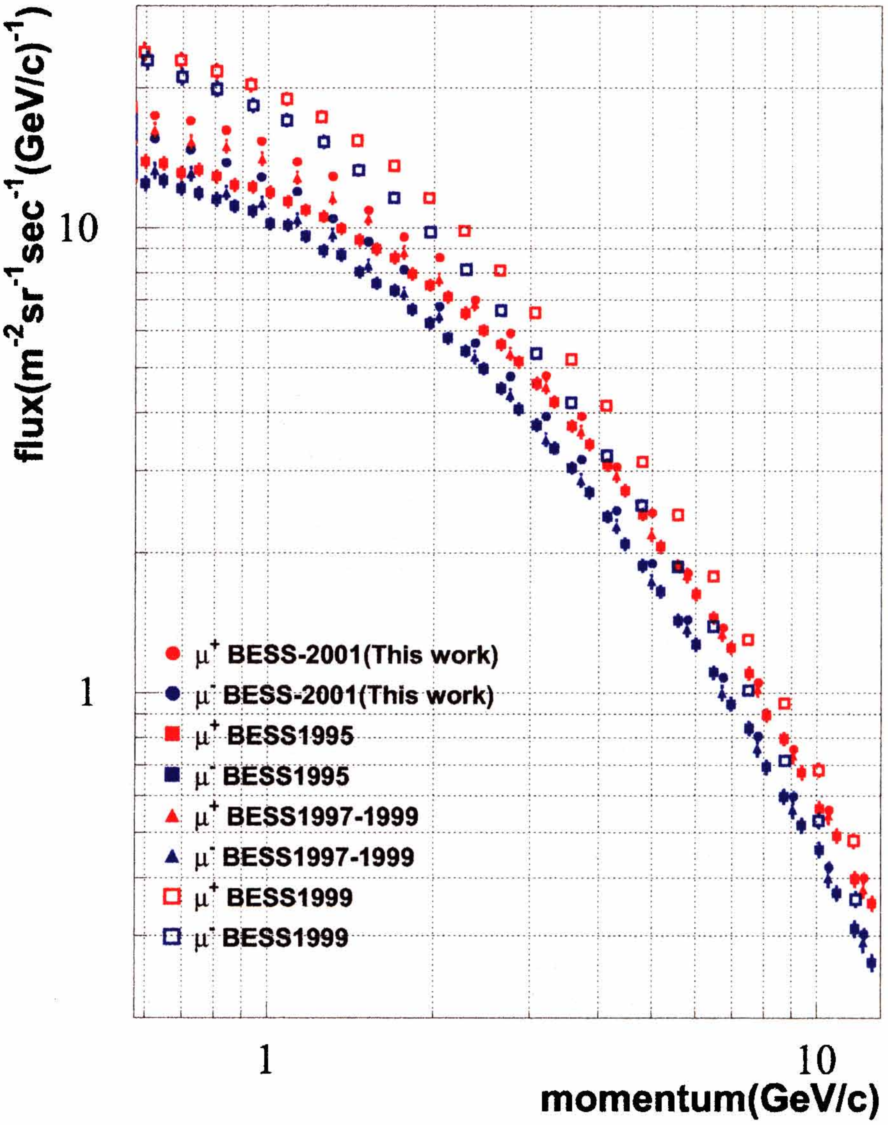

Figure 6.1: The absolute fluxes of atmospheric positive and negative muons in this work with previous observations using BESS detector. Each fluxes represent BESS-2001 at Ft. Sumner(4.2 GV), BESS-1995 at Tsukuba(11.4 GV), BESS-1997-1999 at LynnLake(0.5 GV), BESS-1999 at Mt. Norikura(11.2 GV).

Table 6.1: Summary of some locational conditions about previous experiments.

Location	**Date**	**Observed time** (hours)	**Altitude** (m)	**Atmospheric depth** (g/cm^2)	**Geomagnetic cut off** (GV)
(ii)Ft.Sumner NewMexico (**BESS-2001**)	2001	4	1270	892	4.2
(i)LynnLake Manitoba Canada (**BESS-1997/98/99**)	1997 1998 1999	2 2 2	360	998	0.4
(iii)Tsukuba Japan (**BESS-1995**)	1995	81	30	1030	11.4
Mt.Norikura Japan (**BESS-1999**)	1999	96	2770	742	11.2

6.1 Altitude correction

In order to compare the fluxes of BESS-2001 (Ft. Sumner), BESS-1997/98/99 (LynnLake) and BESS-1995 (Tsukuba), the flux of BESS-2001 (Ft. Sumner) is to be corrected for an altitude. In altitude correction for muon fluxes, we considered the following three factors for the change of the flux of muons;

(1) Decay of muons between the two different altitudes.
(2) Ionization loss.
(3) Production of muons between the two altitudes.

At first, we verified the method of altitude correction using the muon fluxes of BESS-1995 (Tsukuba) and BESS-1999 (Mt. Norikura). BESS-1995 (Tsukuba) and BESS-1999 (Mt. Norikura) were performed at almost same geomagnetic cut-off rigidities with different altitudes each other.

6.1.1 Ionization Loss and Decay of Muons

In order to compare the flux of BESS-1999 (Mt. Norikura) with the flux of BESS-1995 (Tsukuba), we need to consider the flux change between those two altitude via "decay" and "ionization loss" processes. The probability that muons at atmospheric depth x_1 g/cm^2 survive to the atmospheric depth x_2 g/cm^2 ($x_1 < x_2$) is called a "survival probability". The survival probability $\omega_{N \to T}$ of muons with "decay" and "ionization loss" from altitude at Mt. Norikura to altitude at Tsukuba is represented as follows (see **Appendix A**),

$$\omega_{N \to T} = \left(\frac{x_T}{x_N} \frac{P_N}{P_N - a(x_T - x_N)} \right)^{-\frac{b}{P_N + a \cdot x_N}} . \tag{6.1}$$

Here the parameters are defined in Table 6.2.

Table 6.2: Summary of variables used in survival probability ω.

Symbol	Definition	Units or Value
x_N	Pressure at Mt. Norikura	742 g/cm^2
x_T	Pressure at Tsukuba	1030 g/cm^2
P_N	Momentum at Mt. Norikura	GeV/c
a	Ionization loss rate	$\frac{GeV/c}{g/cm^2}$
b	Decay probability	GeV/c

Ionization loss rate a means that charged particles lose their momenta in the air by ionization and atomic excitation. The mean rate of momentum loss was given by the *Bethe-Bloch* equation [46] [47].

Decay probability b is calculated as (see more details in **Appendix A**);

$$\begin{aligned}
b &= \frac{mh}{\tau} \qquad (m: Muon\ mass,\ \tau: Life\ time\ of\ muon,\ h: Scale\ height) \\
&= \frac{m}{\tau} \cdot \frac{x_N}{\rho_N} \qquad \left(h = \frac{x_N}{\rho_N}\right) \\
&= \frac{m}{\tau} \cdot \frac{k \cdot N_A \cdot T_N}{g \cdot M} \times 10^5 \qquad \left(\rho = \frac{x_N \cdot g \cdot M}{k \cdot N_A \cdot T_N} \times 10^{-5}\right). \\
&= 1.3347 \ (GeV/c),
\end{aligned} \tag{6.2}$$

where the parameters are defined as described in Table 6.3.

Table 6.3: Summary of variables used in decay probability b.

Symbol	Definition	Units or Value
m	Muon mass	0.105658 GeV
h	Scale height	8320.56 m
τ	Muon life time	2.197×10^{-6} sec
ρ_N	Atmospheric density	g/cm^3
k	Boltzmann constant	1.380662×10^{-23} J $\cdot$ K^{-1}
N_A	Avogadro constant	6.022045×10^{23} mol^{-1}
T_N	Temperature at Mt. Norikura	284.05 K
g	Gravitational acceleration	9.797887 m/sec^2
M	Molecular weight of air	28.96974 g/mol

Molecular weight of air M is given by the atmospheric composition, which is considered to be consists of nitrogen(78 %), oxygen(21 %), argon(1 %) [45]. Decay constant b of muons was calculated from atmospheric depth of 742 g/cm^2 at Mt. Norikura to that of 1030 g/cm^2 at Tsukuba, assuming that an atmospheric composition and temperature are constant.

Figure 6.2 shows the obtained survival probability between the mountain altitude and the sea level as a function of momentum.

By using $\omega_{N \to T}$, the muon spectra at Tsukuba altitude, $flux_{N \to T}$, was estimated from those at Mt. Norikura, $flux_N$, as follows;

$$flux_{N \to T} = \omega_{N \to T} \times flux_N, \tag{6.3}$$

Figure 6.3 schematically shows the method of altitude correction with decay and ionization loss. The BESS-1999 (Mt. Norikura) of positive muon flux at Mt. Norikura was shifted in the direction of low momentum by the ionization, and also the flux is reduced by the decay processes.

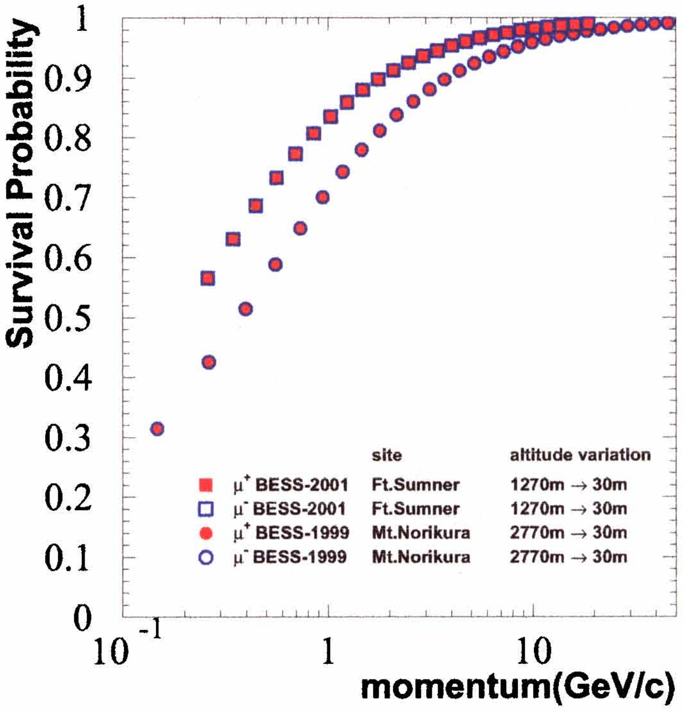

Figure 6.2: The survival probability of positive and negative muons as a function of momentum calculated by the formula 6.1, 6.4. (Circle)The probability that muons at Mt.Norikura altitude(2770m) survive until Tsukuba altitude(30m). (Square)The probability that muons at Ft.Sumner altitude(1270m) survive until Tsukuba altitude(30m).

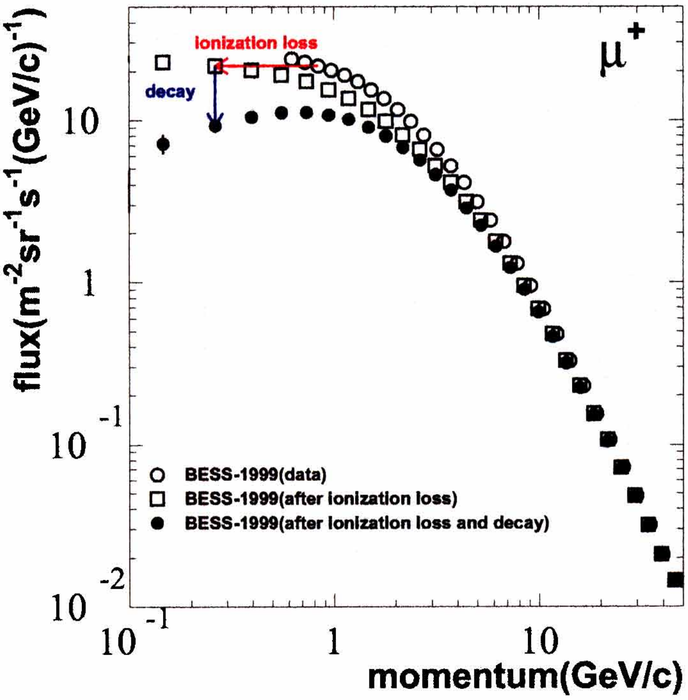

Figure 6.3: The method of altitude correction for decay and ionization loss of muons. For example, using the positive muon flux of BESS-1999 (Mt. Norikura), the positive muon flux at Tsukuba altitude(30 m) is calculated with ionization loss and decay.

6.1.2 Production of Muons

In order to estimate the muons production between an altitude of Mt. Norikura and Tsukuba, we made a Monte Carlo simulation for cosmic-ray transport inside the atmosphere based on GEANT [64] [65] [66]. GEANT is a tool of Monte Carlo simulation used frequently in the field of the high energy physics and allows us to simulate phenomena in an easy way.

We used the atmospheric density by the MSIS-E-90 Atmosphere Model [48] [49] [50] [51]. The MSIS-E-90 Atmosphere Model is an empirical model based on the data measured by seven satellites and numerous rocket probes. This model provides the atmospheric temperature and the atmospheric density at any place and at any time. Figure 6.4 shows the profile of the atmospheric density in 1999 between an altitude of Mt. Norikura(2770 m) and Tsukuba(30 m).

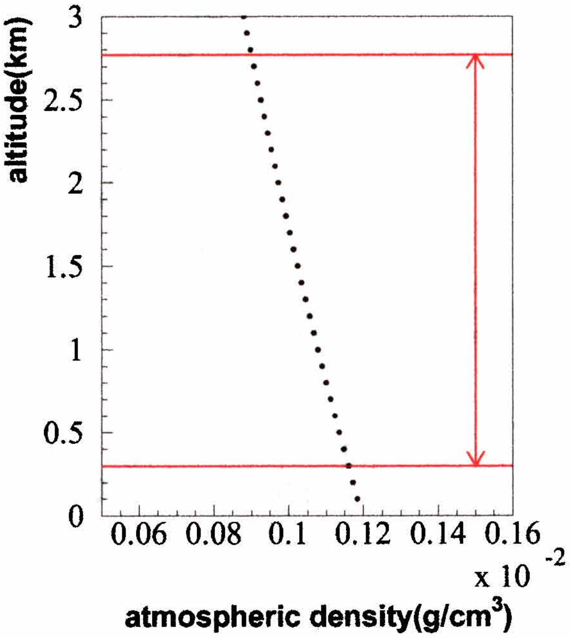

Figure 6.4: Atmospheric density profile at each altitude used for the simulation. The data from MSIS-E-90 model is calculated for the altitude between 0.0 and 3.0 km. (Red arrow)The altitude region as an atmospheric profile is used for Monte Carlo simulation.

As a hadronic interaction model, we used FLUKA [66] equipped in GEANT. Parent protons and neutrons were injected into the air vertically varying the kinetic energy in the range of 0.12 through 1200 GeV randomly in logarithmic scale. In the analysis of the simulation data, we multiplied the energy distribution of parent protons by the proton spectrum observed at Mt. Norikura in

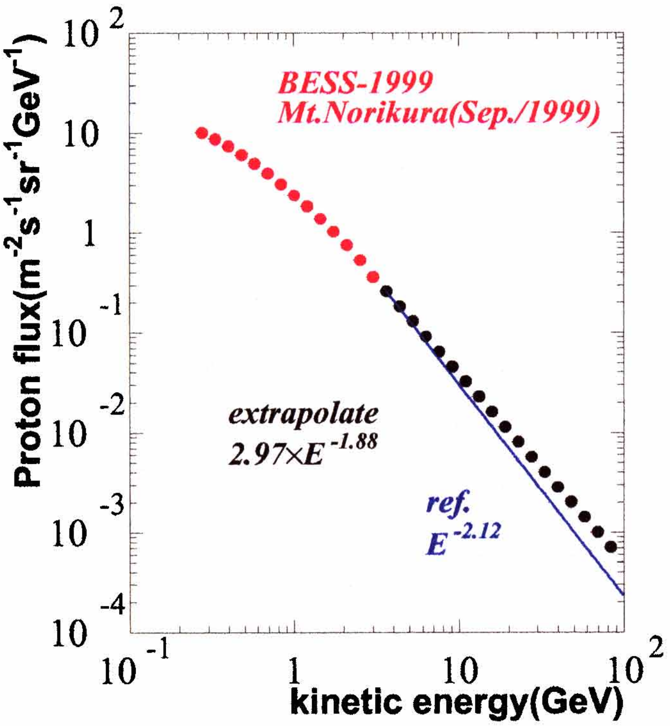

Figure 6.5: The proton spectrum observed at Mt. Norikura in 1999 by BESS detector [52]. Above 3.31 GeV in the kinetic energy, the proton spectrum was extrapolated as a power law as $2.97 \times E^{-1.88}$. The proton spectrum of previous experiments shows as a power law as $E^{-2.12}$ in [53] [54] [55] [56].

1999 by the BESS detector [52]. The observed spectrum covers the kinetic energy range of 0.25-3.31 GeV. The proton spectrum above 3.31 GeV in the kinetic energy was extrapolated as a power law as $E^{-1.88}$ in Figure 6.5.

The previous experiments reported that the proton spectrum at 3200 m a.s.l. had steeper index as a power law as $\sim 4 \times 10^{-4} \times E^{-2.12}$ $cm^{-2}s^{-1}sr^{-1}GeV^{-1}$ above 10 GeV [53] [54] [55] [56]. In the Monte Carlo simulation, we used the proton spectrum as a power law as $E^{-1.88}$ above 3.31 GeV extrapolated from the proton spectrum at Mt. Norikura, and observed proton at Mt. Norikura in the kinetic energy range of 0.25 through 3.31 GeV. We estimated that the proton spetrum at Mt. Norikura is larger than that of previous experiments in high energy region.

For the muon production from neutron, we used the neutron spectrum as a power law as $\sim 4 \times 10^{-7} \times E^{-3}$ $cm^{-2}s^{-1}sr^{-1}MeV^{-1}$ above 1 GeV observed at Matterhorn Lab., Italy, 3500 m a.s.l.(650 g/cm^2) [57]. The neutron spectrum has a steeper shape than proton spectrum. The absolute flux of protons and neutrons are almost same at 1 GeV.

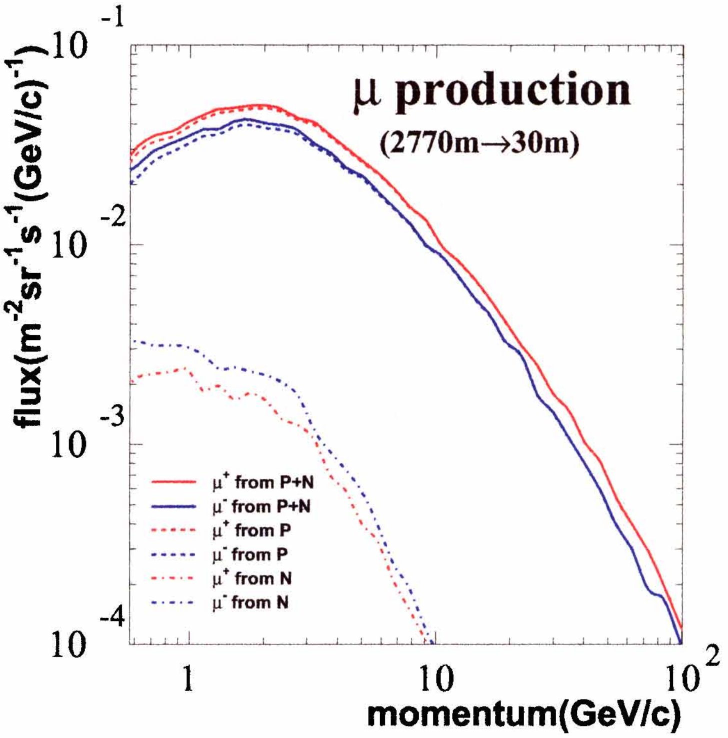

Figure 6.6: The muon production between altitude of Mt. Norikura and Tsukuba using proton and neutron spectrum assumed at Mt. Norikura.

Figure 6.6 shows the simulated positive and negative muon spectra at Tsukuba altitude(30 m), which are produced between mountain altitude and the sea level. Since the index of proton spectrum is looser than that of neutron spectrum, the number of muons produced from protons is larger than that from neutrons.

The muon production between Mt. Norikura altitude and Tsukuba altitude is less than 1 % even if protons and neutrons spectra are estimated larger than spectra of previous experiments.

6.1.3 Altitude correction for BESS-1999 (Mt. Norikura)

As discussed in Section 6.1.2, the number of muons producted between the altitude of Mt. Norikura and Tsukuba is negligible. Thus, in altitude correction, from Section 6.1.1, the muon spectra at Tsukuba estimated from the muon spectra at Mt. Norikura shuld be corrected for "decay" and "ionization loss" of muons.

Figure 6.7 shows the muon spectra of BESS-1999 at Tsukuba altitude(30 m) after altitude correction together with BESS-1995 (Tsukuba) and BESS-1999 (Mt. Norikura). Above 2 GeV/*c*, BESS-1999 (Mt. Norikura) after altitude correction and BESS-1995 (Tsukuba) are consistent with each other. Around 1 GeV/*c*, the difference between BESS-1999 (Mt. Norikura) after altitude correction and BESS-1995 (Tsukuba) is about 10 %. Since the observation time is different, it could be suggested that solar modulation and atmospheric structure at different observation time is reflected in low momentum region.

In the next Section 6.1.4, the same method of altitude correction is applied to positve and negative muon spectra in BESS-2001 (Ft. Sumner).

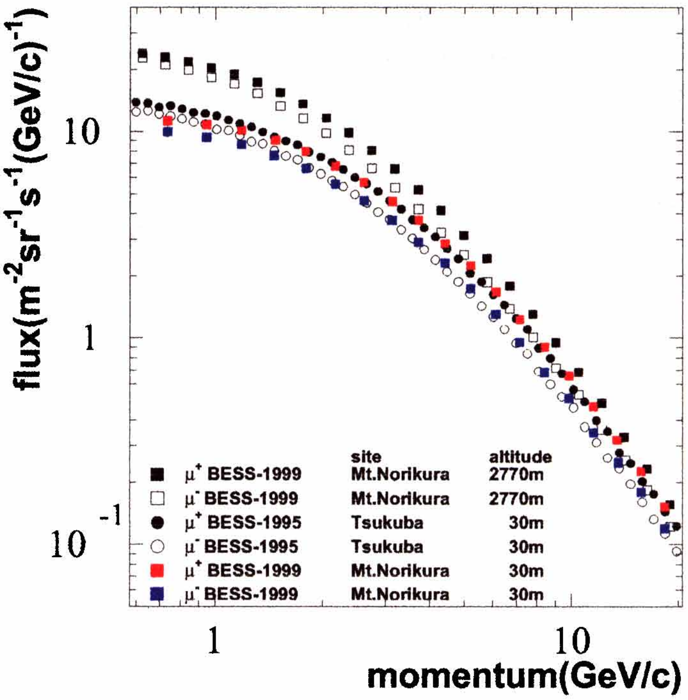

Figure 6.7: The positive and negative muon spectra as a momentum function of BESS-1999 (Mt. Norikura) after alititude correction, BESS-1999 (Mt. Norikura) and BESS-1995 (Tsukuba). (Red and Blue squares)The positive and negative muon spectra at Tsukuba altitude (30 m) estimated from Mt. Norikura altitude (2770 m).

6.1.4 Altitude correction for BESS-2001 (Ft. Sumner) and BESS-1997/98/99 (LynnLake)

BESS-2001 (Ft. Sumner) and BESS-1997/98/99 (LynnLake) were also corrected for altitude in the same manner as described in Section 6.1.1, those are "decay" and "ionization loss" for muons. Since the altitude at Ft. Sumner and LynnLake are lower than the altitude at Mt. Norikura, muons production between an altitude at Ft. Sumner(1270 m) or LynnLake(360 m) and Tsukuba(30 m) is less significant. From the equation 6.1, the survival probability $\omega_{F\to T}$ and $\omega_{L\to T}$ of muons with "decay" and "ionization loss" from altitude at Ft. Sumner(1270 m) and LynnLake(360 m) to altitude at Tsukuba(30 m) is represented as follows(see **Appendix A**), respectively,

$$\omega_{F\to T} = \left(\frac{x_T}{x_F}\frac{P_F}{P_F - a(x_T - x_F)}\right)^{-\frac{b_F}{P_F + a\cdot x_F}}. \tag{6.4}$$

$$\omega_{L\to T} = \left(\frac{x_T}{x_L}\frac{P_L}{P_L - a(x_T - x_L)}\right)^{-\frac{b_L}{P_L + a\cdot x_L}}. \tag{6.5}$$

Here the x_F and x_L are pressures at Ft. Sumner of 892 g/cm^2 and at LynnLake of 998 g/cm^2. P_F and P_L are momenta at Ft. Sumner and at LynnLake.

Decay constant b_F and b_L are (see **Appendix A**),

$$b_F = \frac{m}{\tau}\cdot\frac{k\cdot N_A\cdot T_F}{g\cdot M}\times 10^5 = 1.4010\ (GeV/c)$$

$$b_L = \frac{m}{\tau}\cdot\frac{k\cdot N_A\cdot T_L}{g\cdot M}\times 10^5 = 1.3554\ (GeV/c)$$

T_F and T_L are observed atmospheric temperature of 304.15 K at Ft. Sumner and 288.45 K at LynnLake, respectively. Decay constant b_F of muons was calculated from atmospheric depth 892 g/cm^2 at Ft. Sumner to 1030 g/cm^2 at Tsukuba, assuming that an atmospheric component and temperature are constant. Also decay constant b_L, it was calculated by the same method as b_F. Figure 6.2 shows the survival probability that muons at Ft. Sumner altitude(1270 m) survive to Tsukuba altitude(30 m).

Figure 6.8 show the positive and negative muon momentum spectra of BESS-2001 (Ft. Sumner) after altitude correction(30 m a.s.l.) and BESS-2001(1270 m a.s.l.) in top figure, and BESS-1997/98/99 (LynnLake) after altitude correction(30 m a.s.l) and BESS-1997/98/99(360 m a.s.l) in bottom figure. Beyond 10 GeV/c in momentum, there is no change of muon spectra after and before altitude correction. Around 1 GeV/c in momentum, the muon spectra of BESS-2001 after altitude correction was 30 % lower than that of BESS-2001 (Ft. Sumner).

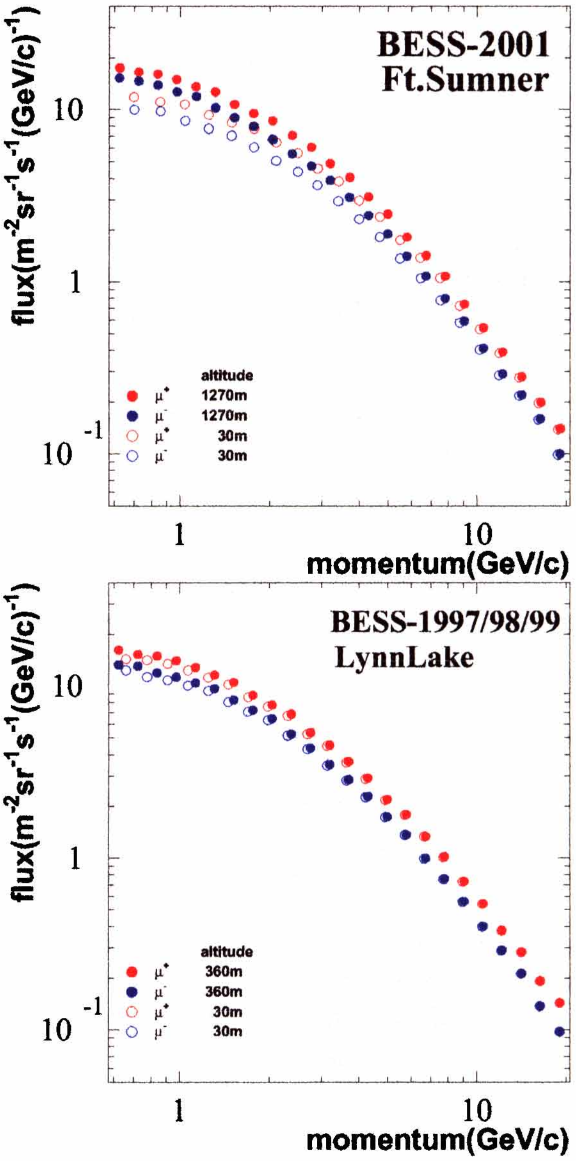

Figure 6.8: The positive and negative muon spectra as a momentum function of (top)BESS-2001 after altitude correction and BESS-2001 at Ft. Sumner, (bottom)BESS-1997/98/99 after altitude correction and BESS-1997/98/99 at LynnLake.

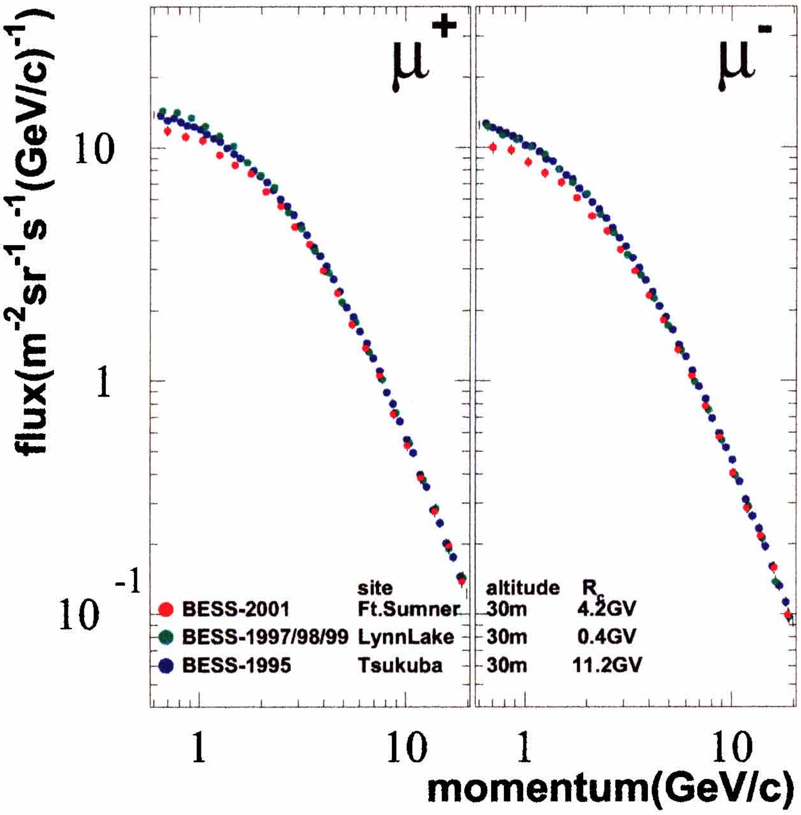

Figure 6.9: The positive and negative muon spectra of BESS-2001 (Ft. Sumner) and BESS-1997/98/99 (LynnLake) after altitude correction, and BESS-1995 (Tsukuba).

6.2 Solar activity dependence

Figure 6.9 shows the positive and negative muon spectra of BESS-2001 (Ft. Sumner) and BESS-1997/98/99 (LynnLake) after altitude correction, and BESS-1995 (Tsukuba). In spite of having corrected altitude for the positive and negative muon spectra of BESS-2001 (Ft. Sumner), the muon spectra of BESS-2001 after altitude correction (black color) is lower than that of BESS-1995 (Tsukuba, blue color) at highest geomagnetic cut-off rigidity of the three locations in Figure 6.9. Since the measurement years are different each other, the muon spectra have influence of "solar modulation effect".

The solar activity influences the cosmic-ray flux on the earth and affect to the shape of the energy spectrum up to about 100 GeV/nucleon [58]. The galactic or primary cosmic-ray and consequently the secondary cosmic-ray produced in the atmosphere, are subject to a periodic variation that follows

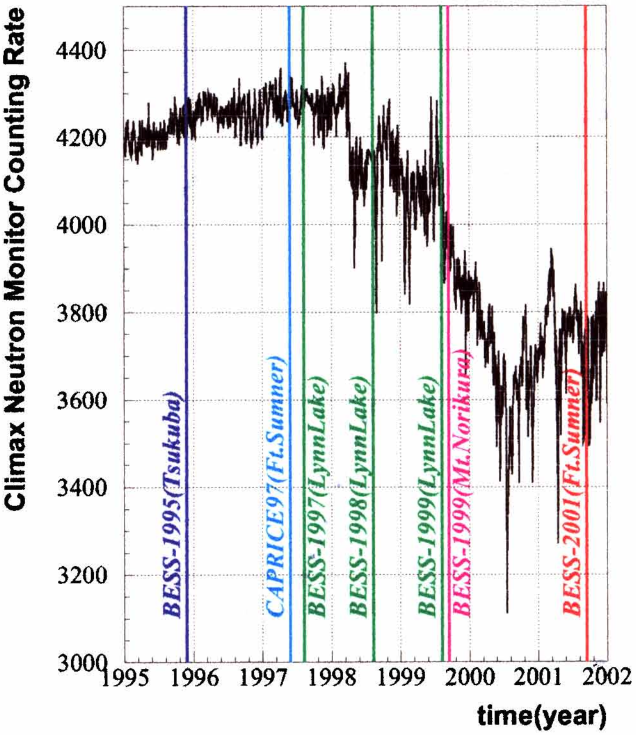

Figure 6.10: The variety of neutron counting rate by solar modulation effect. [63]

the 11 year solar cycle.

Figure 6.10 shows the solar modulation cycles by the variation of neutron counting rate by CLIMAX neutron monitor of The University of Chicago [63] with geomagnetic cut-off rigidity of 2.99 GV. The solar activity was minimal in 1996 (solar minimum) and maximal in 2000 (solar maximum) in the past 10 years.

Figure 6.11 shows the variety of primary proton fluxes at balloon altitude from 1997 to 2001 using the BESS detector in kinetic energy range 4 - 20 GeV. The BESS experiment performed at LynnLake from 1997 to 2000, at Ft.Sumner in 2001, at an altitude of ~ 36 km above sea level (~ 5 g/cm^2). The primary proton fluxes decrease as solar activity become maximum. Primary proton flux in BESS2000 at solar maximum is lower than fluxes in BESS1997, BESS1998, BESS1999, and BESS2001. Primary cosmic ray is affected by solar activity. The atomospheric muons arrive at the ground with the information of the solar modulation. The observed muons in momentum range 0.5 - 20 GeV/c are contributed from the protons in kinetic energy range 20 - 200 GeV [59]. Thus, the fluxes on ground level are indirectly reflected the fluxes of primary cosmic ray.

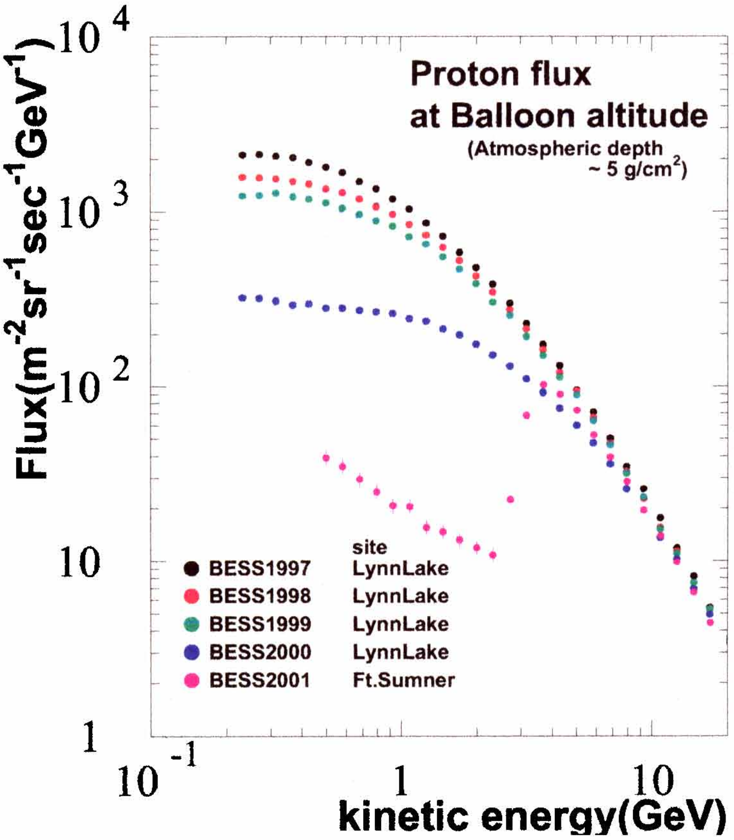

Figure 6.11: The variety of primary proton fluxes at balloon altitude from 1997 to 2001 using BESS detector in kinetic energy range 4 - 20 GeV. BESS experiment performed at LynnLake, Nothern Canada from 1997 to 2000, at Ft.Sumner, NewMexico in 2001.

BESS-2001 (Ft. Sumner) was performed near the solar maximum, while BESS-1995 (Tsukuba) and BESS-1997/98/99 (LynnLake) were performed near the solar minimum. Comparing with BESS-2001 (Ft. Sumner), BESS-1995 (Tsukuba) and BESS-1997/98/99 (LynnLake) about a geomagnetic latitude, it is necessary to eliminate the solar modulation effect.

In order to estimate the solar acivity dependence, BESS-2001 (Ft. Sumner) obtained by this analysis is compared with CAPRICE97. Both observations were carried out on the ground at Ft. Sumner at a different year. Figure 6.12 and Figure 6.13 show the absolute differential momentum spectra of the positive and negative muons, and the positive to negative charge ratios on the ground at Ft. Sumner, respectively. In momentum spectra as shown in Figure 6.12, in comparing with CAPRICE97, the difference is as

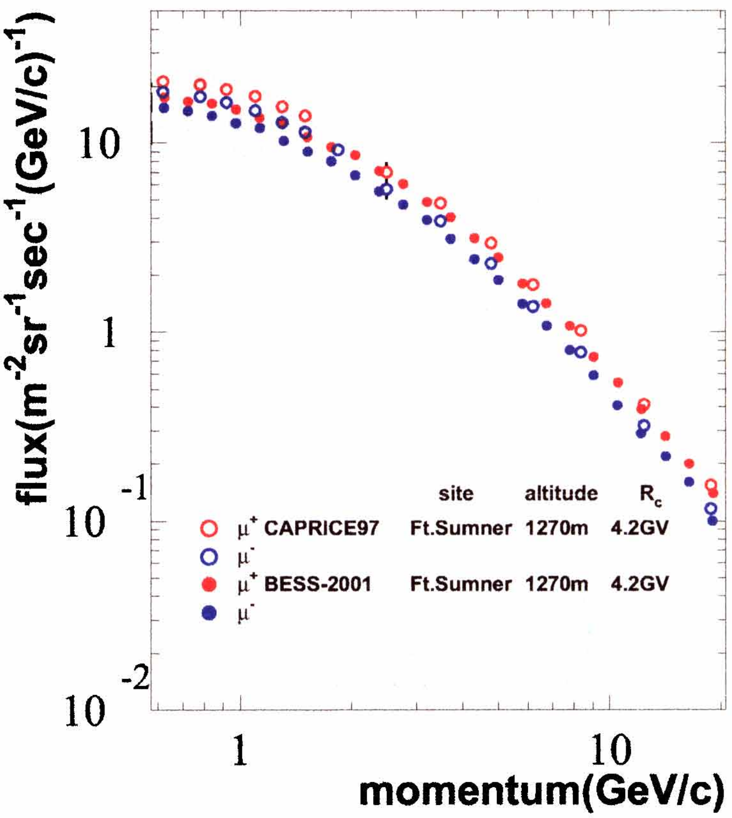

Figure 6.12: The absolute differential momentum spectra of the positive and negative muons on the ground at Ft. Sumner. (opened circle)CAPRICE97, (closed circle)BESS-2001.

large as about 15 % around 1 GeV/c. The difference is attributed to the effect of solar modulation and the different of zenith angle regions in fiducial volume. On the other hand, in charge ratios as shown in Figure 6.13, the difference between BESS-2001 (Ft. Sumner) and CAPRICE97 is small. Figure 6.14 shows the ratio of charge ratio in CAPRICE97 to charge ratio in BESS-2001 (Ft. Sumner). The difference between BESS-2001 (Ft. Sumner) and CAPRICE97 is as small as within ± 3 % by linear function fitting in momentum range 0.6 - 20 GeV/c.

Thus, taking charge ratio, the solar modulation does not affect to the charge ratio so large as to the momentum spectra. We will discuss geomagnetical latitude dependence of the charge ratio of μ^+/μ^-.

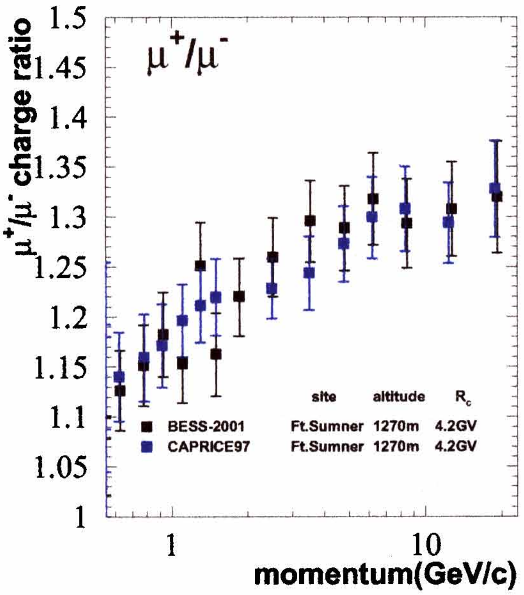

Figure 6.13: The μ^+/μ^- positive to negative charge ratios on the ground at Ft. Sumner. (blue)CAPRICE97, (black)BESS-2001

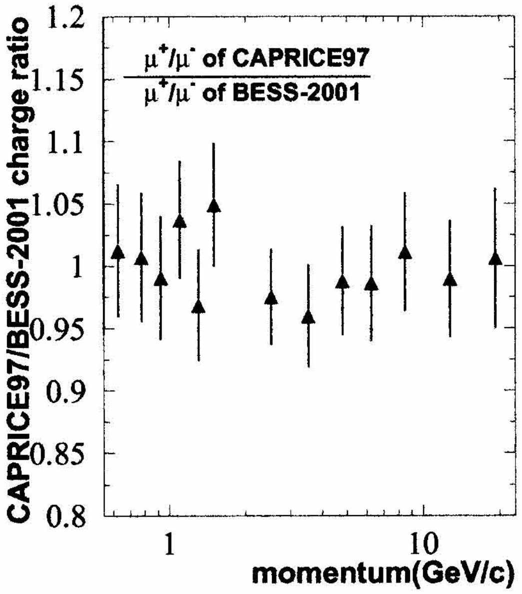

Figure 6.14: The ratio of μ^+/μ^- charge ratio in CAPRICE97 to charge ratio in BESS-2001.

6.3 Geomagnetic latitude effect on charge ratio of muons

In order to estimate the geomagnetic latitude dependence, we use the data obtained from BESS-2001 (Ft. Sumner), BESS-1995 (Tsukuba) and BESS-1997/98/99 (LynnLake) at three different geomagnetic lacations. These experiments are performed in different years and at different altitudes. It is for the first time that atmospheric muon spectra were measured precisely at different locations and periods using same detector. From the discussions of Section 6.2, it becomes clear that in comparing with the fluxes of BESS-2001 (Ft. Sumner), BESS-1995 (Tsukuba) and BESS-1997/98/99 (LynnLake), it is necessary to correct the effect of solar modulation. Comparing with the charge ratios, however, the dependence of solar modulation is negligibly small. The geomagnetic latitude effect of the muon charge ratios is discussed in this section.

Figure 6.15 shows the positive and negative charge ratios of BESS-2001 (Ft. Sumner) and BESS-1997/98/99 (LynnLake) after altitude correction, and BESS-2001 (Ft. Sumner) and BESS-1997/98/99 (LynnLake) before altitude correction, and BESS-1995 (Tsukuba). The following three points were considered from the figure 6.15.

(i) The charge ratios of BESS-2001 (Ft. Sumner) and BESS-1997/98/99 (LynnLake) around 1 GeV/c.

Comparing with before and after altitude correction of BESS-2001 (Ft. Sumner), the charge ratio after altitude correction of BESS-2001 (Ft. Sumner) is higher than that before altitude correction around 1 GeV/*c*. The charge ratio after altitude correction of BESS-2001 (Ft. Sumner) is closed to the charge ratio of BESS-1997/98/99 (LynnLake).

(ii) The charge ratios of BESS-2001 (Ft. Sumner) (or BESS-1997/98/99 (LynnLake)) and BESS-1995 (Tsukuba) around 1 GeV/c.

Comparing with BESS-2001 (Ft. Sumner) after altitude correction and BESS-1995 (Tsukuba), the difference is as large as about 6 % around 1 GeV/c. Comparing with BESS-1997/98/99 (LynnLake) after altitude correction and BESS-1995 (Tsukuba), the difference is as large as about 10 % around 1 GeV/c. The difference from geomagnetic latitude effect is appeared between BESS-2001 (Ft. Sumner) (or BESS-1997/98/99 (LynnLake)) and BESS-1995 (Tsukuba).

(iii) The charge ratios of BESS-2001 (Ft. Sumner), BESS-1997/98/99 (LynnLake) and BESS-1995 (Tsukuba) around 10 GeV/c.

Comparing with BESS-2001 (Ft. Sumner), BESS-1997/98/99 (LynnLake) and BESS-1995 (Tsukuba), the charge ratios of the three locations are

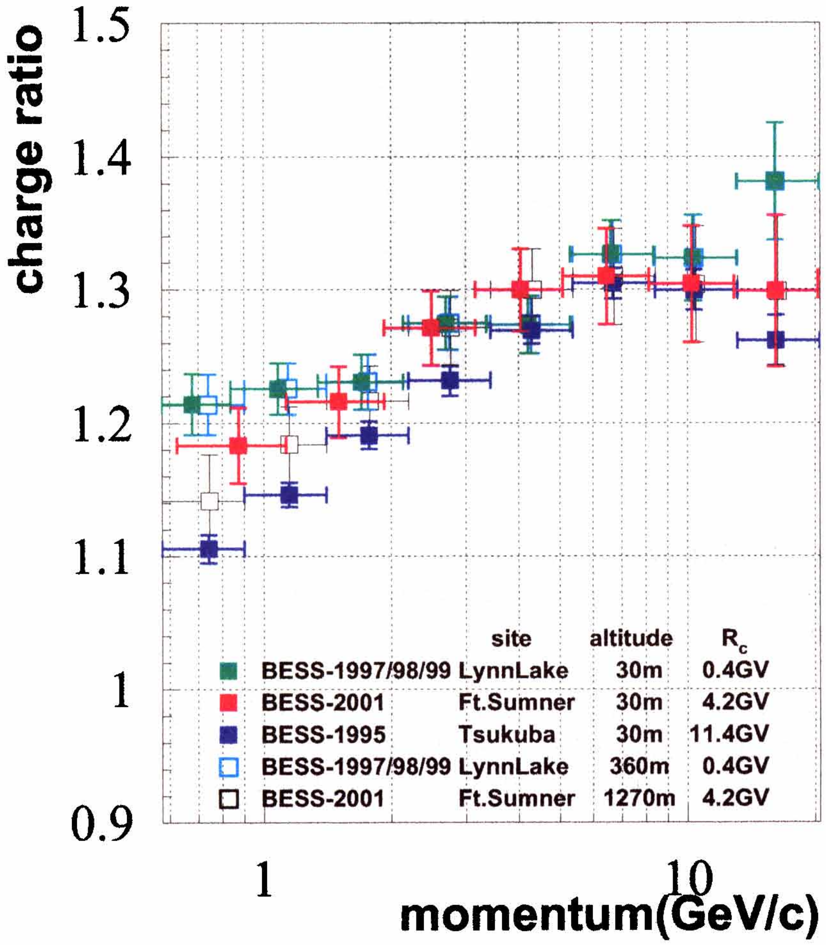

Figure 6.15: The positive to negative charge ratios of BESS-2001 after altitude correction, BESS-2001 (Ft. Sumner), BESS-1997/98/99 (LynnLake) and BESS-1995 (Tsukuba).

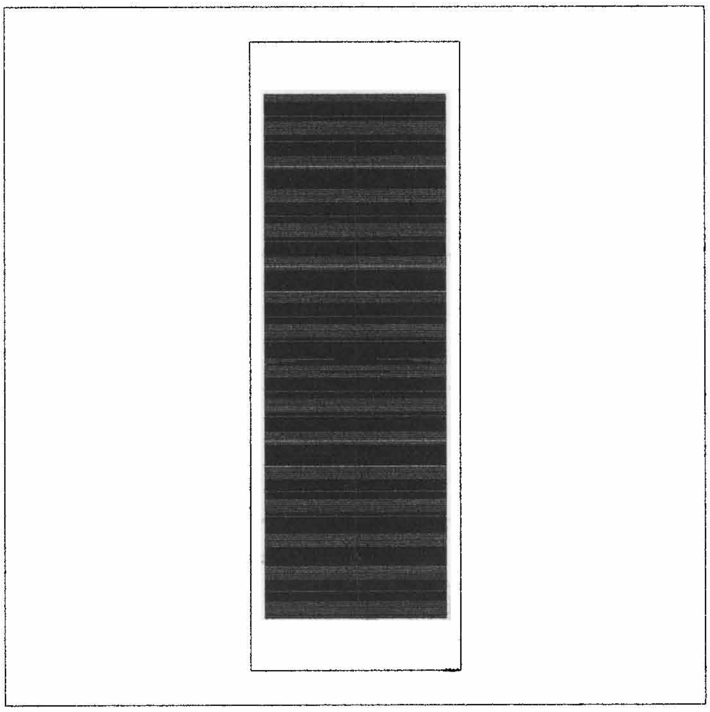

Figure 6.16: Event display of the simulation of the shower from a proton with 80 GeV using GEANT-FLUKA. Red lines show protons or pions. Green lines show muons.

in agreement around 10 GeV/c. No difference from geomagnetic latitude effect is appeared between BESS-2001 (Ft. Sumner) (or BESS-1997/98/99 (LynnLake)) and BESS-1995 (Tsukuba).

This reason is explained by figure 6.18 which show the correlation between parent proton energy and muon momenta on the ground. This calculation is based on Monte Carlo simulation for the atmospheric muons in Section 6.1.2. Figure 6.16 shows a typical event display of the simulation for proton with 80 GeV. The air was defined as a cylindrical volume whose height is 100 km and radius is 17 km. The atmospheric density is given every 100 km along the height. We used the atmospheric density data measured in BESS experiments for the altitude below 38 km. Above 38 km, on the other hand, we used the MSIS-E-90 model. Figure 6.17 shows the profile of the atmospheric density in 1999 used in the simulation. As a hadronic interaction model, we used FLUKA equipped in GEANT. Parent protons were injected into the air vertically varing the kinetic energy in the range of 0.5 through 100 GeV randomly in logarithmic scale. For heavier primary cosmic rays, we employed the "superposition approximation" [67]. We treated a helium nucleus as two

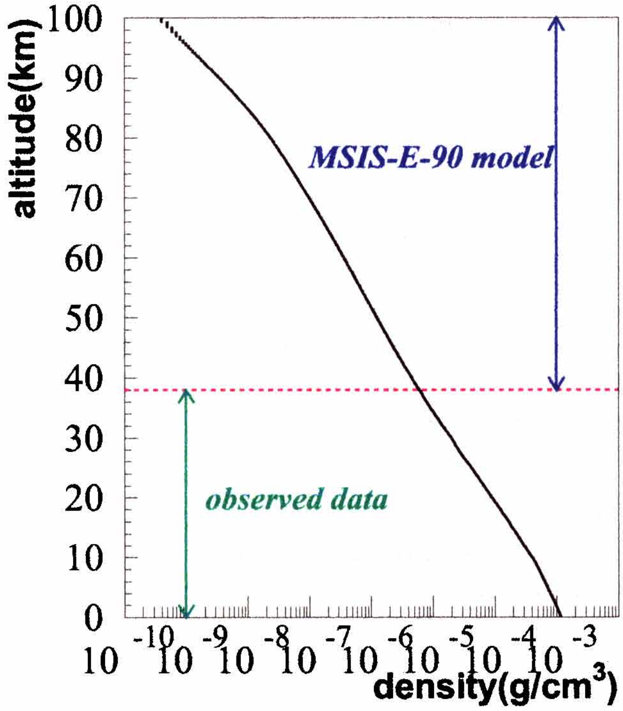

Figure 6.17: Atmospheric density profile for the simulation. The data from MSIS-E-90 model are used for the altitude higher than 38 km.

protons and two neutrons. Therefore, neutrons were also injected into the air vertically varing the kinetic energy in the range of 0.5 through 100 GeV randomly in logarithmic scale. In the analysis of the simulation data, we multiplied the energy distribution of parent protons by the primary proton spectra observed in BESS experiments. For helium, we multiplied the energy distribution of parent protons and neutrons by the primary helium spectra observed in BESS experiments. For heavier nuclei than helium, we multiplied helium spectrum by 1.418 by using the chemical abundances of cosmic rays [68] [69].

It is considered that the differences between observed and simulated muon fluxes originate from the simulation simplicity. For example, in the simulation, we did not consider the zenith angle distribution of primary cosmic rays, correct air structure and the existance of geomagnetic field. It is expected that the differeces between the observed spectra and the simulated spectra would be reduced, if we take these factors into consideration correctly.

We discuss the correlation between the muon momentum on the ground and the parent proton energy at top of atmosphere. Figure 6.18 shows the resluts of this simulation. About (i) $\sim$ (iii), we explain using the results of this simulation.

(i) The geomagnetic cut-off in kinetic energy show 0.07 GeV at LynnLake and 3.32 GeV at Ft. Sumner in figure 6.18. There is different geomagnetic cut-off rigidities of Ft. Sumner and LynnLake, however, geomagnetic latitude effect is not effective for primary proton in the kinetic energy range 0.07-3.32 GeV. Because muons arrived on the ground are originated primary cosmic rays above 3 GeV in Figure 6.18. Thus, comparing the charge ratios of LynnLake and Ft. Sumner at same altitude, the charge ratios of LynnLake and Ft. Sumner are consistent with each other.

(ii) Positive and negative muons in momentum range 0.6 - 0.9 GeV/c (region (a) in figure 6.18) is projected on X-axis ($E_{primary}$ in figure 6.18). Figure 6.19 shows $\mu^{\pm}$ contributed from primary cosmic rays in a muon momentum range 0.6 - 0.9 GeV/c. Since positive muons at Ft. Sumner and LynnLake are larger of green color hatch in figure 6.19 than that at Tsukuba, the μ^{+}/μ^{-} charge ratios at Ft. Sumner and LynnLake are larger than that at Tsukuba.

(iii) Positive and negative muons in momentum range 8.4 - 13.1 GeV/c (region (b) in figure 6.18) is projected on X-axis ($E_{primary}$ in figure 6.18). Figure 6.20 shows $\mu^{\pm}$ contributed from primary cosmic rays in a muon momentum range 8.4 - 13.1 GeV/c. Since positive and negative muons are arrived on the ground at Ft. Sumner, LynnLake and Tsukuba are common primary cosmic rays (green color hatch in figure 6.20), the μ^{+}/μ^{-} charge ratios at Ft. Sumner, LynnLake and Tsukuba become a constant value regardless of geomagnetic cut-off rigidities.

Geomagnetic latitude effect was able to be qualitatively explained by this simulation.

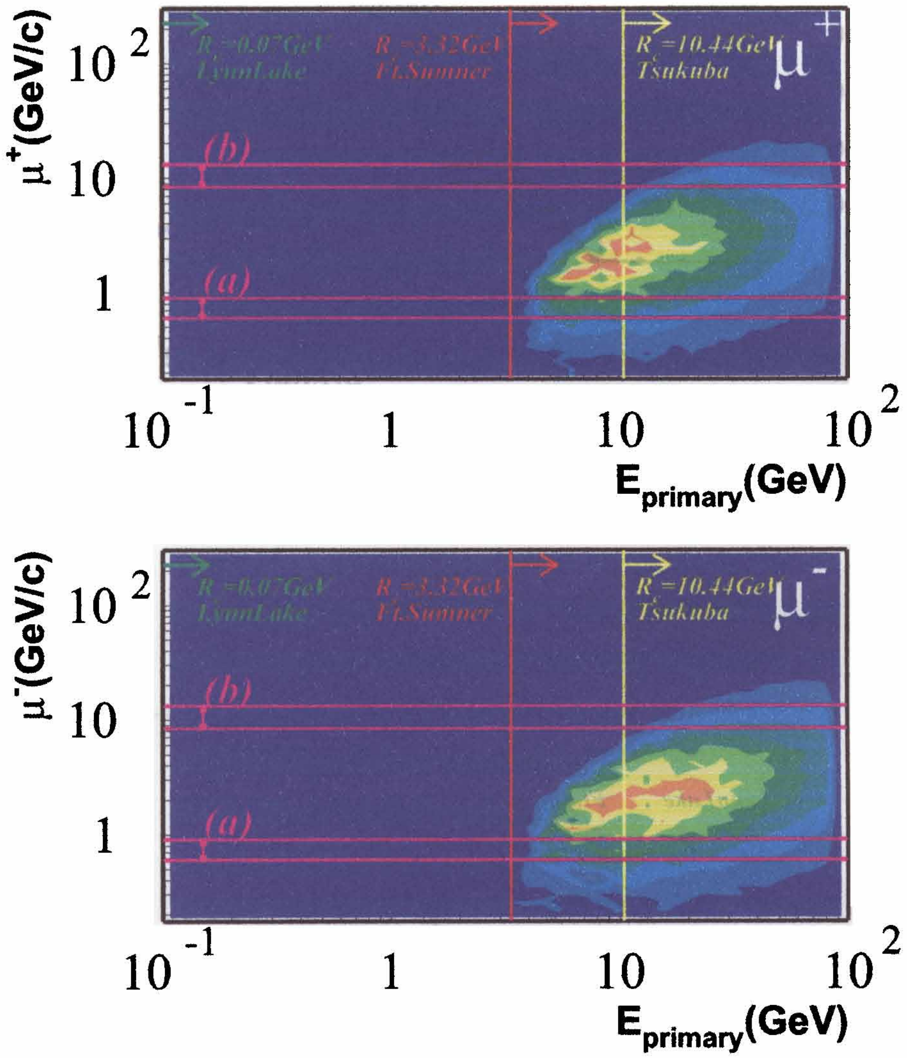

Figure 6.18: (Top) and (bottom) figures show the correlation between parent proton energy at atmospheric depth of 4.6 g/cm^3 in 1999 at LynnLake and positive and negative muon momenta on the ground, respectively.

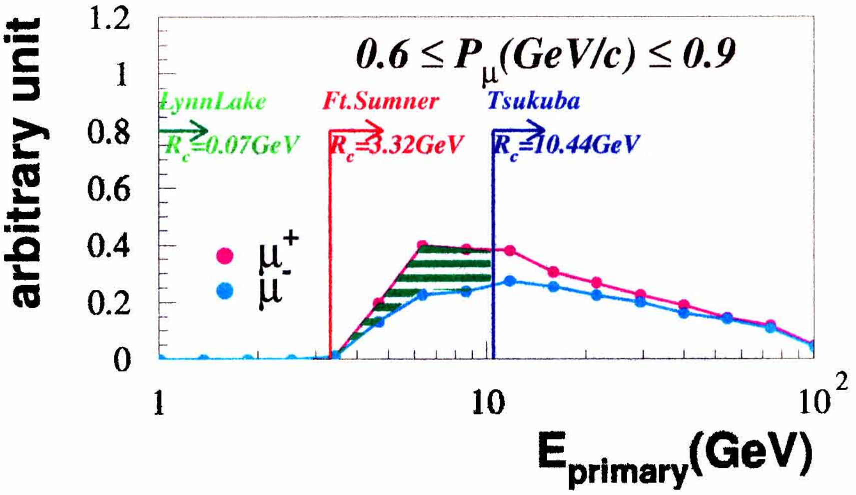

Figure 6.19: $\mu^{\pm}$ contributed from primary cosmic rays in a muon momentum range 0.6 - 0.9 GeV/c.

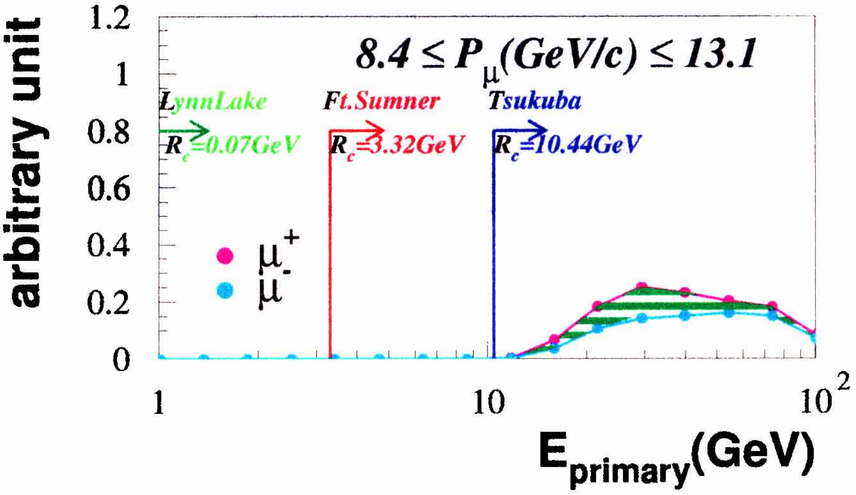

Figure 6.20: $\mu^{\pm}$ contributed from primary cosmic rays in a muon momentum range 8.4 - 13.1 GeV/c.

Chapter 7

Conclusion

We observed the atmospheric muons on the ground at Ft. Sumner, NewMexico, on 4th September in 2001, at an altitude of 1270 m above sea level with a cut-off rigidity of 4.2 GV (BESS-2001). The experiment of BESS-2001 at Ft. Sumner to collect the fundamental data was successful. We obtained the fluxes of positive and negative muons measured by the BESS detector for four hours in the momentum range of 0.5 - 20 GeV/c. The absolute fluxes of atmospheric muons were determined within an estimated total error of 5 %. In order to estimate the geomagnetic latitude dependence, we compared with the previous BESS results observed at another two different geomagnetic locations. These locations are (i)LynnLake, Nothern Canada, at an altitude of 360 m above sea level with a cut-off of 0.4 GV from 1997 to 1999 (BESS-1997/98/99), and (ii)Tsukuba, Japan, at an altitude of 30 m above sea level with a cut-off of 11.4 GV in 1995 (BESS-1995). The geomagnetic latitude dependence was determined quantitatively and qualitatively on the positive to negative charge ratios at these three different geomagnetic locations.

In order to estimate geomagnetic latitude effect, The muon fluxes of BESS-2001 (Ft. Sumner), BESS-1997/98/99 (LynnLake), and BESS-1995 (Tsukuba) are compared with each other. Those experiments where performed at different altitude and on different periods of observations. In order to extract the effect of geomagnetic latitude, the different altitudes and periods of observation have to be corrected to the same condition.

At first, we corrected for the altitude. Using the fluxes of BESS-1995 (Tsukuba) and BESS-1999 (Mt. Norikura) with almost same cut-off rigidity each other, the manner of altitude correction is provided by the processes of decay, ionization loss, and production of muons. The muon production between Mt. Norikura altitude and Tsukuba altitude is negligible. Thus, in order to correct for observing altitude, the processes of decay and ionization loss of muons are considered. The estimated fluxes at Tsukuba altitude from BESS-2001 (Ft. Sumner) and BESS-1997/98/99 (LynnLake) was corrected for altitude with same manner.

Second, The muon fluxes of BESS-2001 (Ft. Sumner), BESS-1997/98/99 (LynnLake), and BESS-1995 (Tsukuba) were observed on different periods with each other. The different of measurement periods gives the effect of solar modulation. In order to estimate the solar activity dependence, the muon fluxes of BESS-2001 and CAPRICE97 were compared with each other. Both experiments were performed at Ft. Sumner on the ground, on different periods. The difference of muon spectra of BESS-2001 (Ft. Sumner) and CAPRICE97 (Ft. Sumner) was ~ 15 % at 1 GeV/c. Taking μ^+/μ^- charge ratio, however, the difference of charge ratios of both observations was ~ 3 %. Taking charge ratio, it is effective to reduce the solar modulation effect.

In order to discuss the geomagnetic latitude effect, the charge ratios of BESS-2001 (Ft. Sumner), BESS-1997/98/99 (LynnLake), and BESS-1995 (Tsukuba) were compared with each other. The charge ratio of BESS-2001 (Ft. Sumner) after altitude correction was close to that of BESS-1997/98/99 (LynnLake) around 1 GeV/c. There is difference in geomagnetic cut-off rigidities of Ft. Sumner and LynnLake, however, because geomagnetic latitude effect is not effective for primary cosmic-ray from Monte Carlo simulation. The difference of geomagnetic latitude appears around 1 GeV/c between the charge ratio of BESS-2001 (Ft. Sumner) or BESS-1997/98/99 (LynnLake) and that of BESS-1995 (Tsukuba). Since the low momentum muons must be generated by primary cosmic-ray above 10 GeV at Tsukuba and by low energy primary cosmic rays at LynnLake and Ft. Sumner, the large number of positive and negative muons are generated by the multiplicity of pion production from the higher energy primary cosmic-ray at Tsukuba and the small number of positive and negative muons are generated at LynnLake and Ft. Sumner. The charge ratios at Ft. Sumner, LynnLake and Tsukuba were agreement with each other around 10 GeV/c. Because geomagnetic latitude effect is not effective for primary cosmic-ray at Ft. Sumner, LynnLake and Tsukuba from Monte Carlo simulation. We were able to explain qualitatively these difference by Monte Carlo simulation.

Appendix A

Survival Probability of Atmospheric Muons

Atmospheric muons produced at high altitude decay and lose energy as these run through the air. Probability that atmospheric muons survive until a level is called "survival probability". In this Appendix A, at first, survival probability for atmospheric muons without energy loss is described, second, survival probability with energy loss is represented.

A.1 Survival probability without energy loss

Parameters are defined as follows;

βc : velocity

$\gamma = 1/\sqrt{1-\beta^2}$: Lorentz factor

$\gamma\tau$: life time

E : total energy

m : mass

$\rho[g/cm^3]$: atmospheric density

b : decay constant

x : atmospheric depth

Calculations of decay probability.
Decay probability per unit time.

$$\frac{1}{\gamma\tau}$$

Decay probabilty per unit length.

$$\frac{1}{c\beta\gamma\tau} = \frac{m}{p\tau}$$

$$(p = \beta\gamma mc)$$

Decay probability per unit amount of substance.

$$\frac{m}{\rho p\tau} \tag{A.1}$$

Assuming constant for temperature of atmosphere, atmospheric density become constant. A constant scale height under constant for atmospheric density is;

$$h = \frac{x}{\rho} \tag{A.2}$$

$$[cm] = \frac{[g/cm^2]}{[g/cm^3]}$$

Eq (A.1) is substituted for Eq (A.2), decay probability per unit amount of substance is represented as follows;

$$\begin{aligned}\frac{m}{\rho p\tau} &= \frac{m}{\frac{x}{h}p\tau}\\ &= \frac{mh}{xp\tau}\\ &= \frac{b}{xp}\end{aligned} \tag{A.3}$$

$$(b = \frac{mh}{\tau})$$

b is constant, defined as decay constant.

It is assumed that Decay constant b and momentum p are constant and independent of atmospheric depth x. Then survival probability $\omega(x)$ is;

$$
\begin{aligned}
\frac{d\omega(x)}{dx} &= -\frac{b}{px}\omega \\
\frac{d\omega(x)}{\omega} &= -\frac{b}{px}dx \\
\int_{x_1}^{x_2} \frac{d\omega(x)}{\omega} &= \int_{x_1}^{x_2} \left(-\frac{b}{px}\right) dx \\
\ln\omega &= -\frac{b}{p}\left(\ln x_2 - \ln x_1\right) \\
&= \ln\left(\frac{x_2}{x_1}\right)^{-\frac{b}{p}} \\
\omega &= \left(\frac{x_2}{x_1}\right)^{-\frac{b}{p}}
\end{aligned}
\tag{A.4}
$$

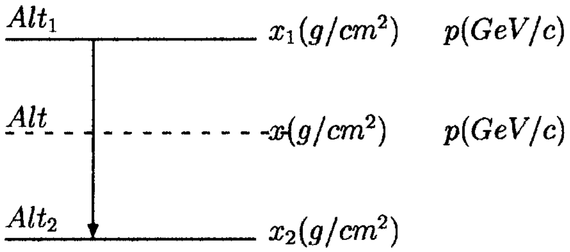

Figure A.1: Survival probability of muons at atmospheric depth x_2 from x_1.

A.2 Survival probability with energy loss

A.2.1 In case that muons run on the ground from the high altitude (atmospheric depth $x_1 \to x_2$)

Parameters are defined as follows;

$x_1[g/cm^2]$: atmospheric depth at Alt_1

$x_2[(g/cm^2]$: atmospheric depth at Alt_2 ($Alt_1 > Alt_2$, $x_1 < x_2$)

$x[g/cm^2]$: atmospheric depth at Alt ($Alt_1 > Alt > Alt_2$, $x_1 < x < x_2$)

$p(x_1)[GeV/c]$: momentum at x_1

$p(x)[GeV/c]$: momentum at x

$a\left[\frac{GeV/c}{g/cm^2}\right]$: energy loss rate per a unit of amount of substance

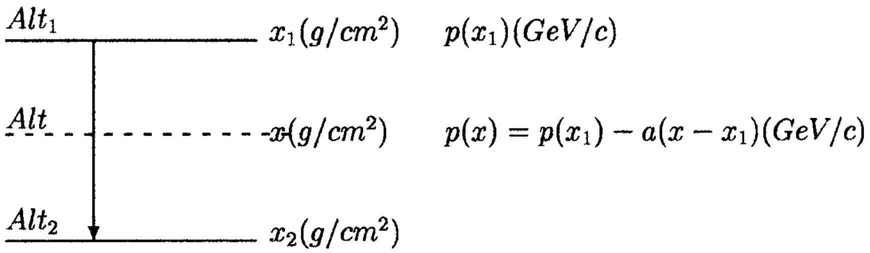

Figure A.2: Survival probability of muons at atmospheric depth x_2 from x_1

The probability that the particle generated in the atmospheric depth x_1 will survive to atmospheric depth x_2 will be calculated. Survival probability of muons is represented as follow equation;

$$\omega(x_1, x_2, p(x_1)) = \exp\left(-\int_{x_1}^{x_2} \frac{b(x)}{xp(x)}dx\right) \tag{A.5}$$

where, b(x)=const.

Momentum $p(x)$ is described as a muon momentum between at atmospheric depth x_1 and x_2. Momentum $p(x)$ using atmospheric depth x_1 is

$$p(x) = p(x_1) - a(x - x_1) \tag{A.6}$$

where, a means energy loss rate per a unit of amount of substance($a \sim 2[\frac{MeV/c}{g/cm^2}]$).

Eq. (A.6) is substituted for $p(x)$ of Eq. (A.5).

$$\omega = \exp\left(-\int_{x_1}^{x_2} \frac{b}{x\left(p(x_1) - a(x - x_1)\right)}dx\right) \tag{A.7}$$

$$
\begin{aligned}
\omega &= \exp\left(- \int_{x_1}^{x_2} \frac{b}{p(x_1) + a x_1} \left(\frac{1}{x} + \frac{a}{p(x_1 - a(x - x_1)} \right) dx \right) \\
&= \exp\left(- \frac{b}{p(x_1) + a x_1} \int_{x_1}^{x_2} \left(\frac{1}{x} + \frac{a}{p(x_1 - a(x - x_1)} \right) dx \right) \\
&= \exp\left(- \frac{b}{p(x_1) + a x_1} \left[\ln x + \ln \left(\frac{-1}{p(x_1) - a(x - x_1)} \right) \right]_{x_1}^{x_2} \right) \\
&= \left(\frac{x_2}{x_1} \frac{p(x_1)}{p(x_1) - a(x_2 - x_1)} \right)^{-\frac{b}{p(x_1) + a x_1}}
\end{aligned}
\tag{A.8}
$$

A.2.2 In case that muons are traced from ground to high altitude (atmospheric depth $x_2 \to x_1$)

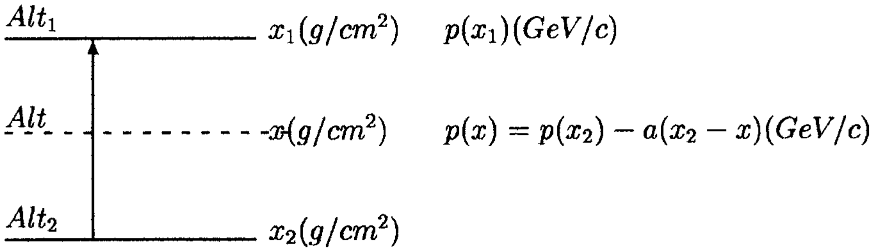

Figure A.3: Survival probability traced from atmospheric depth x_2 to x_1

Momentum $p(x)$ at atmospheric depth x using momentum $p(x_2)$ at atmospheric depth x_2 is

$$
p(x) = p(x_2) + a(x_2 - x) \tag{A.9}
$$

Probability that survived atmospheric muons at atmospheric depth x_2 are traced to x_1 will be calculated. Momentum $p(x_1)$ in terms of survival probability(Eq. (A.8)) is replaced in $p(x_2)$.

$$
\begin{aligned}
p(x) &= p(x_2) + a(x_2 - x) \\
&= p(x_1) - a(x - x_1)
\end{aligned}
$$

Thus,

$$p(x_1) = p(x_2) + a(x_2 - x_1) \tag{A.10}$$

Eq. (A.10) is substituted for Eq. (A.8).

$$\begin{aligned}
\omega &= \left(\frac{x_2}{x_1}\frac{p(x_2)}{p(x_2)+a(x_2-x_1)-a(x_2-x_1)}\right)^{-\frac{b}{p(x_2)+a(x_2-x_1)+ax_1}} \\
&= \left(\frac{x_2}{x_1}\frac{p(x_2)+a(x_2-x_1)}{p(x_2)}\right)^{-\frac{b}{p(x_2)+ax_2}} \\
&= \left(\frac{x_1}{x_2}\frac{p(x_2)}{p(x_2)+a(x_2-x_1)}\right)^{\frac{b}{p(x_2)+ax_2}}
\end{aligned} \tag{A.11}$$

In the same way as section A.2.1, substituting Eq. (A.9) for Eq. (A.5), same result as Eq. (A.11) is obtained.

Acknowledgments

I wish to express my special thanks to Professor M. Nozaki, who had led the BESS experiment and greatly motivated me to the research reported in this thesis. I wish to express my sincere thanks to Professor A. Yamamoto who have led the BESS experiment, for their guidance throughout my research reported in this thesis. I greatly appreciate helpful suggestions from Professor J. Nishimura and Dr. T. Sanuki, and discussions with Dr M. Honda about the theoretical calculations. I also wish to gratefully appreciate Professor T. Yoshida and Dr. T. Sanuki who have lead the campaign to a success. The calibration and analysis were done owing a lot to Dr. T. Sanuki, Dr. K. Abe, Dr. Y. Shikaze, Dr. M. Motoki, and Dr. H. Matsumoto. I would like to acknowledge them for their suggestions and helpful discussions and assistance at the various stages of the analysis. I would like to thank Professor N. Yajima, Professor T. Yamagami, and all the other BESS-Japan colleagues for their effort to make the experiment successful.

I would deeply appreciate Dr. J. Ormes, Dr. R. Streitmatter, Dr. J. Mitchell, Dr. A. Moiseev, and Dr. E. S. Seo, those who are the US collaborators of the experiment. Furthermore, I am grateful to Dr. V. Jones and all other people at NASA who supported BESS and to the balloon campaign team from the National Scientific Balloon Facility for their professional and skillful work in carrying out the BESS flights.

I greatly acknowledge Professor O. Matsuo, Director General of ISAS, Professor H. Sugawara, Director General of KEK, and Professor S. Iwata of KEK for their support and encouragement. Sincere thanks go to International Center for Elementary Particle Physics (ICEPP) of the University of Tokyo for kindly allowing me to use their computing facilities. The data of the CLIMAX neutron monitor were provided by Space Physics Data System of University of Chicago, supported by National Science Foundation Grant ATM-9420790.

The BESS experiment has been supported by Grant-in-Aid for Scientific Research on Priority Areas (12047227 and 12047206) from the Ministry of Education, Culture, Sports Science and Technology (MEXT).

I would appreciate T. Sugimoto, A. Itasaki, K. Takeuchi and Y.Takasugi who wake me up every morning.

References

[1] M.Motoki, *et al.*, Astropart. Phys. 19, 113-126 (2003)

[2] T.Sanuki, *et al.*, Phys. Lett. B, 541, 234-242 (2002)

[3] J.Kremer, *et al.*, Phys. Rev. Lett. 83, 4241-4244 (1999)

[4] B.Rossi, Rev. Mod. Phys. 20, 537-561 (1948)

[5] A. Yamamoto *et al.*, Adv. Space Res. **14(2)**, 75 (1994).

[6] Y. Ajima *et al.*, Nucl. Instrum. Methods A **443**, 71 (2000).

[7] Y. Asaoka *et al.*, Nucl. Instrum. Methods A **416**, 236 (1998).

[8] Y. Shikaze *et al.*, Nucl. Instrum. Methods A **455**, 596 (2000).

[9] S.Orito, Proc. of the ASTROMAG Workshop, KEK Report 87-19, 111(1987)

[10] A. Buffington *et al.*, The Astrophys. J. **199** (1975) 669.

[11] R.L. Golden *et al.*, Nucl. Instr. Method, **148** (1978) 179.

[12] M.H. Salamon *et al.*, The Astrophys. J. **349** (1990) 78.

[13] R.L. Golden *et al.*, Nucl. Instr. Method, **A306** (1991) 366.

[14] S.W. Barwick *et al.*, Nucl. Instr. Method, **A400** (1997) 34.

[15] A. Yamamoto *et al.*, IEEE Trans. Mag. **24** (1988) 1421.

[16] Y. Makida *et al.*, Adv. Cryog. Eng., **37** (1992) 401.

[17] Y. Makida *et al.*, IEEE Trans. Applied Superconductivity **5** (1995) 658.

[18] A. Yamamoto *et al.*, Adv. Space Res., **14** (1994) (2)75.

[19] R.J. Yarema, FERMILAB-TM-1284 (1984).

[20] R. Suda *et al.*, Nucl. Instr. and Meth. A406 (1998) 213.

[21] R. Enomoto *et al.*, Nucl. Instr. and Meth.

[22] T. Massam, GUIDE7: a general program for evaluating the properties of scintillation and Čerenkov counter optical systems, CERN 76-21 (1976).

[23] INMOS, Transputer Reference Manual, Prentice Hall (1998).

[24] G. Jones and M. Goldsmith, Programming in Occam2, Prentice Hall (1998).

[25] M. Imori *et al.*, IEEE Trans. Nucl. Sci. **39** (1992) 987.

[26] H. Matsumoto *et al.*, IEEE Trans. Nucl. Sci., **43** (1996) 2195.

[27] K. Anraku, S. Inaba and M. Imori, IEEE Trans. Nucl. Sci. **40** (1993) 717.

[28] W.B. Atwood, Time of flight measurements, SLAC-PUB-2620, October 1980.

[29] T. Tanimori *et al.*, Nucl. Instr. and Meth. 216 (1983) 57.

[30] E. Chen et al., hep-ex/9606007.

[31] T. Saeki *et al.*, Nucl. Instr. Method, **A355** (1995) 506.

[32] V. Karimaki, Comput. Phys. Commun., **69** (1992) 133.

[33] LonWorks Technology Device Data, Rev. 5, Motorola Inc. USA.

[34] EIA Standard, EIA-709.1 "Control Network Protocol Specification" (1998).

[35] PhotoMOS Relay Specification, Matsushita Electric Works, Ltd., Japan.

[36] INMOS, Transputer Reference Manual, Prentice Hall (1998).

[37] G. Jones and M. Goldsmith, Programming in Occam2, Prentice Hall (1998).

[38] Rika nenpyo (Chronological Scientific Tables), ed. National Astronomical Observatory, Maruzen Co., Ltd.

[39] General Libraries, The University of Texas at Austin
(http://www.lib.utexas.edu/maps/index.html)

[40] R. Brun, *et al.*, GEANT3.21, CERN Program Library Long Write up W5013.

[41] J.D. Sullivan, Nucl. Instrum. Methods 95, 5 (1971)

[42] R.L. Golden, *et al.*, J. Geo. Res., 100, 515-522 (1995)

[43] Y. Hayakawa, Cosmic Ray, Iwanami-kouza, Gendai-butsurigaku III.C.

[44] Aerological Observatory (http://www.kousou-jma.go.jp/index.html)

[45] M.Ogura, Ippankishougaku, Tokyodaigaku-shuppankai

[46] Physical Review D, Particles and Fields, 010001-196

[47] GEANT, Detector Description and Simulation Tool, 290-295

[48] http://nssdc.gsfc.nasa.gov/space/model/models/msis.html

[49] A.E.Hedin, et al., J.Geophys. Res. 88, 10170 (1983)

[50] A.E.Hedin, et al., J.Geophys. Res. 92, 4649 (1987)

[51] A.E.Hedin, et al., J.Geophys. Res. 96, 1159 (1991)

[52] T.Snuki *et al.*, Physics Letters B, 577 (2003) 10-17

[53] Kocharian, N.M., M.T.Aivazian, Z.A.Kirakosian, and A.S.Aleksanian, J. Exp. Theoret. Phys., USSR, 30, p.243 (1956)

[54] Kocharian, N.M., M.T.Aivazian, Z.A.Kirakosian, and A.S.Aleksanian, Sov. Phys. JETP, 3, p.350 (1956)

[55] Kocharian, N.M., G.S.Saakian, and Z.A.Kirakosian, J. Exp. Theoret. Phys., USSR, 35, p.1335 (1958)

[56] Kocharian, N.M., G.S.Saakian, and Z.A.Kirakosian, Sov. Phys. JETP, 35, p.933 (1959)

[57] Manfredotti, C., C.Ongaro, A.Zanini, M.Cavaioli, and L.Tommasino, in SPIE Proceedings Series, ed. George Vourvopoulos, Vol.2867, p.619 (1997)

[58] Peter K.F. Grieder, Cosmic Rays at Earth, Researcher's Reference Manual and Data Book, p.38

[59] T.K.Gaisser and M.Honda, Annu. Rev. Nucl. Part. Sci.,52:153-99 (2002)

[60] Y.Shikaze, Ph.D. thesis, University of Tokyo, (2001)

[61] M.Honda, Private communication and M.Honda et al. (2003)

[62] K.Abe, et al., Phys. Lett. B 564, 8-20 (2003)

[63] Space Physics Data System, University of New Hampshire Neutron Monitor Datasets (http://ulysses.sr.unh.edu/NeutronMonitor/neutron_mon.html)

[64] R.Brun, et al., GEANT3.21, CERN Program Library Long Write up W5013.

[65] H.C.Feselfedt, et al., PITHA 85/02 Aachen, 1985.

[66] A.Fassó, et al., Proc. IV int. Conf. on Calorimetry in High Energy Physics. (La Biodola(Italy))21-26 September 1993, Ed.A.Menzione and A.Scribano, World Scientific, 282(1981)

[67] M.Honda, et al., Physical Review D 52, 4985 (1995)

[68] A.G.W.Cameron, et al., Space Sci. Rev. 15, 121 (1973)

[69] M.M.Shapiro and R.Silberberg, et al., Phil. Trans. Roy. Soc. 277, 317 (1975)